

Markus Rein

Order Reduction for Nonlinear Dynamic Models of District Heating Networks



$$\partial_t e_\alpha(t, x) = -v_\alpha(t) \partial_x e_\alpha(t, x)$$

$$e_k(t) = \frac{\sum_{a \in \mathcal{I}_k} q_a(t) e_a(t, L_a)}{\sum_{a \in \mathcal{O}_k} q_a(t)}$$

$$Kq = 0$$

$$G_a = q_a(e_{a:k} - e_{a:m})$$

$$\frac{1}{\rho_\alpha} \partial_x p_\alpha = -\dot{v}_\alpha - \frac{\lambda(v_\alpha, e_\alpha)}{2d_\alpha} v_\alpha |v_\alpha| - g \partial_x z_\alpha$$

$$p_k(t) = p_a(0, t)$$

$$p_m(t) = p_a(L_a, t)$$

Fraunhofer-Institut für
Techno- und Wirtschaftsmathematik ITWM

Order Reduction for Nonlinear Dynamic Models of District Heating Networks

Markus Rein

FRAUNHOFER VERLAG

Kontakt:

Fraunhofer-Institut für Techno- und Wirtschaftsmathematik ITWM
Fraunhofer-Platz 1
67663 Kaiserslautern
Telefon +49 631/31600-0
Fax +49 631/31600-1099
E-Mail info@itwm.fraunhofer.de
URL www.itwm.fraunhofer.de

Bibliografische Information der Deutschen Nationalbibliothek

Die Deutsche Nationalbibliothek verzeichnet diese Publikation in der Deutschen Nationalbibliografie; detaillierte bibliografische Daten sind im Internet über <http://dnb.d-nb.de> abrufbar.
ISBN (Print): 978-3-8396-1581-2

D 386

Zugl.: Kaiserslautern, TU, Diss., 2019

Titelbild: © Markus Rein

Druck: Mediendienstleistungen des
Fraunhofer-Informationszentrum Raum und Bau IRB, Stuttgart

Für den Druck des Buches wurde chlor- und säurefreies Papier verwendet.

© by **FRAUNHOFER VERLAG**, 2020

Fraunhofer-Informationszentrum Raum und Bau IRB
Postfach 80 04 69, 70504 Stuttgart
Nobelstraße 12, 70569 Stuttgart
Telefon 07 11 9 70-25 00
Telefax 07 11 9 70-25 08
E-Mail verlag@fraunhofer.de
URL <http://verlag.fraunhofer.de>

Alle Rechte vorbehalten

Dieses Werk ist einschließlich aller seiner Teile urheberrechtlich geschützt. Jede Verwertung, die über die engen Grenzen des Urheberrechtsgesetzes hinausgeht, ist ohne schriftliche Zustimmung des Verlages unzulässig und strafbar. Dies gilt insbesondere für Vervielfältigungen, Übersetzungen, Mikroverfilmungen sowie die Speicherung in elektronischen Systemen.

Die Wiedergabe von Warenbezeichnungen und Handelsnamen in diesem Buch berechtigt nicht zu der Annahme, dass solche Bezeichnungen im Sinne der Warenzeichen- und Markenschutz-Gesetzgebung als frei zu betrachten wären und deshalb von jedermann benutzt werden dürften. Soweit in diesem Werk direkt oder indirekt auf Gesetze, Vorschriften oder Richtlinien (z.B. DIN, VDI) Bezug genommen oder aus ihnen zitiert worden ist, kann der Verlag keine Gewähr für Richtigkeit, Vollständigkeit oder Aktualität übernehmen.

Order reduction for nonlinear dynamic models of district heating networks

Markus Rein

Vom Fachbereich Mathematik
der Technischen Universität Kaiserslautern
zur Verleihung des akademischen Grades
Doktor der Naturwissenschaften
(**Doctor rerum naturalium, Dr. rer. nat.**)
genehmigte Dissertation

1. Gutachter: Prof. Dr. Axel Klar, Technische Universität Kaiserslautern
2. Gutachter: Prof. Dr. Nicole Marheineke, Universität Trier

Datum der Disputation: 11.12.2019

D 386

Acknowledgments

During this thesis, I strongly benefited from the support of numerous people making this work possible.

First of all, I would like to thank my academic supervisors Axel Klar and Tobias Damm for being open towards the research project. Their comments and suggestions improved the thesis in many respects. Further thanks go to Raul Borsche, Stephan Trenn, René Pinnau, and Nicole Marheineke for their valuable advice and remarks.

I would like to thank Jan Mohring for the time and power he invested as my supervisor at ITWM. At any phase of the thesis I could rely on his interest and valuable suggestions. I extend my thanks to Jarosław Wlazło, Norbert Siedow, Dominik Linn and Matthias Eimer from the EMO group within the department of transport processes. I always enjoyed our discussions and the pleasant working atmosphere. Furthermore, I would like to thank Martin Heidenbluth and the Technische Werke Ludwigshafen AG, as well as the GEF Ingenieur AG for sharing their practical expertise.

Many thanks go to the TV Mensa group for all the delightful moments before, during and after lunch time. I highly enjoyed our trips to Munich, Budapest and Vienna.

I want to express my special thanks to my family for always believing in me. Your support has been a constant source of motivation. Finally, I thank my girlfriend Tanja for her continuous trust and love. You guided me through the ups and downs of this thesis, as well as my entire academic path ever since A-levels. I am glad to know you at my side.

Grünstadt, October 2019
Markus Rein

Declaration

I hereby declare that I have developed and written the thesis entitled “Order reduction for nonlinear dynamic models of district heating networks” entirely by myself and have not used sources or means without declaration in the text. Any thoughts or quotations which were inferred from these sources are clearly marked as such. This thesis is submitted to the Department of Mathematics at the University of Kaiserslautern. It has not been submitted in the same or in a substantially similar version, not even partially, to any other authority to achieve an academic grading. A list of publications resulting from this thesis is provided in the chapter publications.

Grünstadt, October 2019
Markus Rein

Publications

In the course of the research leading to this thesis, the following conference proceedings and journal publications were written. All of the listed works are within or have passed a peer-review process. Parts of the listed publications are contained in this thesis.

- M. Rein, J. Mohring, T. Damm, A. Klar, Parametric model order reduction for district heating networks, *Proc. Appl. Math. Mech* **18**, e201800192 (2018) (published)
- M. Rein, J. Mohring, T. Damm, A. Klar, Stability preserving model order reduction for district heating networks, *Progress in Industrial Mathematics at ECMI 2018* (2018) (accepted)
- M. Rein, J. Mohring, T. Damm, A. Klar, Reduction of a district heating model using network decomposition, *Proc. Appl. Math. Mech* **19** (2019) (accepted)
- S. Hauschild, N. Marheinke, V. Mehrmann, J. Mohring, A. Badlyan, M. Rein, M. Schmidt, Port-Hamiltonian modeling of district heating networks, arXiv:1908.11226 (2019) (submitted to *Progress in Differential-Algebraic Equations II*)
- M. Rein, J. Mohring, T. Damm, A. Klar, Model order reduction of hyperbolic systems at the example of district heating networks, arXiv:1903.03342 (2019) (submitted to the *Journal of The Franklin Institute*)
- M. Rein, J. Mohring, T. Damm, A. Klar, Optimal control of district heating networks using a reduced order model, arXiv:1907.05255 (2019) (submitted to *Optimal Control Application & Methods*)

Abstract

English version

District heating networks are expected to play a major role towards a carbon neutral supply with energy by their flexibility to operate different sustainable energy sources. Using a network of pipelines, heated water is transported from a centralized power plant to buildings for heating purposes. An efficient operation of these networks requires an optimal control of the supplied energy input while considering technical constraints and power demands. The mathematical task is challenging due to the complex dynamics on large scale district heating networks. When included in an online-planning, algorithms deriving an optimal control strategy face runtime restrictions, explaining the need for an efficient computation of the transport dynamics. To this end, this thesis focuses on surrogate models for a numerically efficient simulation of district heating networks. Their dynamics are advection dominated, leading to a system of quasi-linear hyperbolic partial differential equations equipped with algebraic coupling conditions introduced by the network structure. Using an appropriate spatial discretization, a control system is derived allowing to preserve essential properties such as Lyapunov stability to the reduced order model. By splitting the problem into a differential part describing the transport of thermal energy and an algebraic part defining the flow field, tools from parametric model order reduction can be applied. An algorithm is suggested which produces a global Galerkin projection based on a moment-matching of local transfer functions in the frequency domain. It is applicable for various input scenarios of a given network topology. The benefits of the resulting surrogate model are demonstrated at different, existing large scale networks. In addition, the performance of the suggested model is studied in the numerical computation of an optimal control of the feed-in power employing a discretize-first strategy.

Deutsche Version

Fernwärmenetze zeichnen sich durch ihre Flexibilität aus, durch verschiedene nachhaltige Energiequellen gespeist werden zu können, und spielen somit eine zentrale Rolle für eine klimaneutrale Energieversorgung. Über ein Rohrleitungsnetz wird erhitztes Wasser aus einem Kraftwerk zu Heizzwecken zu Gebäuden transportiert. Ein effizienter Betrieb dieser Netze erfordert eine optimale Steuerung der eingespeisten Energie unter Berücksichtigung technischer Randbedingungen und des Leistungsbedarfs. Das entsprechende mathematische Problem ist aufgrund der komplexen Topologie großer Fernwärmenetze herausfordernd. Durch Zeitrestriktionen in einer Echtzeit-Planung müssen Simulationsmodelle der Transportdynamik hinreichend effizient sein. Zu diesem Zweck konzentriert sich diese Arbeit auf die Erzeugung von Ersatzmodellen für eine numerisch effiziente Simulation von Fernwärmenetzen. Ihre Dynamik ist durch Advektion dominiert, was zu einem System quasilinearer hyperbolischer partieller Differenzialgleichungen führt. Erhaltungsgleichungen an den Netzwerkknoten erzeugen zusätzliche algebraische Kopplungsbedingungen. Mit einer geeigneten räumlichen Diskretisierung wird eine Systemformulierung erzeugt, mit der wesentliche Eigenschaften wie Lyapunov Stabilität in das Ersatzmodell übertragen werden. Durch Aufteilung des Modells in einen differentiellen Teil, der den Transport von Wärmeenergie beschreibt, und einen algebraischen Teil, der das Strömungsfeld definiert, resultiert ein linear zeitvariendes Transportproblem. Zur Erzeugung des Ersatzmodells werden Konzepte der parametrischen Modellordnung angewendet. Der in der Arbeit erarbeitete Algorithmus generiert eine globale Galerkin-Projektion, die auf einer Momentenanpassung von lokalen Übertragungsfunktionen im Frequenzbereich basiert. Das vorgeschlagene Ersatzmodell weist eine stark reduzierte Zustandsraumdimension auf und ist für verschiedene Einspeiseszenarien anwendbar. Die Vorteile des Modells werden in verschiedenen numerischen Analysen für Topologien existierender Netzwerke demonstriert. Diese beinhalten neben der Abbildung der Transportdynamik auch die Berechnung einer optimalen Steuerung der Einspeiseleistung.

Contents

Publications	v
Abstract	vii
1 Introduction	1
2 PDE modeling of heating networks	7
2.1 Model components	7
2.1.1 Incompressible flow in a pipeline	7
2.1.2 Material laws and state equations	9
2.1.3 Coupling conditions on the network	11
2.1.4 Network boundary conditions: source and consumers	13
2.2 Elimination of algebraic equations	15
2.3 Hydrodynamic equations	17
2.4 Basic PDE model	21
3 DAE model	23
3.1 Spatial discretization of advection dominated transport	23
3.1.1 Finite difference methods	25
3.1.2 Finite volume methods	26
3.1.3 Discontinuous Galerkin methods	27
3.1.4 Upwind scheme on heating networks	28
3.1.5 Basic DAE model resulting from upwind discretization	30
3.2 Formulation of a control system	31
3.2.1 Linear time varying system	31
3.3 Affine decomposition of system and input operator	33
3.4 Existence and uniqueness of solutions	39
3.5 Differentiation index of the DAE	43
3.6 Stability	45
3.6.1 Lyapunov stability	45
3.6.2 Comparison of volume- and mass conservation	49
3.6.3 Asymptotic stability	51
3.7 Controllability and observability	55
3.8 Port-Hamiltonian systems	58
3.8.1 Nonlinear port-Hamiltonian systems	58
3.8.2 Semi-discrete port-Hamiltonian description for heating networks	59
3.9 Conclusions	62

4	Model order reduction for district heating networks	63
4.1	Reduction by projection	64
4.2	Reduction of linear time varying systems	66
4.2.1	Proper orthogonal decomposition	67
4.2.2	Model reduction by interpolation	68
4.2.3	Parametric model order reduction	70
4.3	Transfer function on a single pipeline	70
4.4	Further reduction approaches	73
4.5	Generation of suitable Galerkin projections	75
4.6	Conclusions	80
5	Numerical analysis of the reduced order model	83
5.1	Model assumptions	84
5.2	Simulation setup	85
5.3	Domain decomposition of heating networks	87
5.3.1	Decomposition into main- and subnetworks	88
5.3.2	Preservation of Lyapunov stability	89
5.3.3	Decomposition strategy and numerical validation	90
5.4	Numerical analysis of the reduced order model	92
5.4.1	Test case street network	93
5.4.2	Test case district network	96
5.4.3	Reduction of subnetworks including changes of flow direction . .	98
5.5	Conclusions	100
6	Optimal control of heating networks using reduced order models	103
6.1	Optimization objectives of heating networks	103
6.2	Model assumptions	106
6.3	Control problem	107
6.4	Determination of an optimal control	111
6.5	Numerical validation	113
6.5.1	Time integration of the DAE	113
6.5.2	Definition of test scenarios	114
6.5.3	Numerical controls obtained by full and reduced order model . .	115
6.5.4	Components of the speed-up of the reduced order model	121
6.6	Conclusions	123
7	Conclusions and outlook	125
	Bibliography	136
	Curriculum vitae	137
	Lebenslauf	138

Chapter 1

Introduction

A central challenge of today's world is the efficient supply and use of energy. With the increasing share of renewable energies, sources of energy and its transportation to consumers became more volatile and diverse. This development involves significant challenges in planning the use of energy transportation networks such as electrical grids, gas, water, and heating networks. The available energy has to be used as efficient as possible while meeting technical operation conditions as well as consumer demands. The mathematical task is highly complex and involves modeling of the components, simulation of the transport dynamics and optimization of the control parameters at supplying units. When used in realtime planning, the corresponding optimization algorithm is restricted to a maximum runtime of typically 15 min. This stays in contrast to the complexity of real-world networks including 10^3 to 10^4 edges. To this end, this thesis focuses on the derivation of reduced order models allowing for a fast simulation of the energy transport in real-world district heating networks. The latter denote a network of thermally insulated pipelines transporting heat to residential and commercial buildings to cover heating demands [1]. District heating networks became more and more popular by their flexibility in utilizing different sources of energy such as geothermal power, solar power or heat stemming from waste incineration [2, 3, 1]. In addition, the large transport time from a centralized power plant to consumers induces storage effects in the network, allowing to efficiently distribute available heating power over time.

Structure of district heating networks

Fig. 1.1 sketches an exemplary heating network visualizing the basic components. A power plant injects heated water in the flow network where it is guided to buildings using pipelines. Inside the buildings, a heat exchanger is responsible for depositing the heating power required by the consumer. To this end, the heated fluid running in the primary grid network is cooled to a reference temperature, while the fluid inside a secondary network running within the building is heated. This indirect exchange of energy avoids material flow between heating networks and the buildings. By altering the volume flow passing the heat exchanger, each consumer can meet the desired heating power for a range of different water temperatures supplied by the power plant.

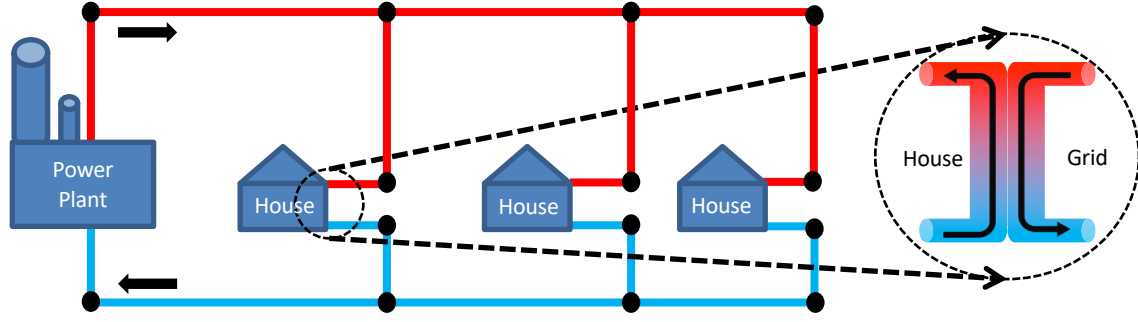


Figure 1.1: Visualization of an exemplary heating network with a flow part (red lines) and a return part (blue lines). The highlighted circle indicates a heat exchanger depositing heating power at building attached to the network.

This allows a flexibility in the fluid temperature injected at the power plant. After exiting the heat exchanger, the cooled fluid is transported back to the power plant within the return network and reheated again. It shall be noted that different forms of district heating networks exist. Within this thesis, a setup including a single power plant and thus a single injection point of thermal energy is studied. Furthermore, water is kept under sufficiently high pressure to ensure a liquid phase, which is the most common type of heating networks. By modeling indirect heat exchangers, flow and return network form a closed system for the water circulation. While fig. 1.1 is a simple example of district heating network, realistic networks include more complex features such as network cycles. These structures allow the fluid to take different paths to an identical consumer station, and possibly lead to a reversal of flux directions within certain pipelines, which is a key difficulty of heating networks Fig. 1.2 depicts a typical power plant setup also referred to as depot or source. A waste to heat incineration plant delivers an unregulated flow of enthalpy which can be used in different ways. First, the enthalpy level can be lowered using a valve. Second, it can be guided to a turbine, lowering the enthalpy while generating electricity. Third, heat can be stored in a heat storage to save it for later usages and finally it can be directly fed to the heating network. The demands of consumers attached to the district heating network have to be met at any time. A gas vessel located at the depot is able to compensate an insufficient supply of power by the waste to heat plant. A central aim of scheduling the depot lies in avoiding the use of the gas turbine since it involves high operation costs and fossil fuels.

Mathematical challenges and related works

The control and optimization of energy networks attains increasing attention not only in the academic sector. These include especially power grids [4, 5], water [6], gas [7, 8, 9, 10], and heating networks [11, 12, 13, 12, 14, 15]. Although exhibiting different physical dynamics, a large class of energy networks share a common description of

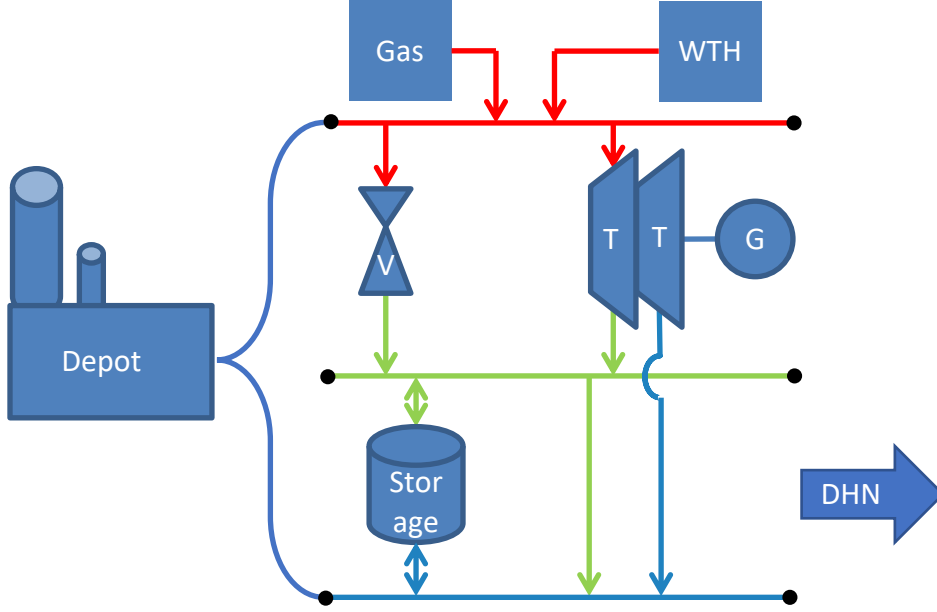


Figure 1.2: Sketch of an exemplary depot. A waste to heat (WTH) incineration plant supplies an energy flow which can be used in different ways. Using turbines(T), generators(G), a heating storage, and valves(V), energy can be converted to electricity, stored for later usages or injected to the heating network (DHN) at different enthalpy levels. A Gas vessel is able to support the WTH plant on demand.

hyperbolic partial differential equations. The latter describe the conservation of physical variables along an edge of the network subject to potential external sink or source terms. While for electric networks the conservative variables are the electrical current and voltage, water, gas and heating networks are determined by a fluid flow through pipelines. A model often applied for these networks are cross-sectional averaged, one dimensional Euler-like equations [16],

$$\partial_t(\rho) + \partial_x(v\rho) = 0, \quad (1.1a)$$

$$\partial_t(\rho v) + \partial_x(\rho v^2) = -\partial_x p - \rho k(v, e), \quad (1.1b)$$

$$\partial_t e + \partial_x(v e) = -p \partial_x v - c(e), \quad (1.1c)$$

Eq. (1.1) forms a set of quasi-linear hyperbolic equations in the state variables mass density ρ , momentum density ρv , and internal energy density e and describes the fluid transport at velocity v in a single pipeline within the network. The expressions k, c collect external interactions of the fluid with its environment including friction, gravity and thermal losses. A significant amount of research was conducted for water [6] and gas networks [17, 7, 8, 9, 6, 18], which are often modeled isothermal. For these networks the transport of energy density according to (1.1c) is not considered. In contrast, the transport of the internal energy density is the essential feature of heating networks. Since water in the liquid phase is modeled within this thesis, the incompressible limit of (1.1c) results, yielding an advection equation of the internal energy density. As a central difficulty of heating networks, the associated advection

velocity changes dynamically along time t due to the regulation of the volume flow by heat exchangers located at consumption points,

$$\partial_t e + v(t)\partial_x(e) = -c(e).$$

Additionally, the direction of the flow within distinct pipelines of a sufficiently complex network can change dynamically. These properties hinder the derivation of a reduced order model for district heating networks for the following reasons. First, advection dominated problems are known to exhibit a small singular value decay, resulting in computationally expensive, large reduced order models [19, 20, 21]. Second, the dynamic advection velocity introduces nonlinearities. Traditional model reduction techniques such as balanced truncation [22] can thus not directly be applied being designed for linear time invariant systems. Third, changes of flux direction adjust the path of the fluid from the power plant to a given consumption point qualitatively introducing a further nonlinearity in the dynamics. Another challenge in the simulation and reduction of heating networks as well as for other energy networks arises from their network structure. Pipelines entering and exiting network junctions introduce algebraic constraints to the dynamics on the pipelines such as the conservation of energy and mass [23, 24, 25]. When deriving reduced order models, special attention has to be paid to algebraic equations and the corresponding variables, since the reduction of algebraic equations can lead to numerical instabilities [26].

The contribution of this work is threefold and addresses the central difficulties of heating networks formulated above. First, by spatial discretization of the transport of energy density on each pipeline, a control system is derived, allowing to analyze the stability and other essential properties of the dynamical system. In contrast to prior works [27, 28, 13, 29, 11], the formulated model remains close to the underlying Euler-like equations (1.1). Second, a reduced order model is suggested based on moment matching of local linearizations, allowing to reduce the state space dimension of advection dominated transport on pipelines while preserving stability. Finally, the numerical efficiency of the suggested reduced order model is evaluated in simulating the dynamics of heating networks as well as in determining an optimal control.

Structure of the thesis

The thesis is structured as follows. Chapter 2 presents a model for the dynamics of district heating networks. It consists of a set of effectively one dimensional Euler-like partial differential equations (PDE) describing incompressible flow in pipelines equipped with algebraic coupling conditions resulting from a network description. In chapter 3, a finite volume discretization for the transport of thermal energy is discussed leading to a differential algebraic system of equations (DAE). The latter allows to deduce a control system describing the dynamics of heating networks. After discussing an affine decomposition of the corresponding system operators, a detailed stability analysis of the control system is presented. The control system is finally embedded into the concept of finite-dimensional port-Hamiltonian systems. Chapter 4 compares

different model reduction techniques and systematically derives an algorithm reducing the state space dimension of the thermal transport. The suggested algorithm addresses the advection dominated transport on a network and is based on moment matching of the transfer functions at local linearizations. The benefits of the suggested reduced order model towards an efficient simulation of heating networks are numerically analyzed in chapter 5. To further improve the projection based reduction, a decomposition strategy of heating network into smaller subnetworks is proposed and tested. Error and runtime of the reduced order model are compared to full order models and higher order hyperbolic schemes. The considered network topologies represent real-world networks supplied by the industrial partner Technische Werke Ludwigshafen AG (TWL). Chapter 6 investigates the reduced order model for applications in the determination of an optimal control. The precise control problem consists of minimizing absolute value and temporal variation of the input energy density while limiting the feed-in power as the central optimization constraint. Chapter 7 summarizes the achieved results and indicates further research directions.

Chapter 2

PDE modeling of heating networks

In this chapter a model describing the dynamics of district heating networks is developed, based on the Euler-like equations describing the fluid dynamics within a pipeline. In addition, models for consumers and the power plant are presented, defining the exchange of energy of the heating network with its environment. Thereafter, an analysis of the hydrodynamic equations is performed, forming the velocity at which thermal energy is transported through heating networks.

2.1 Model components

A model describing the transport of energy within district heating networks consists of three contributions. First an expression for the heat transport within a pipeline. Second the algebraic coupling conditions combining all pipelines attached to the same network node k . Third, boundary conditions defining the exchange of energy of the heating network with its environment given by the power plant and consumption points.

2.1.1 Incompressible flow in a pipeline

Subsequently the dynamics of water in a cylindrical pipeline with constant diameter d and length L shall be modeled, cf. fig. 2.1. The central variables describing the flow are the internal energy density (internal energy per unit volume) e , the mass density ρ and the fluid velocity v . Due to the cylindrical shape, radial symmetry is assumed, allowing to average all fluid quantities over the cross-section. The resulting one-dimensional quantities only change in direction of the cylinder axis $x \in (0, L)$ over time $t \in (t_0, t_{\text{end}}]$, with positive start- and ending times t_0, t_{end} . This allows to define $\rho, v, e : (0, L) \times (t_0, t_{\text{end}}] \mapsto \mathbb{R}$.

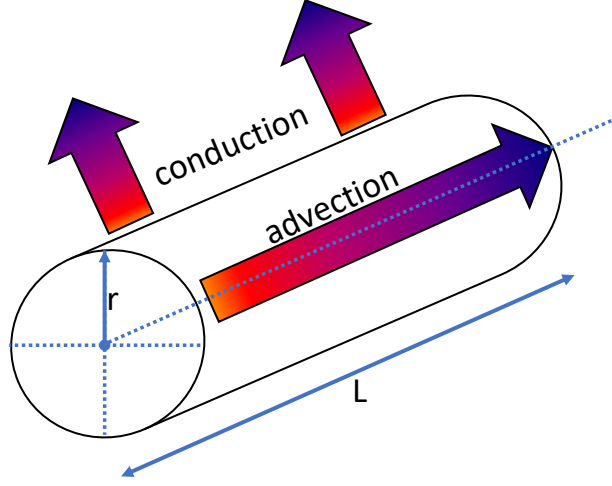


Figure 2.1: Illustration of a cylindrical pipeline with radius r and length L .

Compressible fluids

Within a pipeline, the effective one dimensional dynamics of a viscous, compressible fluid are described by the following three balance laws [16]

$$\partial_t \rho + \partial_x (v \rho) = 0 \quad (2.1a)$$

$$\partial_t (\rho v) + \partial_x (\rho v^2) = -\partial_x p - \rho k(v, e) \quad (2.1b)$$

$$\partial_t e + \partial_x (v e) = -p \partial_x v - c(e). \quad (2.1c)$$

Eq. (2.1a) denotes the conservation of mass, also known as the continuity equation. Similarly, (2.1b) corresponds to the balance of momentum density ρv with velocity v . It results from the three-dimensional Navier-stokes equations, by replacing viscous effects with the results of boundary layer theory [16] for the cylindrical pipeline setup. Specifically, the viscosity of water induces friction at the pipeline border. The corresponding effect on the fluid momentum is approximated by the Darcy-Weisbach law, cf. (2.4) and included in $k(v, e)$. Finally, (2.1c) describes the balance of internal energy subject to a source term $c(e)$ describing thermal losses of the fluid to the pipeline environment. Different representations exist for the energy balance, depending on the notion of energy. Eq. (2.1c) can equivalently be written as a balance law for the total energy including a kinetic part $E^{\text{kin}} = e + 1/2 \rho v^2$ or the total enthalpy density $E^h = E^{\text{kin}} + p$. The right side of (2.1c) changes accordingly. When using the enthalpy density as modeling variable, the contribution of k to the momentum balance also enters the enthalpy balance. Within this thesis, the internal energy density is chosen since it allows a convenient transition to the incompressible case. Eq. (2.1) introduces the pressure $p : (0, L) \times (t_0, t_{\text{end}}] \mapsto \mathbb{R}$ as additional modeling variable. To close the system (2.1), an equation of state relates the quantities pressure, density and temperature (expressed by the energy density). It is discussed in further detail in section 2.1.2. Eqs. (2.1) represent hyperbolic Euler-like equations. While the original Euler equations describe inviscid fluids, (2.1) include an additional expression resulting

from the viscosity of water. The viscosity of water apart from the boundary layer is neglected, removing the diffusive transport of heat within the fluid. According to the database [30], the corresponding thermal diffusivity D_T of water at 5 bar pressure in the temperature range $50 - 120^\circ\text{C}$ takes values within $D_T \in [1.56, 1.71] \times 10^{-7} \text{ m}^2\text{s}^{-1}$. Assuming typical velocities of 10^{-1} ms^{-1} , and pipeline lengths of $L = 1 \text{ m}$, the resulting Péclet number measuring the ratio of advective and diffusive energy heat transport $\text{Pe} = vL/D_T$ is in the order 10^6 . Finally, heat transfer by radiation is not modeled either.

Incompressible limit

The technical operation conditions ensure by a sufficiently high absolute pressure level that water as the transport medium remains in the liquid phase. Hence, the incompressible case is additionally assumed. Thus, the transport of information through water within the network is modeled to happen instantaneously. Eqs. (2.1) then simplify to

$$\partial_x v = 0, \quad (2.2a)$$

$$\rho \partial_t v = -\partial_x p - \rho k(v, e), \quad (2.2b)$$

$$\partial_t e + v \partial_x e = -c(e). \quad (2.2c)$$

The conservation of mass reduces to the incompressibility constraint with the pressure acting as a Lagrange multiplier. The balance law for the energy density represents an advection equation subject to the source term c . To estimate the relevant flow regime, the Reynolds number is an estimate for the typical operation conditions of heating networks. It is defined by

$$\text{Re} = \frac{|v|d\rho}{\mu},$$

where μ refers to the dynamic viscosity. We assume a typical velocity of $v = 0.1 \text{ m s}^{-1}$, a pipeline diameter $d = 0.06 \text{ m}$, and a pressure of $p = 5 \text{ bar}$. At the temperature $T = 70^\circ\text{C}$, a density of $\rho \approx 978 \text{ kg m}^3$ results and a dynamic viscosity of $\mu \approx 4 \times 10^{-4} \text{ Pa s}$. This leads to a Reynolds number of $\text{Re} = 1.45 \times 10^4$. For the conditions relevant in district heating networks, the kinematic viscosity $\nu = \mu\rho^{-1}$ decreases with increasing temperature. Thus, the Reynolds number further increases and the flow in pipelines with typical velocities is turbulent.

2.1.2 Material laws and state equations

In this part, material laws and state equations are presented, which are suitable for the description of heating networks.

The sink term in (2.1c) describing the conduction of thermal energy with temperature T towards the ground with temperature T_∞ by imperfect isolation of the pipeline walls is modeled by [31, 32],

$$c(e) = \frac{4}{d}k_W(T(e) - T_\infty). \quad (2.3)$$

Here, k_W is the heat transfer coefficient, $[k_W] = \text{W K m}^{-2}$, and d the pipeline diameter. Both coefficients are supplied by the operator of the heating networks and thus are known. For the temperature range relevant for heating networks it holds that the temperature is a strictly monotone function of the internal energy density,

$$\partial_e T > 0, \quad T \in [50, 150]^\circ\text{C}, \quad p = 5 \text{ bar},$$

allowing to transform between both quantities.

The external forces shaping the change of pressure along a pipeline exhibit gravitational and frictional contributions,

$$k(q, e) = g\partial_x z + \frac{\lambda(v, e)}{2d}|v|v. \quad (2.4)$$

In the first part, g denotes the gravitational constant, and z_x the slope of the pipeline with respect to the ground level. The second part describes friction of the fluid with the pipeline wall resulting from viscosity and is referred to as the empirical Darcy-Weisbach law. The friction factor λ is a function of the Reynolds number and the ratio of roughness σ and diameter d of the pipeline. For turbulent flows in pipelines, a common model for λ is given by the Colebrook-White equation [6, 33],

$$\frac{1}{\sqrt{\lambda}} = -2\log_{10} \left(\frac{\sigma}{3.71d} + \frac{2.51}{\sqrt{\lambda}\text{Re}} \right) = -2\log_{10} \left(\frac{1}{d} \left[\frac{\sigma}{3.71} + \frac{2.51\mu(T)}{\sqrt{\lambda}|v|\rho(T)} \right] \right), \quad (2.5)$$

where the Reynolds number was inserted explicitly in the second part of the equation. Eq. (2.5) approximates the influence of frictional losses in pipelines, interpolating the transition between the smooth ($\sigma = 0$) and rough ($\sigma \rightarrow \infty$) case. This allows to derive $\lambda \geq 0$, and from the partial derivatives $\partial_d \lambda < 0$, and $\partial_v \lambda < 0$. For the Darcy-Weisbach law it holds that

$$a_r = \frac{\lambda}{2d}v|v|,$$

where a_r is the external influence to acceleration by friction. Thus, frictional forces decrease monotonically with increasing pipe diameter d .

State equations

For the Euler-like equations (2.2) combined with the mentioned constitutive equations, expressions for the viscosity, mass density and temperature of water have to be defined.

At the relevant pressure levels of heating networks applied to water as the transport medium, these quantities are assumed to be independent of pressure. Thus they can be modeled by a polynomial relation to the energy density

$$\rho = \rho(e), \mu = \mu(e), T = T(e),$$

where the polynomial coefficients are fitted to measurements [30]. Alternatively, a formal derivation of the corresponding state equations can be performed by modeling the entropy s of the system using an additional balance law. Temperature and pressure are then defined by the corresponding Gibbs relation. In contrast, this introduces a significant additional computational complexity compared to the evaluation of polynomials defined a-priori.

2.1.3 Coupling conditions on the network

In a network setting consisting of nodes and edges, coupling conditions have to be posed, defining how flows of edges entering a node constitute to flows exiting the node. A node or junction is a network element at which multiple edges interact. The required coupling conditions are of algebraic type and are derived from claiming the conservation of mass and energy at the node. For a formal description of the well-posedness of hyperbolic systems on networks see [23, 24, 25]. Subsequently, a network description for heating networks is discussed using the standard notation used for gas networks [34].

The network of pipelines is described as an oriented graph $\mathcal{G} = (\mathcal{N}, \mathcal{E})$ with nodes \mathcal{N} and edges \mathcal{E} . Its orientation serves as a reference to define the direction of flow quantities such as volume flow, mass flow, and velocity. A non-negative flow is oriented with the reference orientation, a negative flow is oriented opposite to the reference orientation. The set of edges $\mathcal{E} = \mathcal{P}^F \cup \mathcal{C} \cup \mathcal{P}^R \cup \mathcal{S}$ contains $|\mathcal{E}|$ edges which represent the union of pipelines in the flow network \mathcal{P}^F , pipelines in the return network \mathcal{P}^R , edges representing consumers \mathcal{C} , and the source \mathcal{S} also referred to as power plant or depot. With $\mathcal{P} = \mathcal{P}^F \cup \mathcal{P}^R$ the set of all pipelines is denoted. The considered time domain is abbreviated by $\mathcal{T} = [t_0, t_{\text{end}}]$.

In the incompressible case, the volume flow $q : (t_0, t_{\text{end}}] \mapsto \mathbb{R}$ is a suitable description variable, since it is constant in space for a given edge within the network, $a \in \mathcal{E}$. For the set of pipelines \mathcal{P} , it is formed by $q = \Phi v$, involving cross section Φ and velocity v . For heat exchangers \mathcal{C} and the source it is measured directly. To connect incoming and outgoing pipelines within the network, additional algebraic constraints at the junctions have to be posed. First, the conservation of the flow η over node k is defined,

$$\sum_{\alpha \in \delta^{\text{out}}(k)} \eta(\rho, q_\alpha) = \sum_{\alpha \in \delta^{\text{in}}(k)} \eta(\rho, q_\alpha), \quad (2.6)$$

where η is a placeholder for either the mass flow $\hat{q}(t, x) = \rho(t, x)q(t)$ or the volume flow q . While for both possibilities the energy transport along the network is well-

defined, different physical interpretations result. When the density ρ is allowed to change with the internal energy, conservation of mass and volume flow over node k are not identical, and the conservation of mass is the physically correct description. In contrast, the volume flow q proves to fit the numerical scheme derived in chapter 3 and thus replaces the mass flow $\eta = q$. Conservation of volume over node k is identical to conservation of mass in the limit that the temperatures of all flows coupling to node k are identical. To distinguish the consequences for the network model, conservation of mass and volume are equally discussed until spatial discretizations of the Euler equations are introduced. The sets $\delta^{\text{in}}(k)$ ($\delta^{\text{out}}(k)$) denote edges entering (exiting) node k according to the reference orientation, and are formally defined as

$$\begin{aligned}\delta^{\text{in}}(k) &:= \{ a \in \mathcal{E} : \exists m \in \mathcal{N} \text{ with } a = (m, k) \}, \\ \delta^{\text{out}}(k) &:= \{ a \in \mathcal{E} : \exists m \in \mathcal{N} \text{ with } a = (k, m) \}.\end{aligned}\tag{2.7}$$

In addition, the subsets \mathcal{I}_k , and \mathcal{O}_k are defined, containing edges with a volume flow effectively entering and exiting node k . These are formally defined as

$$\begin{aligned}\mathcal{I}_k &:= \{ a \in \delta^{\text{in}}(k) : q_a > 0 \} \cup \{ a \in \delta^{\text{out}}(k) : q_a < 0 \}, \\ \mathcal{O}_k &:= \{ a \in \delta^{\text{in}}(k) : q_a \leq 0 \} \cup \{ a \in \delta^{\text{out}}(k) : q_a \geq 0 \}.\end{aligned}\tag{2.8}$$

Depending on the sign of the volume flow, these sets can change dynamically. The conservation of energy over node k within the time $t \in \mathcal{T}$ is described by

$$\sum_{\alpha \in \delta^{\text{out}}(k)} q_\alpha(t) e_\alpha(t, 0) = \sum_{\alpha \in \delta^{\text{in}}(k)} q_\alpha(t) e_\alpha(t, L_\alpha),\tag{2.9a}$$

$$e_a(t, 0) = e_k(t), \quad a \in \mathcal{O}_k,\tag{2.9b}$$

where (2.9a) claims that the sum of incoming and outgoing energy flows are equal. In addition, (2.9b) defines the energy density exiting node k by claiming that incoming energy densities mix instantaneously, cf. fig. 2.2. This forms a virtual energy density $e_k(t)$ at node k . To ensure a well-defined pressure p_k at node k , continuity of the

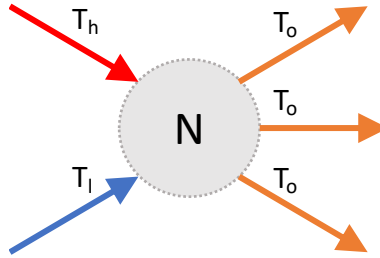


Figure 2.2: Illustration of the mixing assumption. Two pipelines with high T_h and low T_l temperature levels mix their energy densities within node k to $e(T_o)$ identical for all outgoing pipelines.

pressure at the border of every edge attached to k is claimed for $t \in \mathcal{T}$,

$$p_k(t) = p_a(0, t), \quad k \in \mathcal{N}, \quad a \in \delta^{\text{out}}(k),\tag{2.10a}$$

$$p_k(t) = p_a(L_a, t), \quad k \in \mathcal{N}, \quad a \in \delta^{\text{in}}(k).\tag{2.10b}$$

To close the network description, boundary conditions are required, describing the energy density and the pressure levels at the power plant, as well as at the consumption points. The latter are described in the following section in addition to the technical operation conditions.

2.1.4 Network boundary conditions: source and consumers

The technical operation conditions [35] presented hereafter are partially formulated in temperatures T instead of energy densities for consistency with the data supplied by the plant operator. Using the corresponding state equations, temperature restrictions can be transformed to energy densities and vice versa.

The depot, also referred to as power plant or source is modeled by an edge $s = (k, m) \in \mathcal{S}$ directed from return to the flow part of the network, and equipped with the following equations for times $t \in \mathcal{T}$,

$$e_{s:m}(t) = u_F(t), \quad (2.11a)$$

$$p_{s:k}(t) = p_R(t), \quad (2.11b)$$

$$p_{s:m}(t) = p_{s:k}(t) + \Delta p_s(t), \quad (2.11c)$$

$$T_{s:m}(t) \leq T_{\max}^{\text{net}}, \quad (2.11d)$$

$$v_s(t) \geq 0. \quad (2.11e)$$

Eq. (2.11a) sets the energy density injected at the source u_F to the flow network, whereas (2.11b, 2.11c) define the pressure levels at the flow- and return site of the power plant. We specifically assume that the pressure in the return part is defined as control variable, as well as the pressure difference of flow- and return part of the source. Eqs. (2.11d - 2.11e) are technical operation conditions requiring that the temperature injected to the network is limited, and that the source flow is directed into the flow network. In a real depot, the exchange of energy with the heating network is performed by a cascade of heat exchangers. Furthermore, the regulation of pressure levels is achieved by pumps. All of these components are condensed into the a source edge $s \in \mathcal{S}$. A more detailed model of the components on the depot is not within the scope of this work. While multiple injection points are possible and occur in distinct heating networks, within this thesis the interaction with a single source is considered.

Consumers in heating networks are modeled as an edge $a = (k, m) \in \mathcal{C}$. The exchange of energy with the heating network is realized by a heat exchanger, cf. fig. 2.3, described for times $t \in \mathcal{T}$ by the following set of equations,

$$G_a(t) = q_{a:k}(t)e_{a:k}(t) - q_{a:m}(t)e_{a:m}(t), \quad (2.12a)$$

$$\hat{q}_{a:k}(t) = \hat{q}_{a:m}(t), \quad (2.12b)$$

$$T_{a:m}(t) = T_a^R, \quad (2.12c)$$

$$v_a(t) \geq 0, \quad (2.12d)$$

$$T_{a:k}(t) \in [T_{min}^F, T_{max}^F], \quad (2.12e)$$

$$T_{a:k}(t) \leq T_{a:m}(t) + \Delta T_a^c, \quad (2.12f)$$

$$p_{a:k}(t) \in [p_{min}^F, p_{min}^F], \quad (2.12g)$$

$$p_{a:m}(t) \in [p_{min}^R, p_{max}^R], \quad (2.12h)$$

$$p_{a:k}(t) - p_{a:m}(t) \in [\Delta p_{min}^c, \Delta p_{max}^c]. \quad (2.12i)$$

The demanded power consumption G is provided by the power balance between flow-

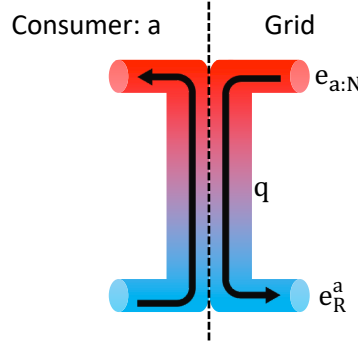


Figure 2.3: Illustration of the heat exchanger for consumer arc $a = (k, m)$.

and return side of the heat exchanger, formed by the product of energy densities e , and volume flows evaluated at flow- and return side (2.12a). The corresponding volume flows are defined by assuming conservation of mass along the heat exchanger (2.12b). Consequently, both velocity and volume flow change dynamically with the energy density $e_{a:k}$ arriving in the flow part of consumer stations and their time dependent consumption G . Heat exchangers are constructed to cool the hot fluid to a contractually defined constant return temperature set in (2.12c), resulting in the return energy density e_R^a . Injected at the return part of consumer stations, the cooled fluid propagates in the return network to the power plant, and is reheated again. The model for the power exchange at heat exchangers is in line with [36, 29], where the heating power is approximated by $\hat{q}c_p T$, with c_p denoting the specific heat capacity at constant pressure, \hat{q} the mass flow and T the temperature. Model (2.12) could be extended to incorporate heat losses, i.e. to model a primary and secondary network formed by the heating network and the consumer [11].

In contrast, in this thesis an emphasis is set to the transport of energy within pipelines. For this purpose, (2.12a) already reveals the fundamental mathematical complexity:

the volume flow entering and exiting each heat exchanger is altered by the energy density at the end of the flow network. Without heat losses, the power demanded by a consumption point is identically extracted from the network at every point of time. To fit the conservation of volume at nodes, which is mainly used within this thesis, a lower model hierarchy for the power balance results from claiming conservation of volume along the heat exchanger

$$G_a(t) = q_a(t)(e_{a:k}(t) - e_{a:m}(t)). \quad (2.13)$$

For the case of a constant density conservation of mass and volume agree, and hence (2.12a) and (2.13) agree, as well. Eq. (2.12d - 2.12i) are technical operation conditions formally not relevant to define the dynamics. In (2.12d), the energy transport is required to lead from the heating network to the consumption. For a negative velocity, heat exchangers would contribute power to the heating network rather than obtaining it. So called prosumers are planned to be investigated in future projects and are not part of this thesis. The temperature arriving at the flow part of consumer stations is restricted to lower and upper values (2.12e) and the temperature difference is bounded by (2.12f). Eq. (2.12d - 2.12f) can be fulfilled simultaneously by defining an appropriate domain for the energy density at the flow part of consumer stations. For practical applications it holds that $T_{min}^F > T_a^R$ leading to $e_{a:k} > e_R^a$. This ensures that the resulting volume flow is finite for finite consumption powers G .

In addition to the technical operation conditions discussed for heat exchangers and the source, the minimum and maximum pressure level at each network node is restricted as well,

$$p_{\min}^{\text{net}} \leq p_k(t) \leq p_{\max}^{\text{net}}, \quad k \in \mathcal{N}, \quad t \in \mathcal{T}.$$

The minimum pressure bound ensures that the fluid indeed remains in the fluid phase. The presented restrictions to temperatures and energy densities on the network can be condensed to a single set of admissible values for the PDE variable,

$$\mathcal{X}^e := \{e_{\alpha}^{\min}(x) \leq e_{\alpha}(t, x) \leq e_{\alpha}^{\max}(x), \quad t \in \mathcal{T}, \quad x \in [0, L_{\alpha}], \quad \alpha \in \mathcal{P}\}, \quad (2.14)$$

where $x \in [0, L_{\alpha}]$ refers to the spatial domain of pipeline α in local coordinates. For typical networks, the resulting borders e_{\min}, e_{\max} are constant on every location x within the network. The space of admissible node pressures is not relevant for a well-defined simulation but poses technical restrictions. These are discussed in chapter 6.

2.2 Elimination of algebraic equations

While the set of algebraic equations presented in section 2.1.3 is complete and allows to solve for the incompressible dynamics of heating networks, its solution can be simplified by eliminating algebraic constraints. Eqs. (2.6, 2.9a) recover a constraint similar to Kirchhoff's current law for electrical circuits. The underlying time invariant network

structure is what shall be eliminated in the following. Starting with the conservation of energy, combining (2.9) yields an expression for the energy leaving node k ,

$$e_k(t) = \frac{\sum_{a \in \mathcal{I}_k} q_a(t) e_j(t, L_a)}{\sum_{a \in \mathcal{O}_k} q_a(t)}, \quad t \in \mathcal{T}. \quad (2.15)$$

Thus the solution of energy conservation reduces to the determination of in- and outgoing edges and the evaluation of (2.15).

Eq. (2.6) claims the conservation of volume or mass. In both cases, it forms a linear system of equations for the volume flows on each node in the network. For conservation of volume it reads

$$Kq = 0, \quad (2.16)$$

where $K \in \mathbb{R}^{N \times |\mathcal{E}|}$ is the weighted incidence matrix of the graph \mathcal{G} . For volume conservation, the absolute value of the weights of K are constantly 1. For mass conservation, (2.16) can be replaced by an incidence matrix $K'(\rho)$ with weights given by the value of the densities at pipelines ends. In a connected graph, one of the equations posed by all nodes is redundant, leading to an undetermined system with $|\mathcal{L}_{\mathcal{G}}| = |\mathcal{E}| - (N - 1)$ independent volume flows q_I . Here, $|\mathcal{L}_{\mathcal{G}}|$ denotes the number of linear independent cycles of the graph \mathcal{G} . A cycle is defined as a nonempty, closed path of edges, in which the only repeated node is the starting node [37]. A visualization is presented in fig. 2.4. By construction of the flow and return network, each consumer edge leads

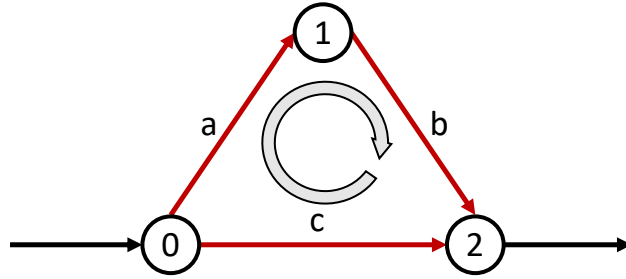


Figure 2.4: Illustration of a network cycle. The path $0 - 1 - 2 - 0$ including the red edges $\{a, b, c\}$ is closed with node 0 as the only repeated node.

to one cycle. The set of consumer cycles shall be denoted by \mathcal{L}_c . Additional cycles are introduced by the topology of the flow- and return network and are denoted by $\mathcal{L}_{\mathcal{G}}$. The determination of the independent flow variables q_I can now be achieved by solving a nonlinear system of equations for each cycle. For volume flows representing consumer cycles, this is performed by solving (2.13). To obtain a constraint for network cycles, the structure of (2.10) is analyzed subsequently. Summing the pressure differences at pipelines along a cycle in a network yields

$$\sum_{a \in \xi} \Delta p_a = 0, \quad \xi \in \mathcal{L}_{\mathcal{G}}, \quad (2.17)$$

in analogy to Kirchhoff's second law for electrical circuits. Integrating the conservation of momentum in space along a pipeline leads to

$$\Delta p = -\bar{\rho}\dot{v} - \overline{\rho k(q, e)}. \quad (2.18)$$

Here, $\bar{y} := \int y(x) \, dx$ marks the integral along the pipeline for the quantity y . In addition, in (2.18) the "dot" notation was used to express the total temporal derivative of a quantity in compact form. Applying Kirchhoff's second law (2.17) to the pressure differences defined in (2.18) yields the constraint (2.19), which allows to solve for the volume flows representing network cycles,

$$\sum_{a \in \xi} \bar{\rho}_a \dot{v}_a + \overline{\rho k(q, e)}_a = 0, \quad \xi \in \mathcal{L}_G. \quad (2.19)$$

Flow-defining equations

The set of flow-defining equations for times $t \in \mathcal{T}$ is thus given by

$$Kq(t) = 0, \quad (2.20a)$$

$$\Phi_\alpha(t)v_\alpha(t) = q_\alpha(t), \quad \alpha \in \mathcal{P}, \quad (2.20b)$$

$$G_a(t) - q_a(t)(e_{a:k}(t) - e_{a:m}(t)) = 0, \quad a = (k, m) \in \mathcal{C}, \quad (2.20c)$$

$$\sum_{a \in \xi} \bar{\rho}_a(t)\dot{v}_a(t) + \overline{\rho k(q, e)}_a = 0, \quad \xi \in \mathcal{L}_G. \quad (2.20d)$$

As a consequence, the determination of $|\mathcal{E}|$ volume flows is essentially reduced to a system of $|\mathcal{L}_G|$ nonlinear equations. Furthermore, after application of (2.19), the pressure variable does not enter the set of equations defining the flow field. After solving (2.20), the pressure can be recovered by evaluating (2.18). Still, the absolute pressure levels define technical operating restrictions and have to be considered for an optimization discussed in chapter 6. An import simplification arises from neglecting the acceleration contribution in the momentum balance (2.2b) of the Euler-like equations. This leads to

$$0 = \partial_x p + \rho k(v, e).$$

This transforms the flow-defining equations (2.20) to a purely algebraic system. While this assumption affects the solution of cycle representing flows, the volume flows at consumers stations remain identical without incorporating the acceleration. Due to the direct influence of consumer stations (2.20c) on the flow field, the flow-defining equations without the acceleration contribution remain non-stationary.

2.3 Hydrodynamic equations

Hereafter, the flow defining equations (2.20) and their solutions are studied. Depending on the considered network topology, the complexity of (2.20) varies, cf. fig. 2.5. For the

visualized network (a), the volume flow field is defined by the volume flow extracted by consumers (with fixed orientation) and the conservation of volume. If a cycle with one inflowing and one outflowing pipeline exists (b), pressure continuity introduces a nonlinear equation defining a flow on the cycle, which remains in the same solution branch independent of the size of the external flows, assuming that the external flows retain their orientation. Finally, if a cycle contains multiple effectively inflowing or multiple effectively outflowing pipelines (c), the solution branch changes depending on the relative size of the external flows.

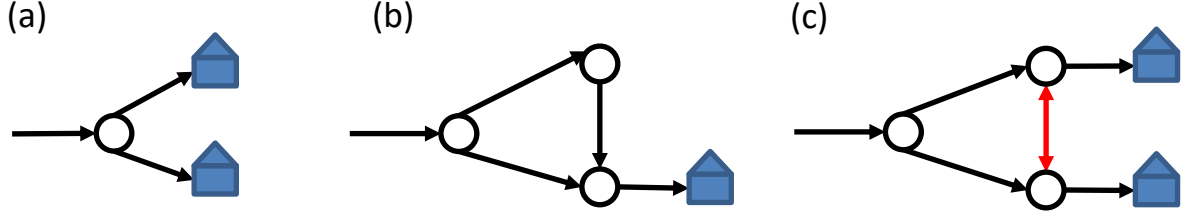


Figure 2.5: Three stages of complexity for the flow defining equations. The three networks contain either no cycle (a), a cycle with one inflowing and one outflowing pipeline (b), and finally a cycle with one inflowing and multiple outflowing pipelines. The last example allows for a change of flux direction on the red edge depending on the volume flow of both houses.

Cycle flow including changes of flow directions

In this part the solution of Kirchhoff's voltage law (2.19) is studied, focusing on the quasi-stationary case. To consider a general setup, the effect of changes of flux directions is included. To illustrate the setting, fig. 2.6 shows a minimum working example of a network exhibiting a change in the flux direction between nodes 2-3. For a single cycle ξ from the set of network cycles $\mathcal{L}_{\mathcal{G}}$, the nonlinear equations defining the flow $q_3 = q_L$ which is chosen to represent the cycle is given by

$$\sum_{a \in \xi} o_a \left(\bar{\rho}_a \dot{v}_a + g \bar{\rho}_a \partial_x z_a + \frac{\bar{\lambda} \rho_a}{2d_a} v_a |v_a| \right) = 0, \quad (2.21)$$

where o_a equals 1 if the pressure difference is taken with the topological orientation and -1 else. Note that the velocity v_a is positive, if its vector is in line with the topological orientation. Considering the case without acceleration ($\dot{v} = 0$), and assuming that the integral of the density along each pipeline is identical yields

$$\frac{\bar{\lambda} \rho_1}{2d_1} v_1 |v_1| + \frac{\bar{\lambda} \rho_3}{2d_L} v_L |v_L| = \frac{\bar{\lambda} \rho_2}{2d_2} v_2 |v_2|, \quad (2.22)$$

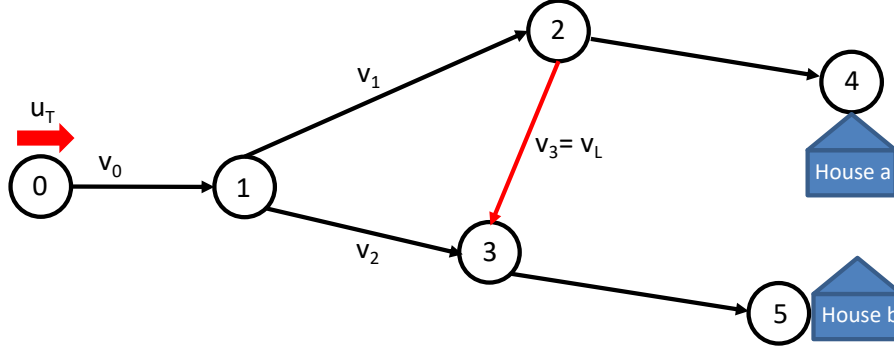


Figure 2.6: Example for a network which can undergo a change of flux direction on pipeline 2-3.

since the height differences along a closed path sum to zero. Eliminating the velocities by their corresponding volume flows and inserting conservation of volume results in

$$\alpha_1(h_a + q_L)|h_a + q_L| + \alpha_L q_L |q_L| = \alpha_2(h_b - q_L)|h_b - q_L|,$$

where h_a, h_b are volume flows of the two houses and q_i , $i \in \{1, L, 2\}$ denote the volume flow in the corresponding pipelines. We additionally assume that friction coefficient and density are constant values on each pipeline, irrespective of velocity and energy density. For the case of identical constants α_i , $i \in [1, L, 2]$ the result can be written as

$$q_L(h_a, h_b) = \begin{cases} -h_a - h_b + \sqrt{2}\sqrt{h_b(h_a + h_b)} & : h_b \geq h_a \\ h_a + h_b - \sqrt{2}\sqrt{h_a(h_a + h_b)} & : h_b < h_a \end{cases}. \quad (2.23)$$

In the first case, q_L is positive, in the second case negative. Notably, the volume flow undergoing a change of the flux direction is a continuous function of the external flows h_a, h_b for this example. The full solution of the hydraulic problem for the case $h_b \geq h_a$ reads

$$\begin{aligned} q_0 &= h_a + h_b \\ q_1 &= h_a + q_L = -h_b + \sqrt{2}\sqrt{h_b(h_a + h_b)} \\ q_L &= -h_a - h_b + \sqrt{2}\sqrt{h_b(h_a + h_b)} \\ q_2 &= h_b - q_L = h_a + 2h_b - \sqrt{2}\sqrt{h_b(h_a + h_b)} \end{aligned}$$

This can also be written split in a linear relation to the house flows and an additional nonlinear function to each equation,

$$\begin{pmatrix} q_0 \\ q_1 \\ q_L \\ q_2 \end{pmatrix} = \begin{pmatrix} 1 & 1 \\ 0 & -1 \\ -1 & -1 \\ 1 & 2 \end{pmatrix} \begin{pmatrix} h_a \\ h_b \end{pmatrix} + \sqrt{2}\sqrt{h_b(h_a + h_b)} \begin{pmatrix} 0 \\ 1 \\ 1 \\ -1 \end{pmatrix}.$$

In case one of the houses exhibits a zero flux or both demands are identical, all relations become linear. This trivially explains that cycles exist, in which a change of flux direction is not possible. Removing one of the houses in fig. 2.6, the flow directions of all paths in the presented cycle are invariant in time due to the pressure continuity.

Existence of circular velocity fields

Hereafter, we analyze the existence of a circular velocity field within a cycle. Starting at an arbitrary node within a cycle and following the flow direction of the velocity fields within the cycle, a circular velocity field is characterized by the fact that the starting node is reached again. It shall be noted that such velocity fields can only exist by differences in the density distribution on each pipeline. If all densities are equal, as assumed in water- and gas networks, the sum over height differences along a cycle cancels to 0. The remaining frictional forces exclude a circular velocity field.

We consider (2.22) and aim at finding a solution in which pipeline 2 flows from node 3 to 1, for the presented orientations of pipelines 1 and 3, which would generate a circular velocity field. We introduce height levels of nodes 1,2,3 and assume equal pipeline diameters on each pipeline. For these assumptions, (2.21) reads

$$\frac{1}{2(\frac{\pi}{4})^4 d^5} (\lambda_1 \bar{\rho}_1 q_1 |q_1| + \lambda_L \bar{\rho}_L q_L |q_L| + \lambda_2 \bar{\rho}_2 q_2 |q_2|) + g(\bar{\rho}_1 \partial_x z_1 + \bar{\rho}_L \partial_x z_L + \bar{\rho}_2 \partial_x z_2) = 0,$$

where velocities are expressed by volume flows. Pipeline 1 is modeled by a positive slope $\partial_x z_1$, while pipelines 2 and 3 share an identical, negative slope $\partial_x z_1 = -2\partial_x z_L = -2\partial_x z_2$. In addition, we assume that the friction factors are constant along each pipeline and that the integrated densities on pipelines 2,3 are identical by appropriate temperature levels, $\bar{\rho}_L = \bar{\rho}_2$. Using these assumptions as well as conservation of volume at each node yields

$$\frac{1}{2(\frac{\pi}{4})^4 d^5} (\lambda_1 \bar{\rho}_1 (h_a - q_L) |h_a - q_L| + 2\lambda_L \bar{\rho}_L q_L |q_L|) + g\partial_x z_1 (\bar{\rho}_1 - \bar{\rho}_L) = 0. \quad (2.24)$$

At a pressure of $p = 5$ bar, and temperatures $T_1 = 120^\circ\text{C}$, $T_L = 60^\circ\text{C}$, the corresponding densities read $\rho_1 = 943 \text{ kg m}^3$, $\rho_L = 983 \text{ kg m}^3$. When modeling the friction factors by the Colebrook-White equation (2.5) for the given roughness $\sigma = 0.047 \text{ mm}$, (2.24) yields no solution in which pipeline 2 is oriented from 3 to 1. In addition, fixing the house flow h_a to a volume flow leading to a velocity of 0.1 m s^{-1} , (2.24) could be solved for a globally constant friction factor. It turns out that the corresponding global friction factor leading to a positive flow on pipeline 2 is $\lambda = 2.6$. This value is at least on order of magnitude above realistic friction factors for turbulent flows.

Remark 1. *Due to the results presented in this section, we assume that all velocity fields solving the flow-defining equations (2.20) including pressure continuity, exclude circular velocity fields. This assumption is used in the analysis of asymptotic stability in section 3.6.3 and in the spectrum of the system operator presented in section 3.7.*

Convexity of independent volume flows

To close the discussion of the flow defining equations, a statement on the convexity of the independent volume flows is made. Since the power consumption is bounded by

$G^a(t) \in [G_-^a, G_+^a]$, $a \in \mathcal{C}$, $t \in \mathcal{T}$, and the energy densities at consumer stations are bounded as well, $e_a(t) \in [e_{\min}^F, e_{\max}^F]$, $t \in \mathcal{T}$, the volume flows at consumer stations are bounded by

$$q_a(t) \in \left[\frac{G_-^a}{e_a(t) - e_{\max}^F}, \frac{G_+^a}{e_a(t) - e_{\min}^F} \right], \quad a \in \mathcal{C}, \quad t \in \mathcal{T}.$$

As a consequence, for fixed points in time t^* , the set of admissible volume flows at consumers stations is convex. In contrast, due to the nonlinear contribution of friction to the pressure difference in the momentum equations, the cycle flows are in general not a convex function of the volume flows at consumers. This means that a convex combination of all independent flows will not form a solution of the hydrodynamic equations. A counter example confirming the claim is presented above, in which $q_3(h_a, h_b)$ defined in (2.23) is not a convex function in h_a, h_b . This can be seen by evaluating the Hessian of $q_3(h_a, h_b)$. For the branch $h_b \geq h_a > 0$, it has the eigenvalues

$$\begin{aligned} \lambda_1 &= 0, \\ \lambda_2 &= \frac{-(h_a^2 + h_b^2)}{4(h_b(h_b + h_a))^{3/2}}. \end{aligned}$$

2.4 Basic PDE model

The PDE model presented in this chapter is summarized below. The technical restrictions valid for consumer stations and the power plant lead to the restriction of the energy density \mathcal{X}^e defined in (2.14). Within this thesis, a lower model hierarchy for the transport of thermal energy is studied. Specifically, the influence of thermal losses at every pipeline is neglected, $k_W \rightarrow 0$. Consequently, for times $t \in \mathcal{T}$ the transport dynamics are described by

$$\partial_t e_\alpha(t, x) = -v_\alpha(t) \partial_x e_\alpha(t, x), \quad \alpha \in \mathcal{P}, \quad x \in [0, L_\alpha], \quad (2.25a)$$

$$e_k(t) = \frac{\sum_{a \in \mathcal{I}_k} q_a(t) e_a(t, L_a)}{\sum_{a \in \mathcal{O}_k} q_a(t)}, \quad k \in \mathcal{N}, \quad (2.25b)$$

$$e_{s:k}(t) = u_F(t), \quad s = (k, m) \in \mathcal{S}, \quad (2.25c)$$

$$e_{c:m}(t) = e_R^c, \quad c = (k, m) \in \mathcal{C}. \quad (2.25d)$$

While the effect of thermal losses is central for low environmental temperatures, the remaining model hierarchy still contains the fundamental difficulties in deriving a reduced order model. System (2.25) consists of purely advection dominated, hyperbolic partial differential equations (PDE) formulated on a network. In addition, the advection speed changes as a function of time depending on the solution of the energy density evaluated at the network end. Thus, the remaining transport dynamics are still effectively nonlinear in the energy density when eliminating the velocity as a state variable. The vector of return energy densities e_R will also be abbreviated as the vector $u_R \in \mathbb{R}^{|\mathcal{C}|}$

$$(u_R)_c := e_R^c, \quad c \in \mathcal{C},$$

expressing that the return energy densities are inputs to the return network, yet not controllable. The second component of the PDE model defines the advection velocity on every pipeline. For times $t \in \mathcal{T}$, these velocities are given by

$$Kq = 0, \tag{2.26a}$$

$$\Phi_\alpha v_\alpha = q_\alpha, \quad \alpha \in \mathcal{P}, \tag{2.26b}$$

$$G_a = q_a(e_{a:k} - e_{a:m}), \quad a = (k, m) \in \mathcal{C}, \tag{2.26c}$$

$$\frac{1}{\rho_\alpha} \partial_x p_\alpha = -\dot{v}_\alpha - \frac{\lambda(v_\alpha, e_\alpha)}{2d_\alpha} v_\alpha |v_\alpha| - g \partial_x z_\alpha, \quad \alpha \in \mathcal{P}, \ x \in [0, L_\alpha] \tag{2.26d}$$

$$p_{s:m} = p_{s:k} + \Delta p_s, \quad s = (k, m) \in \mathcal{S}, \tag{2.26e}$$

$$p_{s:k} = p_R \quad s = (k, m) \in \mathcal{S}. \tag{2.26f}$$

Eq. (2.26a) denotes the conservation of volume at network nodes which will prove to suit the finite volume discretization used to form the ODE representation of the advection equations. As already mentioned, conservation of volume over network nodes is a good approximation to conservation of mass in case the temperature range of the flows coupling to the node is small. Specifically, for simple junctions in which one pipeline enters and one pipeline exits, mass- and volume conservation are identical. Still, parts within this thesis also comment the consequences of replacing (2.26a) by conservation of mass.

Chapter 3

DAE model

For the system of partial differential algebraic equations presented in chapter 2, a spatial discretization is performed, to allow for a numerical solution of the corresponding dynamics. As shown in section 2.2, the flow defining equations can be simplified significantly. Specifically, the pressure can be eliminated as an explicit variable. By incompressibility of the fluid, the velocity is spatially constant on each edge, motivating to discuss a spatial discretization of the advection of thermal energy. As will be discussed below, discretizing the thermal energy leads to the formulation of a control system, whose stability properties can be analyzed by means of the Lyapunov theory. Furthermore, existence and uniqueness of solutions for the control system are discussed. Finally, the relation of the model to the concept of port-Hamiltonian systems is analyzed. The following presentation discusses different numerical methods to solve hyperbolic PDEs and indicates their relation to the upwind scheme. It proves to be sufficiently simple in structure to derive a reduced order model, while possessing many desired properties of a numerical scheme for a hyperbolic PDE. As an alternative to reduced order models, higher order hyperbolic schemes also require a smaller number of discretization cells in space to obtain the same approximation of the underlying PDE compared to lower order schemes. ADER schemes have been successfully used to simulate blood flows and will thus be used as a benchmark in chapter 5.

3.1 Spatial discretization of advection dominated transport

Hereafter, we consider the model hierarchy introduced in section 2.4. Focusing on the advection based transport of energy, the PDE (2.25a) results on each pipeline, where the velocity changes as a function of time defined by the algebraic equations (2.26). Combining the local energy densities e_α , $\alpha \in \mathcal{P}$ to a global variable e , the PDE describing the entire set of pipelines reads

$$\partial_t e = -\partial_x F(t, e), \quad t \in \mathcal{T}, \quad (3.1a)$$

$$= -V(t) \partial_x e, \quad t \in \mathcal{T}, \quad (3.1b)$$

where $V \in \mathbb{R}^{|\mathcal{P}| \times |\mathcal{P}|}$ denotes the Jacobian matrix of the flux function F . It defines a diagonal matrix carrying the pipeline velocities on each diagonal element. As a consequence, (3.1) forms a system of hyperbolic equations, since V is diagonal and carries real eigenvalues represented by the advection velocities. As the velocities need not to be distinct, (3.1) is symmetric hyperbolic, yet not strictly hyperbolic. In addition, due to the time dependent flux function $F(t, e)$, (3.1) also constitutes a quasi-linear systems of hyperbolic PDEs. The conservation of energy (2.25b) relating pipelines at junctions in combination with (2.25c, 2.25d) define time-dependent boundary conditions for each pipeline.

Subsequently numerical schemes are discussed for solving the transport on a representative pipeline described by (3.2) on the domain $\Omega = [0, L] \subset \mathbb{R}^1$ in one spatial dimension. Numerical methods aim at solving (3.2) by discretizing the PDE in space and time, forming a two-dimensional grid for a spatial problem of one dimension [38]. The considered time interval $\mathcal{T} = [t_0, t_{\text{end}}]$ is discretized to $M \in \mathbb{N}$ discrete times t^j , $j \in [0, \dots, M-1]$, $t_0 = t^0$, $t_{\text{end}} = t^{M-1}$. The spatial domain is discretized by a partition of $n \in \mathbb{N}$ disjoint cells $I_i = [x_{i-1/2}, x_{i+1/2}]$, $i \in [0, \dots, n-1]$, with $\Omega = \cup_{i=0}^{n-1} I_i$. For the ease of discussion, equidistant meshes in space and time are considered, with the corresponding grid size $h = x_{i+1/2} - x_{i-1/2}$, $\forall i$, and $\delta_t = t^{j+1} - t^j$. The cell boundaries are thus located at $x_{i \pm 1/2} = 0 + (i + 1/2 \pm 1/2)h$, setting the left boundary of the first cell to the start of the domain $x = 0$.

Quasi-stationary description of the velocity field

The PDE (3.1) carries an explicit time dependence by the time dependent consumer function G . In addition, it depends on the energy densities evaluated at the “right” boundary of the spatial domain coupling to the consumer stations. Due to this fact, the time evolution of the velocity for a future time step is a function of the solution of the energy density to be determined. To solve this bidirectional relation between velocity and energy density, the velocity field at time t^j is assumed to be constant throughout the subsequent time step for an explicit time integration. This is in line with the approach used by explicit time integration schemes of ordinary differential equations (ODEs). Hence, in the subsequent discussion of the numerical methods, a piece-wise constant advection velocity is assumed. The following discussion considers the solenoidal transport of the energy density e on one pipeline within space $\Omega = [0, L]$ and time \mathcal{T} ,

$$\partial_t e + \partial_x f(t, e) = 0, \quad e(t_0, x) = e_0(x), \quad e(t, 0) = u_0(t). \quad (3.2)$$

The advection equation with time varying velocity is recovered by the flux $f(t, e) = v(t)e$,

$$\partial_t e + v(t)e = 0, \quad e(t_0, x) = e_0(x), \quad e(t, 0) = u_0(t). \quad (3.3)$$

3.1.1 Finite difference methods

Finite difference schemes approximate the true solution e of (3.2) at time t^j and space x_i by the quantity $\tilde{e}(t^j, x_i) = e_i^j$ at grid point (i, j) of the space-time grid. Assuming an equidistant mesh, the points at which the approximations are located are defined according to $x_i = 0 + (i + 1/2)h$, $i \in [0, \dots, n - 1]$. A popular finite difference method is given by the upwind scheme. For the time-varying advection equation it reads,

$$e_i^{j+1} = e_i^j - \frac{\delta_t}{2h}(|v^j| + v^j)(e_i^j - e_{i-1}^j) - \frac{\delta_t}{2h}(|v^j| - v^j)(e_i^j - e_{i+1}^j). \quad (3.4)$$

Eq. (3.4) can be interpreted as a first order finite difference approximation to the time- and space derivatives occurring in (3.2). It approximates the solution at point x_i and the future time layer t^{j+1} by a one-sided spatial approximation in the direction from which the information originated. An alternative approach are central schemes, in which the numerical domain influencing the future time step is symmetric. Two symmetric schemes often applied read

$$e_i^{j+1} = \frac{1}{2}(e_{i+1}^j + e_{i-1}^j) - \frac{\delta_t}{2h}v^j(e_{i+1}^j - e_{i-1}^j), \quad (3.5a)$$

$$e_i^{j+1} = e_i^j - \frac{\delta_t}{2h}v^j(e_{i+1}^j - e_{i-1}^j) + \frac{\delta_t^2}{2h^2}(v^j)^2(e_{i+1}^j - 2e_i^j + e_{i-1}^j). \quad (3.5b)$$

Eq. (3.5a) refers to the Lax-Friedrichs scheme, and (3.5b) to the Lax-Wendroff scheme [38]. Both the upwind and the Lax-Friedrichs scheme are of first order in time and space and thus the approximation error compared to the true solution of the PDE increases with h^{+1} . Since the Lax-Friedrichs scheme is a central scheme, applying it to advection dominated problems introduces additional numerical diffusion compared to the upwind scheme. The Lax-Wendroff scheme incorporates a second order approximation of the spatial derivative and is of second order in space and time. In exchange it introduces oscillations at sharp spatial gradients since it is not monotone. Sharp gradients can occur in heating networks allowing for changes of flux direction as discussed in chapter 5. Using a von Neumann stability analysis, the presented schemes are found to be stable on the domain of a single pipeline, if the Courant-Friedrichs-Levy (CFL) condition [38] is satisfied,

$$\frac{\delta_t}{h}|v^j| \leq 1. \quad (3.6)$$

Simulating all pipelines within a network simultaneously, every pipeline is updated in one time step and the most restrictive CFL condition has to be met,

$$\max_{p \in \mathcal{P}} \frac{\delta_t}{h_p}|v_p^j| \leq 1. \quad (3.7)$$

In addition, the presented schemes are conservative and exhibit a consistent flux function.

3.1.2 Finite volume methods

The discussion of finite volume schemes follows [38]. Finite volume schemes approximate the solution to (3.2) by means of finite volumes incorporated in I_i . Integrating (3.2) in space along cell I_i and along a time step yields

$$0 = \int_{x_{i-1/2}}^{x_{i+1/2}} \int_{t^j}^{t^{j+1}} \partial_t e \, dt \, dx + \int_{x_{i-1/2}}^{x_{i+1/2}} \int_{t^j}^{t^{j+1}} \partial_x f(t, e) \, dt \, dx, \quad (3.8a)$$

$$0 = \int_{x_{i-1/2}}^{x_{i+1/2}} e(t^{j+1}, x) - e(t^j, x) \, dx + \int_{t^n}^{t^{j+1}} f(t, e(t, x_{i+1/2})) - f(t, e(t, x_{i-1/2})) \, dt, \quad (3.8b)$$

$$U_i^{j+1} = U_i^j - \frac{\delta_t}{h} \left[\frac{1}{\delta_t} \int_{t^j}^{t^{j+1}} f(t, e(t, x_{i+1/2})) - f(t, e(t, x_{i-1/2})) \, dt \right], \quad (3.8c)$$

where $U_i^j = \frac{1}{h} \int_{x_{i-1/2}}^{x_{i+1/2}} e(t^j, x) \, dx$ is the normalized integral of e at time t^j along the finite volume I_i .

To solve (3.8c) numerically, the Godunov scheme uses a piece-wise constant approximation $\tilde{e}^j(t, x)$, which, at time t^j , is defined by $\tilde{e}^j(t^j, x) = \tilde{U}_i^j$, $x \in I_i$, where \tilde{U}_i^j is now interpreted as an approximation to the cell volume to be updated. Its initial value is defined by the initial condition $\tilde{U}_i^0 = \frac{1}{h} \int_{x_{i-1/2}}^{x_{i+1/2}} e_0(x) \, dx$. Its value for the subsequent time step has the form $\tilde{U}_i^{j+1} = \frac{1}{h} \int_{x_{i-1/2}}^{x_{i+1/2}} \tilde{e}^j(t^{j+1}, x) \, dx$. According to (3.8c), its evaluation requires to solve the Riemann problems defined by the flux functions at the cell boundaries $f(t, \tilde{e}^j(t, x_{i\pm 1/2}))$, $t \in [t^j, t^{j+1}]$. Limiting the time step by the ratio of the cell length and the maximum wave propagation speed of all cells ensures that the Riemann problems can be solved independently,

$$\delta_t \leq \max_l \frac{h}{\lambda_l(\partial_{U^j} f(t^j, U^j))}, \quad (3.9)$$

where λ_l denotes the eigenvalues of the Jacobian of the flux function, $\partial_{U^j} f(t^j, U^j)$. Evaluating it at time t^j results from the assumption that the velocity is constant within the time step $[t^j, t^j + \delta_t]$ and is not related to the Godunov scheme itself. As in the finite difference case, the CFL condition (3.9) has to be satisfied for all pipelines updated within the time step. The updated cell values at the new time step read

$$\tilde{U}_i^{j+1} = \tilde{U}_i^j - \frac{\delta_t}{h} \left[\frac{1}{\delta_t} \int_{t^j}^{t^{j+1}} f(t^j, \hat{e}^j(\tilde{U}_i^j, \tilde{U}_{i+1}^j)) - f(t^j, \hat{e}^j(\tilde{U}_{i-1}^j, \tilde{U}_i^j)) \, dt \right], \quad (3.10)$$

where $\hat{e}(\tilde{U}_i^j, \tilde{U}_{i+1}^j)$ denotes the solution of the Riemann problem at the cell interface $x_{i+1/2}$. Focusing on the advection equation (3.3), and assuming that a positive flow is oriented towards increasing cell indices, the solution of (3.10) reads

$$\tilde{U}_i^{j+1} = \tilde{U}_i^j - \frac{\delta_t}{h} (|v^j| + v^j)(\tilde{U}_i^j - \tilde{U}_{i-1}^j) - \frac{\delta_t}{h} (|v^j| - v^j)(\tilde{U}_i^j - \tilde{U}_{i+1}^j), \quad (3.11)$$

which is the upwind scheme known from the finite difference method applied to the finite volume setting.

ADER schemes

Based on the finite volume Godunov method, higher order hyperbolic schemes are formed, by defining higher order piecewise Ansatz functions \tilde{e}^j , with $\tilde{e}^j(t^j, x) = \psi_i(x)$, $x \in I_i$. The need of higher order Ansatz function arises from Godunov's theorem claiming that every linear, monotone scheme is at maximum order 1 accurate. Specifically, ADER schemes [39] solve the following generalized Riemann problem of order k (GRP $_k$)

$$\partial_t \tilde{e}^j + \partial_x f(t^j, \tilde{e}^j) = 0, \quad t \in [t^j, t^{j+1}], \quad (3.12a)$$

$$\tilde{e}^j(x, t^j) = \begin{cases} \psi_i(x) & : x < x_{i+1/2}, \\ \psi_{i+1}(x) & : x > x_{i+1/2}. \end{cases} \quad (3.12b)$$

The polynomials ψ of degree $k \in \mathbb{N}$ are obtained by a reconstruction procedure based on the current finite volumes \tilde{U}_i^j . Weighted Essentially non oscillatory (WENO) schemes reconstruct the polynomials by the restriction of being conservative. The reconstruction polynomial p_i of cell i is required to recover the volume of $k + 1$ cells,

$$\int_{x_{l-1/2}}^{x_{l+1/2}} p_i(x) \, dx = \tilde{U}_l^j, \quad l \in S_i, \quad (3.13)$$

where S_i is a set and refers to the stencil of $k + 1$ connected finite volume cells, including cell i . Since cell i is covered by $k + 1$ different stencil configurations of length $k + 1$, each of the $k + 1$ reconstruction solutions is weighted to minimize oscillations in the approximated solution. The solution $\hat{e}(p_i, p_{i+1})$ to the GRP $_k$ (3.12) allows to solve the integrals over the boundary fluxes in (3.10) to determine the finite volume approximations \tilde{U}_i^{j+1} for the future time step.

Remark 2. *Assuming that the velocity is constant within a time step is a first order approximation to the solution of the integrals occurring in (3.10). As a consequence, even higher order schemes such as ADER will exhibit a global order of 1 with respect to the PDE solution. Still, a high order scheme yields more accurate approximations than a low order scheme, since the local accuracy within each time step is improved.*

3.1.3 Discontinuous Galerkin methods

The following presentation bases on [40, 41]. Discontinuous Galerkin methods (DG) combine concepts of finite element and finite volume methods by basing on a weak formulation while explicitly treating discontinuous boundary fluxes at cell interfaces. As in the case of finite elements, the PDE is multiplied with test functions ψ from the function space

$$W := \{\psi \in L^1(\Omega) : \psi|_1 \text{ is a polynomial of degree } \leq k\}.$$

After multiplication with the test function ψ , integration in space Ω yields a weak representation of the PDE. Additional integration by parts results in

$$\frac{d}{dt} \int_{x_{i-1/2}}^{x_{i+1/2}} e \psi \, dx - \int_{x_{i-1/2}}^{x_{i+1/2}} f(T, e) \partial_x \psi \, dx + [f(t, e) \psi]_{x_{i-1/2}}^{x_{i+1/2}} = 0, \quad \forall \psi \in W. \quad (3.14)$$

Subsequently, the solution e is expressed by the basis that spans the space of test functions,

$$\tilde{e}(t, x) = \sum_{l=0}^k e_i^l(t) \varphi_l(x), \quad \psi(t, x) = \sum_{l=0}^k \psi_i^l(t) \varphi_l(x), \quad x_{i-1/2} < x < x_{i+1/2}.$$

Inserting the polynomials to (3.14) results in

$$c_{i,l} \frac{de_i^l}{dt} = \frac{1}{h} \int_{x_{i-1/2}}^{x_{i+1/2}} f(t, \tilde{e}) \partial_x \psi \, dx - \frac{1}{h} [f(t, \tilde{e}) \psi]_{x_{i-1/2}}^{x_{i+1/2}}, \quad l \in [0, \dots, k], \quad i \in [1, \dots, n], \quad (3.15)$$

which forms an ODE for the temporal evolution of the coefficients of the polynomial \tilde{e} . The coefficients $c_{i,l} = \int_{I_i} \varphi_i \varphi_l \, dx$ result from evaluation of the integral involving the product of test- and numerical functions in (3.14). The last expression on the right side of (3.15) requires the evaluation of the boundary fluxes and forms a generalized Riemann problem, similar to the approach of Godunov. To solve it, the true flux function f is approximated by a numerical flux function \tilde{f} , allowing for a solution of the Riemann problem. Assuming piece-wise constant test functions of order 0, and assuming the Godunov flux for \tilde{f} , (3.15) reproduces the upwind scheme resulting from the Godunov method. Advantages of DG methods are their simple extension to higher orders, and the high potential to parallelize the update of the local domains to a new time step. A possible drawback results from the formally more restrictive CFL condition when using an explicit Runge-Kutta method for the time integration of the ODE (3.15) [42]. For test polynomials of order k , a Runge-Kutta scheme of order $k+1$ has to be applied. For the advection equation (3.3), the following CFL condition on one pipeline results

$$\frac{\delta_t}{h} |v| \leq \frac{1}{2k+1}.$$

DG methods as well as the upwind method can also be equipped with an implicit time integration. Examples are the implicit Euler method, the (implicit) midpoint rule or implicit Runge-Kutta schemes. Implicit time integration allows for larger time steps by avoiding the restrictive CFL condition. As a drawback hyperbolic features such as shock propagation are resolved improperly. To examine the advantages for the dynamics of heating networks, chapter 5 discusses implicit and explicit time integration methods.

3.1.4 Upwind scheme on heating networks

As described above, a spatial discretization of (2.25a) is performed employing the upwind scheme which yields a total number of n finite volume cells. Each pipeline is

equipped with an equidistant mesh of finite volume cells, cf. fig. 3.1 for an illustration of the index notation used for discretization cells. The number and length of cells

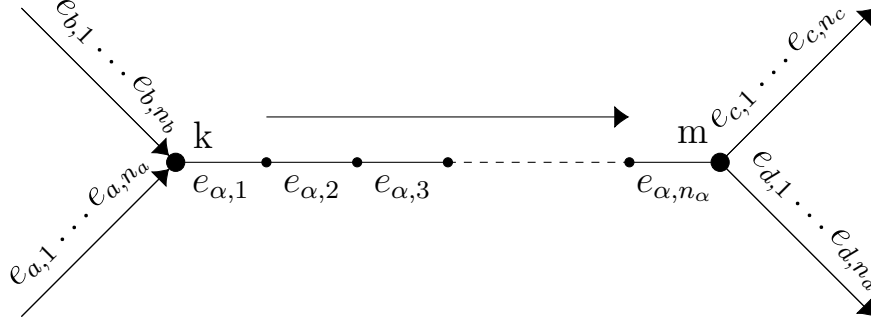


Figure 3.1: Illustration of the upwind discretization in the network case. Cell indices are defined according to the reference orientation defined by the network topology.

varies for different pipelines. The exact strategy to distribute a given number of cells to the set of pipelines is described in chapter 5. Subsequently, $e_{\alpha,\beta}$ refers to finite volume cell β on pipeline $\alpha \in \mathcal{P}$. More specifically, pipeline $\alpha \in \mathcal{P}$ contains the local set of cells $\mathcal{Z}_\alpha := \{1, \dots, n_\alpha\}$ with cardinal number n_α . Cell indices $\beta \in \mathcal{Z}_\alpha$ increase in the direction of positive velocity $v_\alpha \geq 0$, which is parallel to the reference orientation of pipeline α defined by the network topology. The upwind discretization on the network results in two possible types of cell coupling on a network of pipelines and junctions. These are coupling with neighboring cells in the pipeline or with border cells coupling to incoming pipelines at junctions. For pipeline $\alpha = (k, m)$

$$\begin{aligned} \dot{e}_{\alpha,j} &= -\frac{v_\alpha + |v_\alpha|}{2h_\alpha}(e_{\alpha,j} - e_{\alpha,j-1}) - \frac{-v_\alpha + |v_\alpha|}{2h_\alpha}(e_{\alpha,j} - e_{\alpha,j+1}), \quad j \in \mathcal{Z}_\alpha \setminus \{1, n_\alpha\} \\ \dot{e}_{\alpha,1} &= -\frac{v_\alpha + |v_\alpha|}{2h_\alpha}(e_{\alpha,1} - e_k) - \frac{-v_\alpha + |v_\alpha|}{2h_\alpha}(e_{\alpha,1} - e_{\alpha,2}), \\ \dot{e}_{\alpha,n_\alpha} &= -\frac{v_\alpha + |v_\alpha|}{2h_\alpha}(e_{\alpha,n_\alpha} - e_{\alpha,n_\alpha-1}) - \frac{-v_\alpha + |v_\alpha|}{2h_\alpha}(e_{\alpha,n_\alpha} - e_m). \end{aligned} \quad (3.16)$$

Due to changes of flux directions, both signs of the velocity have to be considered in (3.16). The border cells on pipeline α are related to its nodes as follows. Since the upwind scheme is of first order in space, the energy densities at pipeline borders are approximated by the first and last discretization cell on each pipeline,

$$e_\alpha(t, 0) \approx e_{\alpha,1}(t), \quad e_\alpha(t, L_\alpha) \approx e_{\alpha,n_\alpha}(t), \quad \alpha \in \mathcal{P} \quad t \in \mathcal{T}. \quad (3.17)$$

Here, $e_\alpha(t, 0)$, $e_\alpha(t, L_\alpha)$ denote the exact solution of the energy densities at the ends of pipeline α for the PDE (3.3). Hence, the energy density e_k of node $k \in \mathcal{N}$ is defined by

$$e_k = \frac{\sum_{\alpha \in \mathcal{I}_k} \frac{q_\alpha + |q_\alpha|}{2} e_{\alpha,n_\alpha} + \frac{-q_\alpha + |q_\alpha|}{2} e_{\alpha,1}}{\sum_{\alpha \in \mathcal{O}_k} q_\alpha}. \quad (3.18)$$

In particular, (3.18) defines the energy densities at the flow nodes entering consumer stations. While \mathcal{I}_k already considers the effective orientation of pipelines, also the border of the edge has to be defined, which currently couples to node k .

Remark 3. Eqs. (3.16), (3.18) incorporate both possible velocity orientations occurring in the dynamical simulation. This is necessary since the mesh definition is static, while changes of flow direction can occur dynamically in the simulation. For better readability, throughout the rest of this thesis, we will nevertheless assume a positive orientation of all pipelines, and the simplified version of (3.16), (3.18) will be applied.

3.1.5 Basic DAE model resulting from upwind discretization

The system of differential algebraic equations (DAE) analyzed in the remaining part of this chapter is presented subsequently. It results from discretizing the thermal transport in the PDE model discussed in section 2.4 and is defined within the time domain $t \in \mathcal{T}$. The vector of energy densities is restricted to $e \in \tilde{\mathcal{X}}^e$,

$$\tilde{\mathcal{X}}^e := \{e \in \mathbb{R}^n : e_{\min}^\alpha \leq e_{\alpha,\beta} \leq e_{\max}^\alpha, \quad \beta \in \mathcal{Z}_\alpha, \alpha \in \mathcal{P}\}. \quad (3.19)$$

The two main assumptions leading to the DAE model are neglecting thermal losses to the environment and neglecting the acceleration contribution in the momentum balance. The first model component is the thermal part describing the transport of energy using the upwind scheme for times $t \in \mathcal{T}$,

$$\dot{e}_{\alpha,\beta} = -\frac{v_\alpha}{h_\alpha}(e_{\alpha,\beta} - e_{\alpha,\beta-1}), \quad \beta \in \mathcal{Z}_\alpha \setminus \{1\}, \alpha \in \mathcal{P} \quad (3.20a)$$

$$\dot{e}_{\alpha,1} = -\frac{v_\alpha}{h_\alpha}(e_{\alpha,1} - e_k), \quad \alpha = (k, m) \in \mathcal{P}, \quad (3.20b)$$

$$e_k = \frac{\sum_{a \in \mathcal{I}_k} q_a e_a(t, L_a)}{\sum_{a \in \mathcal{O}_k} q_a}, \quad k \in \mathcal{N} \quad (3.20c)$$

$$e_{s:k}(t) = u_F(t), \quad s = (k, m) \in \mathcal{S}, \quad (3.20d)$$

$$e_{c:m}(t) = e_R^c, \quad c = (k, m) \in \mathcal{C}. \quad (3.20e)$$

The second component are the remaining equations defining the advection velocity on every pipeline. As discussed in section 2.2, when neglecting the acceleration in the momentum balance, these read for times $t \in \mathcal{T}$,

$$Kq = 0, \quad (3.21a)$$

$$\Phi_\alpha v_\alpha = q_\alpha, \quad \alpha \in \mathcal{P}, \quad (3.21b)$$

$$G_a - q_a(e_{a:k} - e_{a:m}) = 0, \quad a = (k, m) \in \mathcal{C}, \quad (3.21c)$$

$$-\frac{\lambda(v_\alpha, e_\alpha)}{2d_\alpha} v_\alpha |v_\alpha| - g \partial_x z_\alpha = \frac{1}{\rho_\alpha} \partial_x p_\alpha, \quad \alpha \in \mathcal{P}, x \in [0, L_\alpha], \quad (3.21d)$$

$$p_{s:m} = p_{s:k} + \Delta p_s, \quad s = (k, m) \in \mathcal{S}, \quad (3.21e)$$

$$p_{s:k} = p_R, \quad s = (k, m) \in \mathcal{S}. \quad (3.21f)$$

It is worth noting that the flow defining equations are still non-stationary by the time dependent boundary conditions at consumer stations. Furthermore, all volume flows resulting at consumer stations remain identical comparing (3.21d) with and without the acceleration contribution. Solely the flows representing cycles change when neglecting the acceleration. In typical networks, the number of cycles is small compared to the number of consumer stations. In turn, this assumption allows to focus the subsequent analysis on the dynamics of the thermal transport. Eqs. (3.21) are abbreviated by

$$g(e, q, p, \Gamma) = 0, \quad \Gamma := (G, u_R, p_R, \Delta p_s)^T \quad (3.22)$$

In (3.22), Γ gathers the boundary conditions relevant to define the algebraic equations including the consumption power G , the return energy density u_R , and the pressure levels at the power plant p_R , Δp_s .

3.2 Formulation of a control system

In control theory, a state space representation of a linear dynamical system [22] with a generic state space $\mathcal{X} \in \mathbb{R}^n$ is expressed as

$$E\dot{x} = Ax + Bu, \quad (3.23a)$$

$$y = Cx + Du, \quad (3.23b)$$

where x is the state vector, $u \in \mathbb{R}^{|u|}$ the input driving the system externally, and $y \in \mathbb{R}^{|y|}$ is a subset of the state space which should be observed, the system output. The essential properties of system (3.23) can be deduced from the structure of the operators $A, E \in \mathbb{R}^{n \times n}$, $B \in \mathbb{R}^{n \times |u|}$, $C \in \mathbb{R}^{|y| \times n}$, $D \in \mathbb{R}^{|y| \times |u|}$. In addition, many results and tools from model order reduction are available for this class of systems. In this spirit, a system description close to (3.23) is derived subsequently for the dynamics of district heating networks.

3.2.1 Linear time varying system

For a fixed volume flow field \bar{q} , the system matrix $A(\bar{q}) \in \mathbb{R}^{n \times n}$ is defined as the Jacobian of the ODE system (3.20),

$$A_{f_Z(i,j), f_Z(k,l)}(\bar{q}) := \frac{\partial \dot{e}_{i,j}}{\partial e_{k,l}}(\bar{q}), \quad (3.24)$$

where e is the vector of finite volume cells on the entire network. Rows and columns of the matrix A are mapped to the edge- and cell indices i, j by the ordering function

$$f_Z(e, c) := c + \sum_{k=1}^{e-1} n_k, \quad e \in \mathcal{P}, \quad c \in \mathcal{Z}_e. \quad (3.25)$$

Both the upwind scheme and the conservation of energy are encoded in the volume flow dependent matrix $A(\bar{q})$. Its entries are functions depending on the volume flow, relating the time derivative of each finite volume cell to the vector e . The population structure of $A(\bar{q})$ even changes qualitatively if a pipeline undergoes a change of flux direction. The input matrices B_F, B_R address the finite volume cells which are related to the input energy densities u_F, u_R of flow and return network and are defined by

$$B_F(\bar{q}) := \frac{\partial \dot{e}}{\partial u_F}(\bar{q}), \quad (3.26a)$$

$$B_R(\bar{q}) := \frac{\partial \dot{e}}{\partial u_R}(\bar{q}). \quad (3.26b)$$

For the flow network, u_F is the energy density supplied by the power plant. For the return network, u_R represents the contractually defined energy densities returning from heat exchangers at consumer stations. The set of observables depends on the specific application. Within this thesis, the energy densities in the flow network entering the consumer stations are measured by C_F and the energy density entering the power plant in the return network by C_R , cf. fig. 3.2. For existing heating networks, only one pipeline enters a given heat exchanger, requiring to only observe a single energy density for each consumer. To describe both flow and return network, the operators

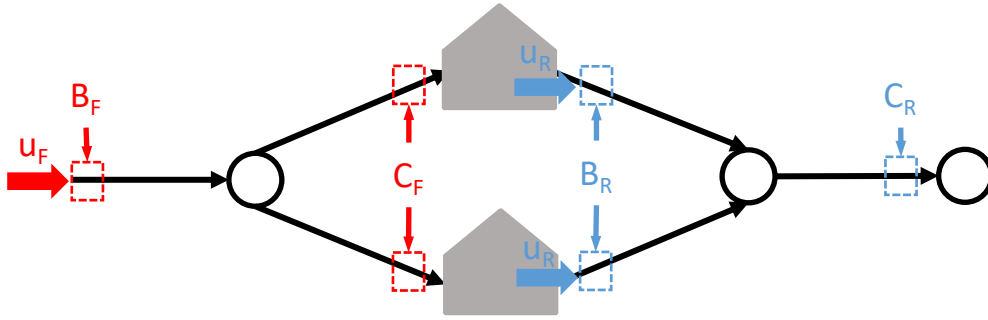


Figure 3.2: Illustration of input energy densities and input- and output operators for flow (red) and return (blue) network. Dashed rectangles indicate finite volume cells.

A, B, C can be decomposed into block structure, where the blocks represent the flow " F " and the return " R " network,

$$A = \begin{pmatrix} A_F & \\ & A_R \end{pmatrix}, \quad B = \begin{pmatrix} B_F & \\ & B_R \end{pmatrix}, \quad C = \begin{pmatrix} C_F & \\ & C_R \end{pmatrix}.$$

Specifically, since both subnetworks are thermally decoupled, the operators are block diagonal. While both are identical in terms of the temperature transport, the main difference results from the fact that the boundary condition at the consumers defining the volume flow field solely couples to the state space of the flow network. If not

stated explicitly, the properties of A, B, C discussed subsequently apply to both the spatially discretized flow and return network. This allows to formulate the entire system of differential algebraic equations as the following parameterized linear time varying control system

$$\dot{e} = A(q)e + B(q)u_T, \quad (3.27a)$$

$$y = Ce, \quad (3.27b)$$

$$0 = g(e, q, p, \Gamma). \quad (3.27c)$$

In this notion, (3.27) mirrors the advection of the energy density subject to the thermal input $u_T = (u_F, u_R)^T$, with $B(v) \in \mathbb{R}^{n \times |u|}$. Outputs y are a linear combination of energy densities and are observed by $C \in \mathbb{R}^{|y| \times n}$. The flow defining equations (3.27c) act as generators for the volume flow field q . Eq. (3.27) is expressed in the basic state variables e, q, p . The resulting operator $A(q)$ is equivalent to (3.24) by $q_\alpha = \Phi_\alpha v_\alpha$, $\alpha \in \mathcal{P}$. Although volume conservation is assumed by default, $A(q)$ could equivalently be defined for conservation of mass. Note that C does not depend on the flow field and thus is a constant in time linear operator. Eq. (3.27) does also have an interpretation as a descriptor system [43]

$$\begin{aligned} E\dot{x} &= F(x, u_T) \\ y &= C_e x, \end{aligned}$$

where $E \in \mathbb{R}^{n \times n}$ is a singular matrix, and $x = (e, q, p)$ collects the state variables energy density, volume flow and pressure. For district heating networks, E constitutes a diagonal matrix with entries 1 for rows referring to energy densities and zero for rows referring to algebraic equations. Since the reduction of algebraic equations and variables might introduce instabilities, we focus on the reduction of the purely differential part given by the transport of the energy density.

3.3 Affine decomposition of system and input operator

Within this section, an affine decomposition of the system operators A, B of the DAE (3.27) is discussed. An affine decomposition to time-constant matrices and a volume flow dependent part is useful, since it allows for a determination of projection based reduced system operators in the offline-phase. The determination of reduced operators is discussed in chapter 4. A general form of an affine decomposition of a finite dimensional operator $\Theta : \mathbb{R}^P \mapsto \mathbb{R}^{n \times n}$ in terms of a parameter vector $p \in \mathbb{R}^P$, $P \in \mathbb{N}$ and time constant matrices Θ_i is given by [44]

$$\Theta(p) = \sum_{i=1}^P \gamma_i(p) \Theta_i, \quad (3.28)$$

where $\gamma : \mathbb{R}^P \mapsto \mathbb{R}^P$ is a function of the parameter vector p and $\Theta_i \in \mathbb{R}^{n \times n}$ are constant matrices. The possibility to express the operators $A(v), B(v)$ in the structure of (3.28)

has two origins. First, the Euler-like equations result in a quasi-linear hyperbolic system in the energy density. Second, the conservation of energy at every network node defines the outgoing energy density to be a linear combination of the entering energy densities with the volume flow vector as coefficients. To illustrate this observation, the ODEs describing the energy densities on pipeline α are considered. The inner energy densities $e_{\alpha,\beta}$, $\beta \in [2, \dots, n_\alpha]$ are trivial and can be expressed as products of q_α and $e_{\alpha,\beta}$, $\beta \in [1, \dots, n_\alpha - 1]$. The ODE for the first energy density is more involved and reads

$$\dot{e}_{\alpha,1} = -\frac{v_\alpha}{h_\alpha}(e_{\alpha,1} - e_k) = -\frac{q_\alpha}{\Phi_\alpha h_\alpha}e_{\alpha,1} + \frac{q_\alpha}{\Phi_\alpha h_\alpha} \frac{\sum_{b \in \mathcal{I}_k} q_b e_{b,n_b}}{\sum_{b \in \mathcal{O}_k} q_b}, \quad \alpha = (k, m) \in \mathcal{P}. \quad (3.29)$$

Since this applies for every pipeline $\alpha \in \mathcal{P}$, $A(q)$ can be decomposed in the form (3.28), The corresponding weighting coefficients are linear, $\gamma(q) \propto q_\alpha$, for ODEs relating inner energy densities on pipeline α and are nonlinear for the first cell on pipeline α . Precisely, $A(q)$ can be expressed as (3.29) with volume flow dependent weighting functions. Hereafter, useful choices for parameter and weighting function γ are discussed, exploiting the specific topology of heating networks by assuming conservation of volume over network nodes.

Parameterization of networks without changes of flux direction

The splitting of flow-defining and thermal equations suggests to perform an affine decomposition of the system operators. Focusing on a single pipeline $\alpha \in \mathcal{P}$, the ODE resulting from an upwind discretization is defined in (3.16). Due to the available pipeline junctions, nodes in existing district heating networks couple to at maximum three pipelines. For this structure of the nodes, combining conservation of energy and volume simplifies the ODE for the first cell on pipeline α to two cases,

$$\dot{e}_{\alpha,1} = \begin{cases} -\frac{v_\alpha}{h_\alpha}e_{\alpha,1} + \frac{1}{h_\alpha \Phi_\alpha}(q_k e_{k,n_k} + q_l e_{l,n_l}), & : k, l \in \mathcal{I}_k \\ -\frac{v_\alpha}{h_\alpha}e_{\alpha,1} + \frac{v_\alpha}{h_\alpha}e_{k,n_k} & : \text{only } k \in \mathcal{I}_k. \end{cases} \quad (3.30)$$

In the first case, two pipes flow into node k . The node contributes the flux

$$-\frac{v_\alpha}{h_\alpha}e_k = -\frac{v_\alpha}{h_\alpha} \frac{(q_k e_{k,n_k} + q_l e_{l,n_l})}{q_\alpha} = -\frac{1}{h_\alpha \Phi_\alpha}(q_k e_{k,n_k} + q_l e_{l,n_l}). \quad (3.31)$$

In the second case only one pipeline flows into node k . In both cases, the ODE for the first cell in pipeline α is a bilinear expression in velocities and energy densities. Thus, if the orientation of all pipelines remains static, a possible affine decomposition of the system and input operators is given by

$$\hat{A}(v) = \sum_{\nu=1}^{|\mathcal{P}|} v_\nu A_\nu^v, \quad \hat{B}(v) = \sum_{\nu=1}^{|\mathcal{P}|} v_\nu B_\nu^v,$$

where $|\mathcal{P}|$ denotes the number of pipelines. The matrices $A_\nu^v \in \mathbb{R}^{n \times n}$, $B_\nu^v \in \mathbb{R}^{n \times |u|}$ are time-independent operators multiplied with the time-varying components of the velocity vector. The notation A_ν^v indicates that the time-independent matrices are created using the velocity as a parameter, but do not depend on the dynamically changing velocity vector. The system operators $\hat{A}(v), \hat{B}(v)$ equal the desired system operators $A(q), B(q)$ introduced in the previous sections. The central difference is the parameter basis use in their construction. It turns out that using independent volume flows as parameters is more efficient for the construction of reduced order operators discussed in chapter 4. Thus, throughout the rest of this thesis $A(q), B(q)$ refer to constructing the system operators by independent volume flows. By conservation of volume and incompressibility, these are related to the velocities as

$$v = S\tilde{q},$$

where S is the solution operator of the linear volume conservation law. The system operators can then be written as

$$A(q) = \sum_{\nu=1}^{|\mathcal{L}_G|+|\mathcal{C}|} \tilde{q}_\nu A_\nu^{\tilde{q}}, \quad B(q) = \sum_{\nu=1}^{|\mathcal{L}_G|+|\mathcal{C}|} \tilde{q}_\nu B_\nu^{\tilde{q}},$$

where the notation $A(q), B(q)$ is chosen to express that independent volume flows \tilde{q} are used as parameters. Using independent volume flows to describe the system operators, the number of parameters reduces. By conservation of volume for arbitrary networks it holds that

$$|\mathcal{L}_G| + |\mathcal{C}| \leq |\mathcal{P}|.$$

At the same time, the time-independent system operators $A_\nu^{\tilde{q}}$ couple to more finite volume cells in the network compared to using velocities as parameters, since by conservation of volume, an independent flow couples to potentially multiple pipelines, cf. fig. 3.3. Reducing the number of parameters is important for a later use in projection based model order reduction, cf. chapter 4. Instead of using the conservation of volume at network nodes, the conservation of mass could be claimed. As a drawback, the inflowing energy density on pipeline α would not represent a convex combination of incoming energy densities anymore, cf. (3.29) and the representation (3.31) would not be possible anymore. In addition, the concept of independent volume flows \tilde{q} does not exist and volume flows potentially differ on each pipeline. Hence, the number of parameters required by an affine decomposition increases.

If the flow direction of all considered pipelines is not static, but potentially changes for the boundary conditions of interest, additional nonlinear parameters have to be introduced for an affine decomposition.

Parameterization of changes of flux directions

By conservation of volume, a pipeline changes its flux direction as part of a segment of pipelines. Such a group of pipelines changing flow directions simultaneously will

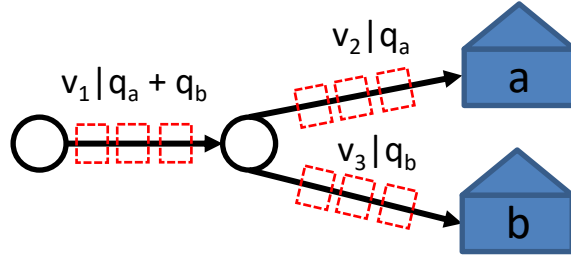


Figure 3.3: Illustration of independent volume flows q_a , q_b and the velocities v_i , $i \in [1, 2, 3]$ for an example network.

be called "segment", cf. fig. 3.4. The border nodes at the start and the end of the segment have to couple to at least three edges. As mentioned above, existing heating networks couple to at maximum three edges at a every node. Under this assumption, a setup in which a pipeline changes its flux direction is visualized in fig. 3.4. For the

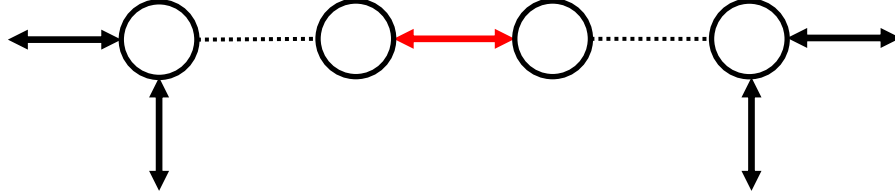


Figure 3.4: Illustration of a segment containing a pipeline undergoing a change of flux direction (red). It is constrained by border nodes at the left and right side which couple to three edges each, all of which might undergo a change of flux direction itself.

presented segment, it is possible to describe the change of flux direction by a single representative pipeline marked in red. The ODE of finite volume cells on a pipeline α within this segment can consequently be parameterized by its volume flow q_r at the reference edge r ,

$$\dot{e}_{\alpha,1} = -\frac{q_r + |q_r|}{2h_\alpha \Phi_i}(e_{\alpha,1} - e^L) + \frac{q_r - |q_r|}{2h_\alpha \Phi_i}(e_{\alpha,1} - e_{\alpha,2}), \quad (3.32a)$$

$$\dot{e}_{\alpha,n_\alpha} = -\frac{q_r + |q_r|}{2h_\alpha \Phi_\alpha}(e_{\alpha,n_\alpha} - e_{\alpha,n_\alpha-1}) + \frac{q_r - |q_r|}{2h_\alpha \Phi_\alpha}(e_{\alpha,n_\alpha} - e^R), \quad (3.32b)$$

$$\dot{e}_{\alpha,\beta} = -\frac{q_r + |q_r|}{2h_\alpha \Phi_i}(e_{\alpha,\beta} - e_{\alpha,\beta-1}) + \frac{q_r - |q_r|}{2h_\alpha \Phi_\alpha}(e_{\alpha,\beta} - e_{\alpha,\beta+1}), \quad j \in [2, \dots, n_\alpha - 1]. \quad (3.32c)$$

Here, $e^L(e^R)$ denotes the energy density at the left(right) border nodes of pipeline α . For all pipelines within the domain coupling to simple nodes, $e^L(e^R)$ are proportional to the first or last finite volume cell of the neighboring pipeline in the segment. In contrast, the influence of the edges at left and right border nodes to the first and last cell in the flux changing domain is more involved and depends on the current flux orientation of the reference edge r towards the edges at the border nodes. The three possible configurations at a border node are presented in fig. 3.5. The aim is to construct a single nonlinear parameter describing how energy is transported to a

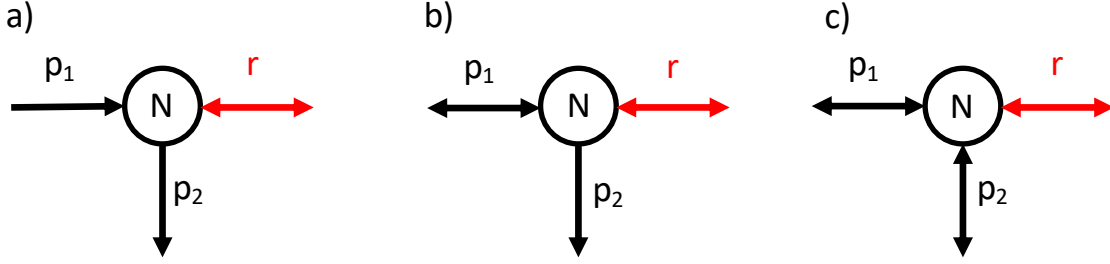


Figure 3.5: Illustration of the possible flux configurations at the left border node coupling to three edges. The changing reference edge r either couples to two pipelines which either remain at a constant orientation (a), or one of them changes orientation (b) or finally all of them change their orientation (c).

pipeline leaving the junction displayed in fig. 3.5, based on the flow configuration of the other two pipelines. A function fulfilling this task is given by

$$f_p(i, j, k) := s_k^- s_i^+ |q_i| \frac{|q_i| + l_j q_j}{|q_i| + s_j^+ l_j q_j}. \quad (3.33)$$

In (3.33) l_j stores the sign of q_j when entering node k . Similarly, $s_i^+(s_i^-)$ equals one if the current volume flow q_i enters(exits) node k , and is zero else. For three edges coupling to node k , (3.33) defines the energy flow of a reference pipeline i to pipeline k , based on the current orientation of the third pipeline j . It represents a generic solution of the conservation of energy and volume for all possible orientations of the coupling edges. For an upwind discretization this allows to write

$$\dot{e}_{k,1} = -\frac{v_k}{h_k} e_{k,1} + \frac{1}{h_k \Phi_k} (f_p(i, j, k) e_{i,n_i} + f_p(j, i, k) e_{j,n_j}). \quad (3.34)$$

More precisely, (3.33) contributes a volume flow only if pipeline k indeed exits node k and pipeline i enters k . If pipeline j enters k ($s_j^+ = 1$), i transports e_{i,n_i} with volume flow $|q_i|$ to pipeline k . If j exits node k , i transports e_{i,n_i} with a volume flow $|q_i| + l_j q_j$ to pipeline k .

The representation (3.33) allows to systematically define how energy is transported by edges possibly changing their flux direction. The parameterization is performed in steps. First, segments which contain a change of flux directions have to be defined a priori. This can be done using training simulations for given boundary conditions. Second, the parameterization is done for all pipelines which are not affected by pipelines changing the flux direction. Third, all segments undergoing a change of flux direction are considered. For both velocity profiles of the segment, the transport of energy from the segment to pipelines leaving the outflow boundary of the segment is written. The scheme to describe the transport of pipelines reverting their orientation is summarized in alg. 1. The resulting parameterization including changes of flux directions based on independent volume flows reads

$$A(q) = \sum_{\nu=1}^{n_q} \gamma_{\nu}^{\tilde{q}}(q) A_{\nu}^{\tilde{q}}, \quad B(q) = \sum_{\nu=1}^{n_q} \gamma_{\nu}^{\tilde{q}}(q) B_{\nu}^q, \quad (3.35)$$

Algorithm 1 Parameterization of energy transport for edges exhibiting changes of flux directions

- 1: Determine the parameterization for all pipelines, which are not affected by a pipeline changing its flux direction.
- 2: **for** all segments containing a change of flux direction **do**
- 3: Define a representative edge r in the segment s .
- 4: Write the temporal derivative of the energy density for all pipelines i in the segment s according to (3.32) as defined in the following steps.
- 5: **for** positive and negative configurations of the reference flow q_r **do**
- 6: Determine the outflow boundary node n_o of segment s .
- 7: Determine the finite volume cells within the segment at the inflow and outflow boundary: $(b_{\text{in}}, c_{\text{in}})$, and $(b_{\text{out}}, c_{\text{out}})$.
- 8: Write the influence of the reference pipeline r to all edges exiting node n_o . To this end, distinguish the following cases.
- 9: 1. Pipelines p_1, p_2 have fixed flow direction within the simulation, p_1 runs in the node, p_2 runs out.

$$\begin{aligned}\dot{e}_{p_2,1} &\propto -q_{p_1}e_{p_2,1} + f_p(r, p_1, p_2)e_{r,1} + f_p(p_1, r, p_2)e_{p_1, n_{p_1}} \\ \dot{e}_{p_2,j} &\propto -q_{p_2}(e_{p_2,j} - e_{p_2,j-1}), \quad j \in [2, \dots, n_j] \\ \dot{e}_{b_{\text{out}}, c_{\text{out}}} &\propto -q_r e_{b_{\text{out}}, c_{\text{out}}} + f_p(p_1, p_2, r)e_{p_1,1}\end{aligned}$$

2. Pipeline p_1 changes direction within the simulation, p_2 is fixed, and runs in.

$$\dot{e}_{p_1,1} \propto -q_{p_1}e_{p_1,1} + f_p(r, p_2, p_1)e_{b_{\text{out}}, c_{\text{out}}} + \propto f_p(p_2, r, p_1)e_{p_2, n_{p_2}}$$

3. Pipeline p_1 changes its direction, the fixed edge p_2 runs out.

$$\begin{aligned}\dot{e}_{p_2,1} &\propto -q_{p_2}e_{p_2,1} + f_p(r, p_1, p_2)e_{b_{\text{out}}, c_{\text{out}}} + f_p(p_1, r, p_2)e_{p_1, n_{p_1}} \\ \dot{e}_{p_2,j} &\propto -q_{p_2}(e_{p_2,j} - e_{p_2,j-1}), \quad j \in [2, \dots, n_j] \\ \dot{e}_{p_1,1} &\propto -q_{p_1}e_{p_1,1} + f_p(r, p_1, p_2)e_{b_{\text{out}}, c_{\text{out}}}\end{aligned}$$

4. All three edges change their sign within the simulation.

$$\begin{aligned}\dot{e}_{p_1,1} &\propto -q_{p_1}e_{p_1,1} + f_p(r, p_2, p_1)e_{b_{\text{out}}, c_{\text{out}}} \\ \dot{e}_{p_2,1} &\propto -q_{p_2}e_{p_2,1} + f_p(r, p_1, p_2)e_{b_{\text{out}}, c_{\text{out}}}\end{aligned}$$

10: **end for**

11: **end for**

where $B_\nu^{\tilde{q}}, A_\nu^{\tilde{q}}$ are time-independent matrices multiplied with volume flow dependent weighting functions $\gamma : \mathbb{R}^{n_q} \mapsto \mathbb{R}^{n_q}$. Thus, γ changes over time with the boundary condition defining the volume flows at houses. Here, n_q denotes the number of parameters required to describe the energy transport. The latter amounts to the number of independent volume flows $|\mathcal{L}_G| + |\mathcal{C}|$ plus four to six nonlinear parameters for each segment changing the flux direction. The number of parameters depends on the cases illustrated in fig. 3.5. The presented scheme can be extended to cases with more than three pipelines coupling at a given node. This would form a more complex nonlinear function (3.33) incorporating the increased number of edges coupling to the considered node. Using a nonlinear parameter to model the influence of a pipeline changing its flow direction reduces the number of parameters needed in the affine composition compared to the usage of linear representations. This is crucial when applying Galerkin projections, in which even sparse unreduced matrices become densely populated. Furthermore, expressing the DAE based on matrices allows to easily compute gradients with respect to state variables.

3.4 Existence and uniqueness of solutions

Subsequently existence and uniqueness of the solution of the spatially discretized system (3.27) shall be analyzed resulting from spatial discretization with the upwind scheme. The essential assumptions considered in (3.27) are volume conservation, a loss-less energy transport, and the assumption that acceleration is neglected in the momentum balance. Within this section, system (3.27) is abbreviated by

$$\dot{e} = f(t, e), \quad e \in \tilde{\mathcal{X}}^e, \quad e_0 = e(t_0). \quad (3.36)$$

The considered spatial domain $\tilde{\mathcal{X}}^e$ is defined in (3.19). Finite volume cells entering consumer stations in the flow network are strictly larger than the corresponding return energy densities of heat exchangers. In addition, the boundary functions u_T, G are assumed to be continuous in time. In the following the Picard-Lindelöf theorem [45] is applied to (3.36) consisting of the discretized advection term subject to the hydrodynamic equations serving as algebraic constraints. The resulting DAE exhibits differentiation index 1, cf. section 3.5.

Theorem 4. *We assume that the input energy densities u_T and the power consumption G are continuous functions of time and are bounded. In addition the considered network topology does not contain cycles in the flow- or the return network. Then, for the solenoidal descriptor system (3.27) resulting from upwind discretization with quasi-stationary hydrodynamic equations, there exists a unique solution of (3.27).*

Proof of Theorem 4. Using the Picard-Lindelöf theorem [45], it suffices to show that $f(t, e)$ is continuous with respect to time t and Lipschitz continuous with respect to the energy density e . If the network is free of cycles, a representation of the ODE (3.27) is given by

$$\dot{e} = \sum_{i \in \mathcal{C}} q_i(G_i(t), e)[A_i e + B_i u_T(t)], \quad (3.37)$$

where $A_i, B_i, i \in \mathcal{C}$ are time-independent matrices. Inserting the solution of the volume flows at consumer stations resulting from (2.13) yields

$$\dot{e} = \sum_{i \in \mathcal{C}} \frac{G_i(t)}{e_i - e_R^i} [A_i e + B_i u_T(t)]. \quad (3.38)$$

Eq. (3.38) contains products and sums of the functions u_T, G which are continuous in time, yielding continuity in time for the entire DAE. Showing Lipschitz continuity with respect to the energy density results in

$$\|f(t, x) - f(t, y)\| \leq c\|x - y\|, \forall x, y \in \tilde{\mathcal{X}}^e, \quad c \in \mathbb{R}^+, \quad c \neq 0.$$

Due to equivalence of norms on finite dimensional spaces, the used norm is not specified further. Inserting (3.38) gives

$$\|f(t, x) - f(t, y)\| = \left\| \sum_{i \in \mathcal{C}} q_i^x [A_i x + B_i u_T(t)] - q_i^y [A_i y + B_i u_T(t)] \right\|, \quad (3.39)$$

$$= \left\| \sum_{i \in \mathcal{C}} A_i [q_i^x x - q_i^y y] + B_i u_T(t) [q_i^x - q_i^y] \right\|, \quad (3.40)$$

where $q_i^x := q_i(G_i(t), x)$ denotes the volume flow resulting from the energy density x . If the functions

$$x \in \tilde{\mathcal{X}}^e \mapsto q_i^x, \quad i \in \mathcal{C}, \quad (3.41a)$$

$$x \in \tilde{\mathcal{X}}^e \mapsto q_i^x x, \quad i \in \mathcal{C}, \quad (3.41b)$$

are Lipschitz continuous with respect to energy densities, inserting their Lipschitz constants $c_i^{q,x}, c_i^q$ yields

$$\begin{aligned} \|f(t, x) - f(t, y)\| &\leq \left\| \sum_{i \in \mathcal{C}} A_i c_i^{q,x} \|x - y\| + B_i u_T(t) c_i^q \|x - y\| \right\| \\ &\leq \left(\sum_{i \in \mathcal{C}} \|A_i\| |c_i^{q,x}| + |u_T(t)| \sum_{i \in \mathcal{C}} \|B_i\| |c_i^q| \right) \|x - y\|. \end{aligned}$$

Note that the norm of finite dimensional matrices is finite. Hence it suffices to show that the functions (3.41) are Lipschitz continuous. Since $e \in \tilde{\mathcal{X}}^e$, the following derivative exists and is bounded

$$\left| \frac{d}{dx} \frac{G_i}{x - e_R^i} \right| = \left| \frac{G_i}{(x - e_R^i)^2} \right| \leq \frac{\max_{j \in \mathcal{C}, t \in \mathcal{T}} G_j(t)}{\min_{j \in \mathcal{C}} (e_{\min}^F - e_R^j)}, \quad i \in \mathcal{C}, \quad x \in \tilde{\mathcal{X}}^e,$$

where the fact is used that the admissible energy densities are larger than each energy density in the return part of consumer stations, $e_{\min}^F > \max_{a \in \mathcal{C}} e_R^a$. This allows to conclude that

$$|q_i^x - q_i^y| \leq c_i^q |x - y| \leq c_i^q \|x - y\|, \quad \forall x, y \in \tilde{\mathcal{X}}^e, i \in \mathcal{C}.$$

Lipschitz continuity of the product of energy density and volume flow follows by

$$\begin{aligned}
 \|q_i^x x - q_i^y y\| &= \|q_i^x x - q_i^y y + q_i^x y - q_i^x y\| \\
 &= \|q_i^x (x - y) + y(q_i^x - q_i^y)\| \\
 &\leq \|q_i^x\| \|x - y\| + \|y\| \|q_i^x - q_i^y\| \\
 &\leq \|q_i^x\| \|x - y\| + c_i^q \|y\| \|x - y\| \\
 &\leq c_i^{q,x} \|x - y\|,
 \end{aligned}$$

and the fact that $x, y \in \tilde{\mathcal{X}}^e$, and thus both q_i^x, y are bounded. The energy densities x, y are bounded since the maximal admissible energy densities in $\tilde{\mathcal{X}}^e$ are bounded. As a last step to showing existence and uniqueness, one has to prove that a solution with admissible initial conditions $e_0 \in \tilde{\mathcal{X}}^e$ is ensured to remain within $\tilde{\mathcal{X}}^e$, given that each component of the thermal control $(u_T)_i$, $i = 1, \dots, |u|$ takes values within $[e_{\min}^{\text{net}}, e_{\max}^{\text{net}}]$.

To this end, we consider the simulation interval $\mathcal{T} = [t_0, t_{\text{end}}]$. Both the components of the initial state e_0 and the components of the control u_T are assumed to take values within $(e_{\min}^{\text{net}}, e_{\max}^{\text{net}})$ and thus, are strictly larger than e_{\min}^{net} . We choose a proof by contradiction and assume that there exists a time $\tau \in \mathcal{T}$ at which at least one cell β_r , for the first time within \mathcal{T} , equals the critical value $e_{\beta_r}(\tau) = e_{\min}^{\text{net}}$. Then, we know that for times $t < \tau$ the solution of the energy density is continuously differentiable by the results obtained so far. Different cases are considered subsequently for the cells $e_{\beta_{r\leftarrow}}$ influencing β_r . In case 1, the energy density of the reference cell is smaller than the energy density of one of its preceding cells, $e_{\beta_r}(\tau) < e_{\beta_{r\leftarrow}}(\tau)$. By definition of the upwind scheme cf. (3.16), it follows that $\dot{e}_{\beta_r}(\tau) > 0$. This in turn requires that $e_{\beta_r}(t) \leq e_{\min}^{\text{net}}$ for a small time interval $\tau - \epsilon < t < \tau$ with $\epsilon > 0$, which is a contradiction to the assumption that τ is the first time at which $e_{\beta_r}(\tau) = e_{\min}^{\text{net}}$. In case 2, all cells influencing the reference cell take energy densities identical to the reference cell, $e_{\beta_{r\leftarrow}}(\tau) = e_{\beta_r}(\tau)$. In this case, preceding cells are searched until a cell c is found which has a preceding cell with larger value, $e_{c\leftarrow} > e_{\min}^{\text{net}}$. Subsequently, the argument of case 1 again applies to e_c . If all cells exhibit an identical value e_{\min}^{net} , at least the cells ζ closest to the injection points of thermal energy in flow- and return network will possess a positive temporal derivative

$$\dot{e}_i(\tau) = -|v|(e_i(\tau) - u_T^i(\tau)) > 0, \quad i \in \zeta. \quad (3.42)$$

In (3.42) u_T^i is the input which directly affects cell i , and cell i is an element of the set of cells ζ which are exclusively influenced by the thermal controls. Hence, a positive slope results and by the argument of case 1 a contradiction to the existence of the time $\tau \in \mathcal{T}$ is given. Consequently, if the components of the initial state and the control are ensured to be larger than e_{\min}^{net} , the resulting energy densities will be larger than e_{\min}^{net} , as well. The same chain of arguments applies for the upper bound e_{\max}^{net} closing the proof. \square

Existence of solutions for topologies including cycles

In [46, 47] existence and uniqueness of solutions is shown for equations governing water networks including cycle structures. These are described by a set of equations closely related to the flow defining equations (2.26) within time $t \in \mathcal{T}$

$$Kq = 0, \quad (3.43a)$$

$$q_a = q_a(t), \quad a = (k, m) \in \mathcal{C}, \quad (3.43b)$$

$$-\rho \frac{L_\alpha \lambda_\alpha}{2d_\alpha} v_\alpha |v_\alpha| - \rho g \Delta z_\alpha - \rho L_\alpha \dot{v}_\alpha = \Delta p_\alpha, \quad \alpha \in \mathcal{P}, \quad (3.43c)$$

$$p_{s:m} = p_{s:k} + \Delta p_s, \quad s = (k, m), \quad (3.43d)$$

$$p_{s:k} = p_R, \quad s = (k, m). \quad (3.43e)$$

Specifically, the density is globally constant, and the friction factor is a temporally constant pipeline-specific parameter. The volume flow at the network ends is defined by demand functions q_a , $a \in \mathcal{C}$. In [46], global unique solvability is shown for (3.43) without the acceleration contribution \dot{v}_α . Thus, it remains to show that the unique solution of (3.43) is Lipschitz continuous in the volume flows defined at consumer stations. This proof would allow to conclude for the existence of solutions of (3.36) for networks including cycles which do not exhibit a change of flow direction. However, this proof is an open task for future research and not further analyzed within this thesis.

Contact discontinuities by changes of flux direction

In theorem 4, networks exhibiting changes of flux direction are excluded. This is due to the fact that changes in flux direction can induce contact discontinuities in the PDE description of the energy transport. A minimum example for a network containing a pipeline which changes its flux direction is presented in fig. 3.6. Assuming that pipelines (1,2) and (1,3) share identical length and diameter, the sign of the volume flow along edge 2,3 changes with the difference of the volume flows at houses a, b , $q_3 \propto q_a - q_b$. To illustrate the creation of a contact discontinuity the following scenario is considered. The velocity v_3 of pipeline 3 is directed towards node 3 and positive. After a finite time, its flux direction reverts to a negative sign. With $\tau \in \mathbb{R}^+$, the time is denoted at which $v_3(\tau) = 0$, such that $v_3(\tau + \epsilon) < 0$, $\forall \epsilon$, $0 < \epsilon \leq \delta$ for a small time interval $\delta > 0$. Hence, the time evolution of the energy density e_{3,n_3} in the cell close to node 3 is defined by

$$e_{3,n_3} := \begin{cases} e_2(t - s(t)) & : t \leq \tau, \\ e_3(t) & : t > \tau. \end{cases} \quad (3.44)$$

In (3.44), e_2 denotes the energy density of node 2, and $s(t)$ is the temporally changing transport time between node 2 and cell e_{3,n_3} for positive velocities v_3 . Similarly, e_3 denotes the energy density of node 3. Eq. (3.44) defines a Riemann problem, if

$e_3(\tau) \neq e_2(\tau - s(\tau))$, inducing a contact discontinuity which propagates along pipeline 3 subsequently. Since the volume flow q_3 changes continuously while attaining the value 0, the transported power qe does also change continuously. In contrast, the energy density exhibits a contact discontinuity. Focusing on the PDE level, this contact discontinuity would propagate to at least one heat exchanger, inducing a discontinuity in the volume flow at consumer stations. This discontinuity leads to oscillations in the network dynamics. This is in contrast to the ODE level studied here, in which due to the numerical diffusion introduced by the upwind discretization, the initial contact discontinuity will be smoothed to a continuous signal in the energy density. While this is not a formal proof, even in the case of flux changes, a classical, unique solution to (3.36) is expected. By increasing the number of finite volume cells, the resulting solution will be a continuous approximation to the contact discontinuity propagation occurring in the PDE case.

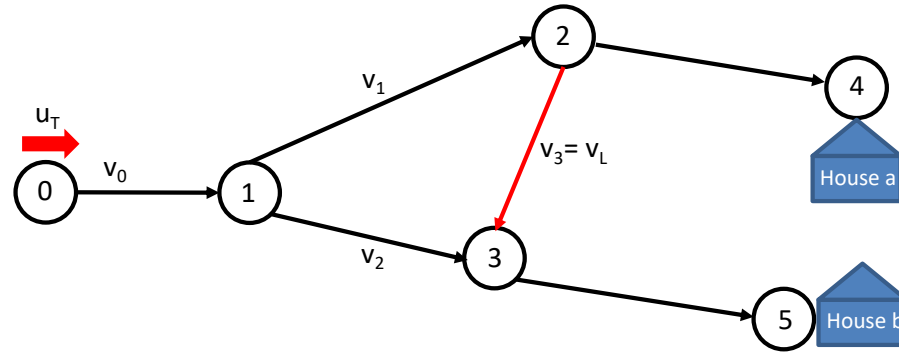


Figure 3.6: Minimum example for a flow network in which a change of flux direction is possible (edge 2-3) for appropriate volume flows at consumer stations.

3.5 Differentiation index of the DAE

The differentiation index of the DAE (3.27), cf. section 3.1.5, shall be evaluated subsequently. It is defined as the number of differentiations needed to transform the DAE to a pure ODE in all state variables [48], [43]. For heating networks, these refer to the vector of velocities, energy densities and pressures. To apply this definition, networks are considered, for which a unique solution of (3.27) is ensured as discussed in section 3.4. We consider the DAE (3.27) defined in section 3.1.5 with and without the acceleration contribution in what follows. It turns out that by including the acceleration in (3.21d), the differentiation index of the DAE equals 2. In addition, neglecting the contribution of acceleration in (3.21d) as done to derive (3.27) in section 3.1.5 reduces the index to 1. Alternatively, removing the pressure from the considered state variables and removing the momentum balance (3.21d) from the set of equations, as described in section 2.2, reduces the index to 1, as well.

When attempting to write the basic DAE model defined in section 3.1.5 as a purely differential system, one notes that the advection equation already is in the form of a differential equation for the energy densities,

$$\dot{e}_{\alpha,1} = -\frac{v_\alpha}{h_\alpha}(e_{\alpha,1} - e_k), \quad \alpha = (k, m) \in \mathcal{P} \quad (3.45a)$$

$$\dot{e}_{\alpha,\beta} = -\frac{v_\alpha}{h_\alpha}(e_{\alpha,\beta} - e_{\alpha,\beta-1}), \quad \alpha \in \mathcal{P}, \quad \beta \in \mathcal{Z}_\alpha \setminus \{1\}, \quad (3.45b)$$

$$\sum_{\alpha \in \mathcal{O}_k} \dot{q}_\alpha e_k + \dot{e}_k q_\alpha = \sum_{\alpha \in \mathcal{I}_k} q_\alpha \dot{e}_{\alpha,n_\alpha} + \dot{q}_\alpha e_{\alpha,n_\alpha}, \quad k \in \mathcal{N}. \quad (3.45c)$$

Eqs. (3.45a, 3.45b) define ODEs for the energy densities on each pipeline, and (3.45c) for the virtual energy density on the node k resulting from conservation of energy. The temporal derivative of the momentum balance integrated in space yields an ODE for the pressure at every network node

$$\dot{\rho}(e_\alpha) = \frac{\partial \rho}{\partial e_\alpha} \dot{e}_\alpha, \quad \dot{\lambda}(e_\alpha, v_\alpha) = \frac{\partial \lambda}{\partial e_\alpha} \dot{e}_\alpha + \frac{\partial \lambda}{\partial v_\alpha} \dot{v}_\alpha, \quad \alpha \in \mathcal{P}, \quad (3.46a)$$

$$\begin{aligned} \frac{d(p_k - p_m)}{dt} = & -\frac{|v_\alpha|}{2d} [2\dot{v}_\alpha \overline{\rho(e_\alpha) \lambda(e_\alpha, v_\alpha)} + v_\alpha \frac{d}{dt} (\overline{\rho(e_\alpha) \lambda(e_\alpha, v_\alpha)})] \\ & - \overline{\rho(e_\alpha)} \frac{d\dot{v}_\alpha}{dt} - (v_\alpha - g z_x^\alpha) \frac{d}{dt} \overline{\rho(e_\alpha)}, \end{aligned} \quad \alpha = (k, m) \in \mathcal{P}. \quad (3.46b)$$

The temporal derivative of the momentum balance (3.46b) contains both the acceleration \dot{v}_α itself and its temporal derivative ($\frac{d}{dt} \dot{v}_\alpha$). First, an ODE for the velocity (a description of the acceleration) is given by applying the temporal derivative to the remaining flow defining equations. This leads to

$$\dot{q}_\alpha = \Phi_\alpha \dot{v}_\alpha, \quad \alpha \in \mathcal{P}, \quad (3.47a)$$

$$\dot{q}_c = \frac{\dot{G}_c(e_k - e_R^c) - G_c \dot{e}_k}{(e_k - e_R^c)^2}, \quad c = (k, m) \in \mathcal{C}, \quad (3.47b)$$

$$\sum_{a \in \delta^{\text{out}}(k)} \dot{q}_a = \sum_{a \in \delta^{\text{in}}(k)} \dot{q}_a, \quad k \in \mathcal{N}. \quad (3.47c)$$

Second, to obtain an ODE for the acceleration in (3.46b), (3.47) have to be differentiated a second time, forming a purely differential system. As a consequence, the resulting DAE is of differentiation index two.

When alternatively neglecting the acceleration contribution in (3.46b), the index of the resulting DAE reduces to one, since (3.47) does not need to be differentiated twice. The same observation results when eliminating the pressure variables by summing (3.46b) over cycles. The resulting $|\mathcal{L}_G|$ equations form a nonlinear system of equations for the determination of cycle flows. When removing the remaining $|\mathcal{P}| - |\mathcal{L}_G|$ equations of type (3.46b), the pressure is not part of the state variables and the DAE is of differentiation index 1.

3.6 Stability

The stability of the system description (3.27) of an arbitrary heating network is analyzed, resulting from spatial discretization of the energy density using the upwind scheme. The discussion is split in the two concepts of Lyapunov and asymptotic stability. The subsequent presentation applies for network topologies and boundary conditions, which allow for the existence of a unique solution, as discussed in section 3.4.

3.6.1 Lyapunov stability

Since the finite-dimensional time-varying system (3.27) is considered, analyzing eigenvalues of the time-varying system operator A is not sufficient [49] to conclude for stability of (3.27). Precisely, the following dynamical system is studied, cf. [50],

$$\dot{x} = f(t, x(t)), \quad x(t_0) = x_0, \quad (3.48)$$

where $f : \mathcal{T} \times \mathcal{X} \mapsto \mathbb{R}^n$ is additionally assumed to be continuous in both arguments to ensure the existence of a classical solution, i.e.

$$f(\cdot, x) \text{ continuous } x \in \mathcal{X} \quad (3.49)$$

$$f(t, \cdot) \text{ continuous } t \in \mathcal{T}. \quad (3.50)$$

With these definitions, stability of the dynamical system can be defined as follows [50]:

Definition 5 ([50]). *A function f defined in (3.48) with equilibrium point \bar{x} is Lyapunov stable, if there exists a positive definite operator $V : \mathcal{T} \times D \mapsto \mathbb{R}^+$, $V(x) = 0$ iff $x = \bar{x}$, where D is a neighborhood of \bar{x} , such that*

$$\frac{d}{dt}V(t, x) \leq 0, \quad t \in \mathcal{T}, x \in \text{int}(D), \quad (3.51)$$

where $\text{int}(D)$ is the interior of D . Asymptotic stability results from strict definiteness of (3.51).

Steady states

For a thermal control u_T , which is constant in time, the existence of steady states as required for a stability analysis shall be evaluated subsequently. For the following considerations, flow and return network are considered independently by a generic network with $|u|$ injection points of thermal energy.

Theorem 6. *For the description of the energy transport as defined in (3.27), there exist constant in time thermal controls \bar{u} , forming steady states $\bar{e}(\bar{u})$. By conservation of energy, the components of $\bar{e}(\bar{u})$ are within the convex hull of the thermal inputs in \bar{u} .*

Proof of Theorem 6. The ODE of the discretized energy densities resulting from the upwind scheme on pipeline $\alpha = (k, m) \in \mathcal{P}$ reads

$$\begin{aligned}\dot{e}_{\alpha,j} &= -\frac{v_\alpha}{h_\alpha}(e_{\alpha,\beta} - e_{\alpha,\beta-1}), \quad \beta \in \mathcal{N}_\alpha \setminus \{1\} \\ \dot{e}_{\alpha,1} &= -\frac{v_\alpha}{h_\alpha}(e_{\alpha,1} - e_k).\end{aligned}$$

An equilibrium results by $\bar{e}_{\alpha,\beta} = e_k$, $\beta \in \mathcal{Z}_\alpha$. Due to the conservation of energy (3.20c), in combination with volume conservation on each node (3.21a), e_k is given by a convex combination of incoming energy densities

$$e_k \in \left[\min_{i \in \mathcal{I}_k} \{e_{i,n_i}\}, \max_{i \in \mathcal{I}_k} \{e_{i,n_i}\} \right], \quad k \in \mathcal{N}. \quad (3.52)$$

This allows to conclude that the components of the resulting equilibrium state vector are within the minimum and maximum injected thermal controls,

$$\min_{k \in [1, \dots, |u|]} \bar{u}_k \leq \bar{e}_{\alpha,\beta} \leq \max_{k \in [1, \dots, |u|]} \bar{u}_k, \quad \beta \in \mathcal{Z}_\alpha, \alpha \in \mathcal{P},$$

where $|u|$ is the dimension of the equilibrium control vector \bar{u} . □

For flow and return network, the corresponding controls allowing for steady states in line with technical constraints read

$$\begin{aligned}\bar{u}_F : \mathcal{T} &\mapsto [e_{\min}^F, \infty), \\ \bar{u}_R : \mathcal{T} &\mapsto (e_R^1, \dots, e_R^{|\mathcal{C}|})^T, \subset \mathbb{R}^{|\mathcal{C}|},\end{aligned}$$

where e_{\min}^F is the minimum allowed energy density at consumer stations in the flow network. The velocity vector v used above is now defined by the flow defining equations for the equilibrium energy densities $\bar{e}(\bar{u})$.

Lyapunov inequality

For a quadratic Lyapunov function $V(t, x) = x^T Q x$ with a positive semi-definite, symmetric, constant in time Kernel $Q \in \mathbb{R}^{n \times n}$, (3.51) is equivalent to

$$x^T Q f(t, x) + f^T(t, x) Q x \leq 0 \quad x \in \mathcal{X}, t \in \mathcal{T}. \quad (3.53)$$

Focusing on the network setup, Lyapunov stability does not follow trivially ($Q = \mathbb{1}$), since A needs not to be negative semi-definite (nsd). To illustrate this, the example of two aligned pipelines with velocities v_1, v_2 and a cell length h is considered, where each pipeline receives one finite-volume cell. In this setup the operator A reads

$$A = \frac{1}{h} \begin{pmatrix} -v_1 & \\ v_2 & -v_2 \end{pmatrix}.$$

Here, the definiteness of A depends on the ratio $r = v_1/v_2$, which changes with the pipeline diameters. For $r < 0.25$ the matrix is indefinite. In contrast, the matrix QA is negative semi-definite (nsd), when choosing Q as a diagonal matrix carrying the volume of the finite volume cells of each pipeline, $\Phi \cdot h$. The ordering function f_Z considered subsequently was introduced in (3.25). This motivates the following theorem.

Theorem 7. *For the system operator $A(q)$ of the control system (3.27) defined in (3.24), the following holds. There exists a global, diagonal, positive definite energy matrix $Q \in \mathbb{R}^{n \times n}$, such that for every fixed volume flow field \bar{q} satisfying volume conservation (3.21a),*

$$M = (QA(\bar{q}))^T + (QA(\bar{q})) \leq 0. \quad (3.54)$$

Remark 8.

1. Q can be constructed with positive diagonal elements

$$Q_i \equiv \text{diag}(Q) = Q_{f_Z(i,j),f_Z(i,j)} = \Phi_i h_i, \quad i \in \mathcal{P}, \quad j \in \mathcal{Z}_i.$$

The latter carry the volume $\Phi_i h_i$ of each of the discretization cells on edge i .

2. Since (3.54) holds for all volume flows q satisfying volume conservation (3.21a), $V(e) = (e - \bar{e})^T Q (e - \bar{e})$ forms a Lyapunov function for the system (3.27) with the constant in time control \bar{u} .
3. Note that also a change in the flux direction which yields a structural modification in the system matrix $A(q)$ leads to a stable system by transformation with Q .

Proof of Theorem 7. For the following considerations, we choose the orientation of each edge velocity such that $v_i \geq 0 \quad \forall i \in \mathcal{E}$. Hence, velocities and the corresponding volume flows are non-negative. Proving that the symmetric matrix M is negative semi-definite amounts to show that M has non-positive diagonal elements, and is weakly (row- and column) diagonally dominant,

$$\sum_{j=1, i \neq j}^n |M_{ij}| \leq |M_{jj}|. \quad (3.55)$$

With these properties, [51] theorem 6.1.1 allows to conclude that all eigenvalues of M are non-positive and by [51] theorem 4.1.8 a hermitian matrix with non-positive eigenvalues is negative semi-definite. For the following proof, a reference pipeline $i = (a, b) \in \mathcal{P}$ is considered, cf. fig. 3.7. Based on the coupling types (3.16), one obtains for $A' \equiv QA(\bar{q})$

$$A'_{f_Z(i,j),f_Z(i,j)} = -Q_i \frac{v_i}{h_i} = -q_i, \quad j \in \{1, \dots, n_i\}, \quad (3.56a)$$

$$A'_{f_Z(i,j),f_Z(i,j-1)} = Q_i \frac{v_i}{h_i} = q_i, \quad j \in \{2, \dots, n_i\}, \quad (3.56b)$$

$$A'_{f_Z(i,1),f_Z(j,n_j)} = a'_{ij} = Q_i \frac{v_i}{h_i} \frac{\Phi_j v_j}{\sum_{k \in \mathcal{O}_a} \Phi_k v_k} = q_i \frac{q_j}{\sum_{k \in \mathcal{O}_a} q_k}, \quad j \in \mathcal{I}_a. \quad (3.56c)$$

Focusing on rows describing cells at the inflow boundary of an arbitrary edge $i \in \mathcal{E}$ yields the following off-diagonal elements

$$\begin{aligned}
\sum_{k \neq f_{\mathcal{Z}}(i,1)} |M_{f_{\mathcal{Z}}(i,1),k}| &= \sum_{k \neq f_{\mathcal{Z}}(i,1)} |A'_{k,f_{\mathcal{Z}}(i,1)} + A'_{f_{\mathcal{Z}}(i,1),k}| \\
&\leq |A'_{f_{\mathcal{Z}}(i,2),f_{\mathcal{Z}}(i,1)}| + \sum_{j \in E_i^+} |A'_{f_{\mathcal{Z}}(i,1),f_{\mathcal{Z}}(j,n_j)}| \\
&= q_i + \sum_{j \in \mathcal{I}_a} a'_{ij}.
\end{aligned}$$

Finally, we calculate the sum of off-diagonal cells at the outflow boundary,

$$\begin{aligned}
\sum_{k \neq f_{\mathcal{Z}}(i,n_i)} |M_{f_{\mathcal{Z}}(i,n_i),k}| &= \sum_{k \neq f_{\mathcal{Z}}(i,n_i)} |A'_{f_{\mathcal{Z}}(i,n_i),k} + A'_{k,f_{\mathcal{Z}}(i,n_i)}| \\
&\leq |A'_{f_{\mathcal{Z}}(i,n_i),f(i,n_i-1)}| + \sum_{j \in \mathcal{O}_b} |A'_{f_{\mathcal{Z}}(j,1),f(i,n_i)}| \\
&= q_i + \sum_{j \in \mathcal{O}_b} a'_{ji}.
\end{aligned}$$

Hence, it remains to verify the two inequalities

$$q_i \geq \sum_{j \in \mathcal{I}_a} a'_{ij} = q_i \frac{\sum_{j \in \mathcal{I}_a} q_j}{\sum_{k \in \mathcal{O}_a} q_k} \quad \text{and} \quad q_i \geq \sum_{j \in \mathcal{O}_b} a'_{ji} = q_i \frac{\sum_{j \in \mathcal{O}_b} q_j}{\sum_{k \in \mathcal{O}_b} q_k} = q_i.$$

The second is clear, while the first follows from the volume conservation property at node a . \square

It shall be noted that the solution in theorem 7 is in general not unique. If Q solves the Lyapunov inequality, $\tilde{Q} = cQ$, $c \in \mathbb{R}^+$, is a solution, as well. Furthermore, the example of one pipeline with n discretization cells is considered, expressed by the system operator $A(\bar{q}) \in \mathbb{R}^{n \times n}$ for a fixed volume flow field \bar{q} . Defining the energy matrix as $Q = \Phi_k h c_k$, $k \in [1, ..n]$, $c_k \in \mathbb{R}^+$ also leads to a Lyapunov stable system if additionally $c_k \leq 2c_{k-1}$, $k \in [2, .., n-1]$. Thus, even the diagonal elements of Q can be chosen differently.

3.6.2 Comparison of volume- and mass conservation

To obtain Lyapunov stability in theorem 7, we focused on the energy density coupling to volume flows and additionally claimed the conservation of volume over node k . To show that this is a natural description due to the finite volume discretization of the energy density, conservation of mass is considered subsequently. As we will see, the proof of theorem 7 does not work for conservation of mass in the identical manner. However, based on this finding conservation of mass does not necessarily lead to an unstable system.

We start by assuming conservation of mass over each network node

$$\sum_{\alpha \in \delta^{\text{out}}(k)} \rho(t, 0) q_{\alpha}(t) = \sum_{\alpha \in \delta^{\text{in}}(k)} \rho(t, L_{\alpha}) q_{\alpha}(t), \quad (3.57)$$

in combination with energy conservation

$$\begin{aligned} \sum_{\alpha \in \delta^{\text{out}}(k)} \beta_{\alpha}(t, 0) E_{\alpha}(t, 0) &= \sum_{\alpha \in \delta^{\text{in}}(k)} \beta_{\alpha}(t, L_{\alpha}) E_{\alpha}(t, L_{\alpha}), \\ E^a(t, 0) &= E^k(t), \quad a \in \mathcal{O}_k. \end{aligned}$$

Here, E acts as a placeholder for energy density (energy per unit volume), when β refers to volume flows, and for the specific energy (energy per unit mass), when β refers to mass flows. Applying the upwind discretization to E and forming $A(v)$ as described above yields,

$$\begin{aligned} A'_{f_{\mathcal{Z}}(i,j), f_{\mathcal{Z}}(i,j)} &= -Q_i \frac{v_i}{h_i} = -q_i, \quad j \in \{1, \dots, n_i\} \\ A'_{f_{\mathcal{Z}}(i,j), f_{\mathcal{Z}}(i,j-1)} &= Q_i \frac{v_i}{h_i} = q_i, \quad j \in \{2, \dots, n_i\} \\ A'_{f_{\mathcal{Z}}(i,1), f_{\mathcal{Z}}(j,n_j)} &= a'_{ij} = Q_i \frac{v_i}{h_i} \frac{\beta_j}{\sum_{k \in \mathcal{O}_b} \beta_k} = q_i \frac{\beta_j}{\sum_{k \in \mathcal{O}_b} \beta_k}, \quad j \in \mathcal{I}_a. \end{aligned}$$

Following the steps discussed in theorem 7, showing weak diagonal dominance reduces to the two inequalities,

$$q_i \geq \sum_{j \in \mathcal{I}_a} a'_{ij} = \sum_{j \in \mathcal{I}_a} q_i \frac{\beta_j}{\sum_{k \in \mathcal{O}_b} \beta_k} = q_i \frac{\sum_{j \in \mathcal{I}_a} \beta_j}{\sum_{k \in \mathcal{O}_b} \beta_k}, \quad (3.59)$$

$$q_i \geq \sum_{j \in \mathcal{O}_b} a'_{ji} = \sum_{j \in \mathcal{O}_b} q_j \frac{\beta_i}{\sum_{k \in \mathcal{O}_b} \beta_k}. \quad (3.60)$$

Eq. (3.59) is fulfilled by defining β to be a mass flow, which is conserved by (3.57). Inserting the mass flow for β in (3.60) leads to

$$q_i \geq q_i \frac{\sum_{j \in \mathcal{O}_b} q_j \rho_i}{\sum_{k \in \mathcal{O}_b} q_k \rho_k} = q_i \frac{\rho_i}{\rho_o},$$

since the outgoing densities are equal and form $\rho_o(E)$. Thus, for weak diagonal dominance, all mass densities entering node k have to be less or equal the mass density exiting node k which is not feasible generally. As a counter example we consider case of two specific energies E_1, E_2 entering node k , carried by identical mass flows $m_1 = m_2$. In the range in which heating networks operate, the mass density is a monotone function of the specific energy. Thus, the outgoing energy density will be the average of the incoming energy densities. This leads to the fact that $\rho_o \in (\rho_1, \rho_2)$.

3.6.3 Asymptotic stability

Based on Lyapunov stability discussed in section 3.6.1, asymptotic stability is analyzed subsequently. This task splits in two parts. In the first part, asymptotic stability is proven in the absence of flux changing edges. In the second part stability is analyzed for networks which possibly contain volume flow fields with zero components.

For the first part, networks are considered which topologically exclude changes of flux direction as well as networks, in which changes of flux direction do not occur by the chosen consumption signal. To state the main theorem, several definitions have to be made. An external node k_e in a heating network is a node where all coupling pipelines contribute volume flows which only effectively enter or only effectively exit node k_e . By pressure continuity (2.10), a heating network has at least one external inflow and one external outflow node. External nodes are the nodes in the flow and return network, corresponding to the power plant as well as the consumers, cf. fig. 3.9. A matrix is

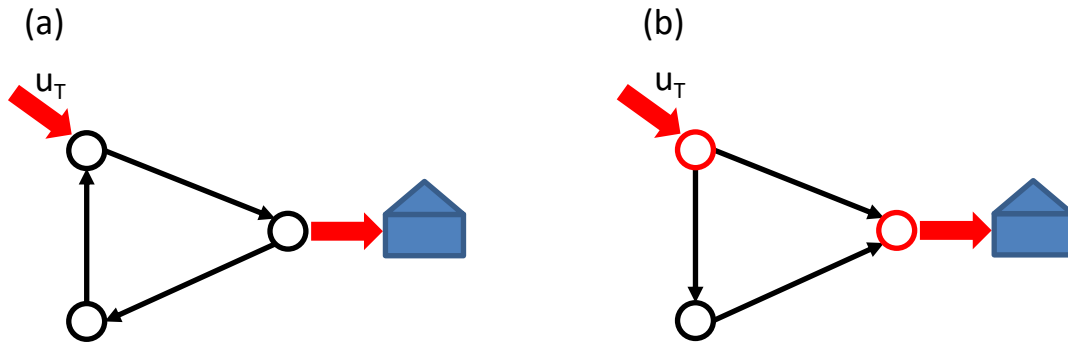


Figure 3.9: Network (a) visualizes a flow field containing a circular flow which violates the assumption of remark 1 resulting from the pressure continuity in every node. Network (b) exhibits external nodes marked in red, at which all pipelines (black lines) only enter or exit the node. These coincide with the points at which the power plant contributes and the consumers extract thermal energy.

weakly chained diagonally dominant (wcdd) if it is weakly diagonally dominant, and for every row which is weakly diagonally dominant, there exists a path to a row which is strictly diagonally dominant [52]. The notion path is related to the graph formed by the entries of the matrix M . Matrix M defined in (3.54) defines an adjacency matrix of an unweighted graph. Its nodes are formed by the finite volume cells and its edges are the connection of the cells defined by the upwind scheme. Thus, if cells i, j couple, the entry $M_{ij} = M_{ji} \neq 0$ by symmetry. The graph described by the finite volume cells and defined by M is not identical to the graph of the heating network but both are related by conservation of energy coupling finite volume cells of the border of pipelines. For the following consideration, flow and return part of the network can

be modeled jointly in A , as well as only one of the two parts, since the considered graph of the heating network needs not to be connected to show the wcdd property. The exclusion of circular velocity fields used in the following theorem is ensured by pressure continuity in combination with remark 1.

Theorem 9. *We consider a velocity flow field \bar{q} satisfying volume conservation, which does not contain any circular flows and only consists of nonzero components, $\bar{q}_i \neq 0$, $i \in \mathcal{P}$. For these assumptions, the matrix $M = QA(\bar{q}) + (QA(\bar{q}))^T$ resulting from upwind discretization of advection on a graph is weakly chained diagonally dominant (wcdd).*

Proof of Theorem 9. One first notes that every finite volume cell is connected to an external node via a path formed by adjacent cells. To see this, cell $i \in \mathcal{Z}_\alpha$ is considered on an arbitrary pipeline α . By discretization utilizing the upwind scheme, cell i is connected to the row of its neighboring cells $j \in \{i-1, i+1\}$. Note that the entries in M connecting cells i, j are indeed nonzero by assumption. Hence, all cells on pipeline α form a path $\mathcal{Z}_\alpha \in \mathcal{C}$. If pipeline α is not attached to other pipelines, it exhibits two external nodes proving the claim. If it is attached to neighboring pipelines \mathcal{P}_n , there exist nonzero entries in M coupling the border cells of α to the border cells of neighboring pipelines. The path of connected cells is thus augmented by all cells on neighboring pipelines, $\mathcal{C} = \mathcal{C} \cup \mathcal{Z}_k$ $k \in \mathcal{P}_n$. This argument is continued recursively, until each iteration ends in an external node. Due to the assumption that circular velocity fields are excluded, proceeding along a velocity field, the resulting path can not be cyclic and thus must start and end in at least two different external nodes, cf. remark 1.

The second observation is that all cells next to an external node k_e form strictly diagonally dominant rows in M . To see this, consider border cell b on one of the pipelines P_e adjacent to N_e . For the diagonal element one obtains $M(b, b) = -2q_{P_e}$. Since all flows either enter or exit N_e , cell b can only either couple to one adjacent cell on the same pipeline P_e or to cells on other pipelines combined at an inner node N_i , $i \neq e$. In the first case, the off diagonal element reads $q_{P_e} < |M(b, b)|$. In the second case, the off-diagonal elements of outrunning pipelines sum to $\sum_{j \neq b} M_{b,j} = q_{P_e} < |M(b, b)|$. Hence, $M(b, :)$ is strictly diagonally dominant. \square

Theorem 9 implies that $M < 0$. In particular, the system is asymptotically stable to the equilibrium points defined above, which can be seen as follows. One notes that by volume conservation, theorem 7 allows to conclude that $M \leq 0$. The property wcdd yields $M \neq 0$, since wcdd matrices are non singular [52] which allows to conclude that $M < 0$. Since this observation is independent of the velocity flow field within the mentioned assumptions, asymptotic stability follows. Since flow- and return network are thermally decoupled, the graph of the matrix M defined by its finite volume cells is not connected, but consists of a flow- and a return part. Still, by theorem 9, both operators describing the flow $A_F(\bar{q})$ and the return $A_R(\bar{q})$ network equipped with an upwind discretization are wcdd. Combining both to a global system matrix A yields

a wcd matrix $A(\bar{q})$ since every row of $M(\bar{q})$ is part of a path leading to a strictly diagonally dominant row.

Counterexample for asymptotic stability in case of flux changes

In the second part, the stability of a dynamical system is analyzed, in which at least one pipeline changes its flux direction. To this end, the network in fig. 3.10 is considered, allowing for a change of flux direction on edge 2-3. It is sufficient for this example to only consider the flow network. The aim is to construct a situation, in which a zero velocity on edge 2 – 3 is persistent for infinite times. To this end, equal diameters,

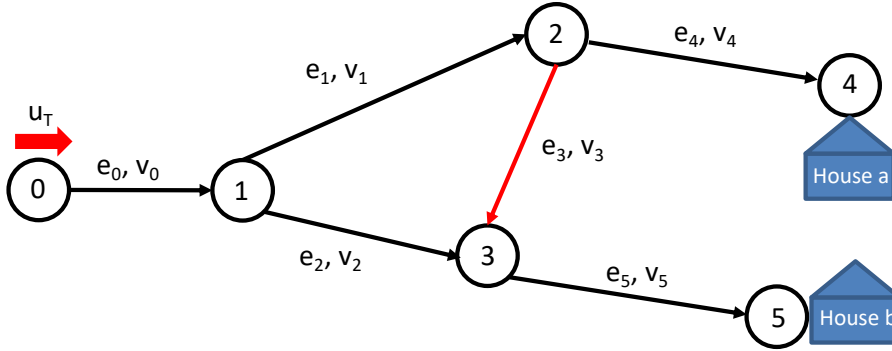


Figure 3.10: Minimum example for a flow network in which a change of flux direction is possible (edge 2-3). For the corresponding velocity $v_3 = 0$, the system matrix resulting from upwind discretization A loses full rank.

$d_i = d$, $i \in \mathcal{P}$ and lengths $L_i = L$, $i \in \mathcal{P}$ of the pipelines are assumed. The length of finite volume cells is fixed to a constant value $h_i = h$, $i \in \mathcal{P}$. Each pipeline velocity is thus related to its volume flow by a constant factor Φ . In this special situation the energy matrix $Q = \mathbb{1}$ yielding Lyapunov stability is trivial. After discretization of the PDE in space using one finite volume cell on each pipeline, the following operators result

$$A = \frac{1}{h} \begin{pmatrix} -v_0 & & & & & \\ v_1 & -v_1 & & & & \\ & v_2 & -v_2 & & & \\ & v_3^b & v_3^a & -v_3 & & \\ & v_4^b + v_1^a & v_3^a & -v_4 & & \\ & & v_5^a + v_2^b & v_3^b & -v_5 & \end{pmatrix}, \quad B = \frac{q_a + q_b}{h\Phi} \begin{pmatrix} 1 \\ 0 \\ \vdots \\ 0 \end{pmatrix}.$$

The boundary condition defining the volume flow at consumer stations is solved to

$$q_a(t) = \frac{G_a(t)}{e_4(t) - e_R}, \quad q_b(t) = \frac{G_b(t)}{e_5(t) - e_R}, \quad (3.61)$$

where the return energy density is assumed to be identical for both consumers. The effect of flux changes is mapped to the velocities using the following notation,

$$v_{i,j}^a = \begin{cases} v_{i,j} & : q_a \geq q_b \\ 0 & : q_a < q_b \end{cases},$$

and vice versa for $v_{i,j}^b$ if $q_b \geq q_a$. Furthermore the pressure continuity applied to the cycle $1 - 2 - 3 - 1$ is solved by

$$q_{23} = \begin{cases} -(q_a + q_b - \sqrt{2}\sqrt{q_a(q_a + q_b)}) & : q_a \geq q_b \\ q_a + q_b - \sqrt{2}\sqrt{q_b(q_a + q_b)} & : q_b > q_a. \end{cases}.$$

If both houses induce the same volume flow $q_a = q_b$, it follows that $v_{23} = q_{23}/\Phi = 0$. Hence, A is singular in this case. To violate asymptotic stability, it must be shown that boundary conditions exist, for which the singularity induced by the algebraic equations is persistent. To this end, identical consumptions $G_a(t) = G_b(t)$, $t \in \mathcal{T}$ are assumed in addition to the thermal control $u(t) = u_0$, $t \in \mathcal{T}$. For the initial state

$$e_0 = \begin{cases} \theta_0 & : i \in \mathcal{P}, i \neq 3 \\ \theta_3 & : i = 3 \end{cases},$$

the chosen controls force energy densities at houses a, b to develop synchronously, $e_4(t) = e_5(t)$, $t \in \mathcal{T}$, for all initial states $e_{\min} \leq \theta_0, \theta_3 \leq e_{\max}$, since the paths to both consumers a, b are symmetric by construction. Here, θ_0 and θ_3 denote the initial energy density on pipelines 1, 2, 4, 5, 6 and pipeline 3 respectively. In this case, the system state converges to

$$\lim_{t \rightarrow \infty} e(t) = \bar{e} = \begin{cases} u_0 & : i \in \mathcal{P}, i \neq 3 \\ \theta_3 & : i = 3 \end{cases}.$$

For $\delta > 0$ a class of initial vectors is defined

$$e_0^\epsilon = \begin{cases} \theta_0 & : i \in \mathcal{P}, i \neq 3 \\ \theta_3 + \epsilon & : i = 3 \end{cases}, \quad \text{s.t. } 0 < \epsilon < \delta.$$

For the initial state e_0^ϵ it results that

$$\|e_0^\epsilon - \bar{e}\| = \epsilon < \delta \quad \Rightarrow \quad \lim_{t \rightarrow \infty} \|e(t) - \bar{e}\| = \epsilon > 0, \quad (3.62)$$

which means that the system does not converge to an equilibrium point. Since this is true for all admissible time-constant controls u_0 , the equilibrium points of networks without flux changes discussed previously are not necessarily asymptotically stable for networks including changes of flux direction.

It shall be noted that the constructed scenario can be realized by an appropriate control of the input energy density for the presented network topology. Still, the configuration allowing for a persistent zero velocity on a flux changing edge is rather unstable and unlikely to occur for practical controls on existing heating networks. Furthermore,

the presented example suggests that the subnetwork Σ_r and its energy densities e_r formed by removing the flux changing edges from the full network topology is still asymptotically stable. This conjecture is motivated by the fact that a graph in which flux changing edges are removed is still connected by pressure continuity. Hence, Σ_r is wcd and theorem 9 applies to conclude for asymptotic stability. This claim however remains without a rigorous proof.

3.7 Controllability and observability

Within this section, the controllability and the observability of the control system (3.27) are analyzed. For linear time-invariant systems, the initial state $x_0 \in \mathcal{X}$ is called controllable to the zero state, if there exists an unconstrained control \hat{u} , steering the system to the zero state within a finite time $\hat{t} < \infty$ [22]. A state $\hat{x} \in \mathcal{X}$ is unobservable, if the output resulting from a zero control $\hat{u}(t) = 0$ and the initial condition $x_0 = \hat{x}$ is zero for all times $y(t) = 0$, $t \geq 0$ [22]. For time-varying systems, both concepts require the evaluation of the fundamental solution matrix. However, deriving an analytical solution is not always possible even for simple network topologies of district heating networks. Still, a characterization of the time-varying system can be performed by considering local linear time invariant models for fixed velocity fields \bar{q} . To this end, the operator pair $(A(\bar{q}), B(\bar{q}))$ is considered with $A(\bar{q}) \in \mathbb{R}^{n \times n}$, $B(\bar{q}) \in \mathbb{R}^{n \times |u|}$, resulting from the velocity field \bar{q} . The corresponding linear time-invariant system is completely controllable, iff [22]

$$\text{rank}([s\mathbb{1} - A(\bar{q}), B(\bar{q})]) = n, \quad \forall s \in \mathbb{C}.$$

Similarly, the linear time-invariant system of the operator pair $(A(\bar{q}), C)$ with $A(\bar{q}) \in \mathbb{R}^{n \times n}$, $C \in \mathbb{R}^{n \times |y|}$ is observable, iff [22]

$$\text{rank} \begin{pmatrix} s\mathbb{1} - A(\bar{q}) \\ C \end{pmatrix} = n, \quad \forall s \in \mathbb{C}.$$

Spectrum of the system operators

Before focusing on observability and controllability, the closely related spectrum of $A(\bar{q})$ shall be analyzed for fixed velocity fields \bar{q} . The eigenvalues of the full system are given by the negative transport velocities divided by the length of the discretization cells h_α , $\alpha \in \mathcal{P}$. For networks without flux-changes, $\bar{q}_\alpha \neq 0$, $\alpha \in \mathcal{P}$, thus all eigenvalues of $A(\bar{q})$ are strictly negative.

A proof of this claim based on the structure of the system matrix $A(\bar{q})$ is given as follows. Due to pressure continuity (2.10) and the exclusion of circular velocity fields, cf. remark 1, every discretization cell can be classified by its distance to the source. By the structure of the upwind discretization, the temporal derivative of each finite

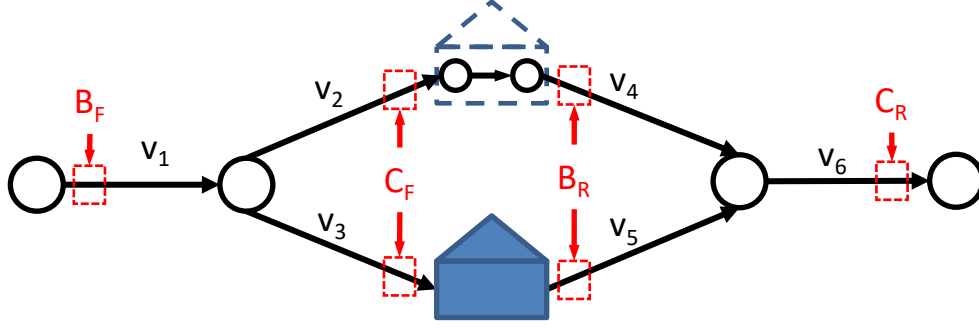


Figure 3.11: Example network to study observability and controllability.

volume cell only depends on cells upward the flow direction. Hence, by assigning rows and columns of $A(\bar{q})$ to cells according to their distance to the source yields a lower triangular matrix $A(\bar{q})$. For the upwind scheme, the diagonal elements of $A(\bar{q})$ carry the negative advection velocities divided by the length of the discretization cells. The fact that eigenvalues of triangular matrices are given by their diagonal elements proves the claim.

This allows to characterize observability and controllability of the locally linear system descriptions of heating networks. The systems operators A_F, B_F correspond to the flow- and A_R, B_R to the return part of a heating network, cf. fig. 3.11.

Theorem 10. *There exist nontrivial flow networks with volume flow configurations \bar{q}_F , in which the pair $(A_F(\bar{q}_F), B_F(\bar{q}_F))$ is not controllable. Vice versa, there exist nontrivial return networks with velocity configurations \bar{q}_R , in which the pair $(A_R(\bar{q}_R), C_R(\bar{q}_R))$ is not observable. Consequently, there exist velocity configurations for which the composed operators for flow- and return network are neither controllable, nor observable.*

Proof of Theorem 10. As a counter example confirming the claim, the network visualized in fig. 3.11 splitting from one source pipeline with velocity v_1 to two pipelines with velocities v_2, v_3 is considered, with a symmetric return network. The input and output operators for flow and return network exhibit the ranks $\text{rank}(B_F) = \text{rank}(C_R) = 1$, and $\text{rank}(C_F) = \text{rank}(B_R) = 2$. To illustrate the structure of the system operators A_F, A_R , the Kernel $s\mathbb{1} - A_F(\bar{q}_F)$ in the flow network for one discretization cell on each pipeline is presented

$$\begin{pmatrix} s + \frac{v_1}{h_1} & & & & & & & & \\ \frac{v_1}{h_1} & s + \frac{v_1}{h_1} & & & & & & & \\ & -\frac{v_1}{h_1} & s + \frac{v_1}{h_1} & & & & & & \\ -\frac{v_2}{h_2} & & & s + \frac{v_2}{h_2} & & & & & \\ & & & -\frac{v_2}{h_2} & s + \frac{v_2}{h_2} & & & & \\ & & & & -\frac{v_2}{h_2} & s + \frac{v_2}{h_2} & & & \\ -\frac{v_3}{h_3} & & & & & & s + \frac{v_3}{h_3} & & \\ & & & & & & -\frac{v_3}{h_3} & s + \frac{v_3}{h_3} & \\ & & & & & & & -\frac{v_3}{h_3} & s + \frac{v_3}{h_3} \end{pmatrix}.$$

The extension to the case of multiple finite volume cells is straight forward. For the volume flow vector $\bar{q}_F = (\Phi_1 v_1, \Phi_2 v_2, \Phi_3 v_3)$, in which the following holds, $v_2/h_2 = v_3/h_3$, the choice $s = s^* = -v_2/h_2$ leads to $s^* + \frac{v_2}{h_2} = s^* + \frac{v_3}{h_3} = 0$. Thus, the columns corresponding to the state variables entering the two consumers are identically 0, and the rank of $A_F(\bar{q}_F)$ reduces to

$$\text{rank}(s^*\mathbb{1} - A_F(\bar{q}_F)) = n_F - 2 < n_F - \text{rank}(B_F),$$

where n_F refers to the number of discretization cells in the flow network. By conservation of volume, this velocity field can be realized, if the volume flows at houses a, b satisfy

$$\frac{q_a}{h_2 \Phi_2} = \frac{q_b}{h_3 \Phi_3}.$$

Similarly, if the volume flow vector $\bar{q}_R = (\Phi_4 v_4, \Phi_5 v_5, \Phi_6 v_6)$ satisfies $v_4/h_4 = v_5/h_5$, this allows to conclude

$$\text{rank}(s^*\mathbb{1} - A_R(\bar{q}_R)) = n_R - 2 < n_R - \text{rank}(C_R).$$

where n_R refers to the number of discretization cells in the return network. The choice for \bar{q}_R can be realized by the following volume flows at the consumers stations

$$\frac{q_a}{h_4 \Phi_4} = \frac{q_b}{h_5 \Phi_5}.$$

Consequently, the pair (A_R, B_R) is not observable for the distinct volume flow vector. Since the volume flows discussed for flow- and return network can be realized simultaneously by a corresponding ratio of cross sections Φ and discretization lengths h , the pair (A, B) is not controllable and (A, C) not observable. \square

3.8 Port-Hamiltonian systems

3.8.1 Nonlinear port-Hamiltonian systems

Port-Hamiltonian (pH) systems [53, 54] have become a popular concept since they relate desired properties of a system such as stability and passivity to its underlying state space description [55, 56, 57]. To properly define passivity, the following generic nonlinear system is considered,

$$\dot{x} = f(x, u), \quad x(t_0) = x_0, \quad (3.63a)$$

$$y = h(x, u), \quad (3.63b)$$

where \mathcal{X} denotes the state space, $x_0 \in \mathcal{X}$ the initial state, u the input vector resulting from the input space \mathcal{U} , and y the output vector within the output space \mathcal{Y} . The functions $f : \mathcal{X} \times \mathcal{U} \mapsto \mathbb{R}^n$, $h : \mathcal{X} \times \mathcal{U} \mapsto \mathcal{Y}$ should be continuous in the input u and Lipschitz-continuous in space x to ensure for a unique solution of (3.63) for time-continuous input signals. Here, \mathcal{T} is the considered time domain. System (3.63) is passive, if and only if there exists a storage function $H : \mathcal{X} \mapsto \mathbb{R}$ such that

$$H(x(t_1)) - H(x(t_0)) \leq \int_{t_0}^{t_1} u^T(t)y(t) dt, \quad \forall t_0 \leq t_1 \in \mathcal{T}, \quad (3.64)$$

for all (u, x, y) satisfying (3.63). The increase in internal energy of the system is majorized by the external (port-based) inflow of energy at any time. For pH systems, the function H is referred to as the Hamiltonian representing the internal energy of the described system. To allow for an energy interpretation, H is usually restricted to be a non-negative function. Furthermore, it serves as a basis for the construction of a Lyapunov function, showing that unforced ($u = 0$), minimal port-Hamiltonian systems are implicitly Lyapunov stable [58]. A state space representation of nonlinear pH systems is given by

$$\dot{x} = (J - R)\nabla_x H(x) + (B - P)u \quad (3.65a)$$

$$y = (B + P)^T \nabla_x H(x) + (S + N)u. \quad (3.65b)$$

The matrices $S = S^T$, $N = -N^T$, describe the feed-through from input to output, $B \pm P$ are the port matrices relating the state variable x and its temporal derivative to inputs and outputs. Most importantly, $R = R^T$ describes the dissipation of energy from the system to its environment, while $J = -J^T$ represents the conversion of energy within the system by e.g. rotational degrees of freedom. The essential property allowing to conclude for passivity as defined in (3.64) is that

$$W = \begin{pmatrix} R & P \\ P^T & S \end{pmatrix} \geq 0. \quad (3.66)$$

The block matrix W equipped with the above operators has to be positive semi-definite to obtain passivity. For a differentiable Hamiltonian, taking its temporal derivative

and inserting the system description (3.65) confirms the inequality (3.64) if (3.66) holds. A special case of (3.65) are linear time invariant port-Hamiltonian systems, in which the Hamiltonian is a quadratic function of the state space variables, $H = x^T Q x$. The matrix $Q \in \mathbb{R}^{n \times n}$ is the positive definite and symmetric energy matrix acting as the kernel of the Hamiltonian. For a general linear time invariant system

$$\dot{x} = Ax + Bu, \quad x(0) = x_0, \quad (3.67a)$$

$$y = Cx + Du, \quad (3.67b)$$

where $A \in \mathbb{R}^{n \times n}$, $B \in \mathbb{R}^{n \times i}$, $C \in \mathbb{R}^{i \times n}$, $D \in \mathbb{R}^{i \times o}$, the positive real lemma [22] allows to derive a similar result to (3.66). In particular, system (3.67) is passive if and only if there exists a positive definite, symmetric solution Q to the LMI [22]

$$\begin{pmatrix} A^T Q + QA & QB - C^T \\ B^T Q - C & -D - D^T \end{pmatrix} \leq 0.$$

Port-Hamiltonian systems are well suited for modeling energy networks. Using energies as a common description variable allows to couple models for different types of energy networks such as electrical, gas- or heating networks. Furthermore, a composition of pH systems remains pH. Thus, if different subnetworks described as port-Hamiltonian system are connected, the resulting system will automatically incorporate passivity and stability. This fact is in particular important for electrical circuits, which served as the main applications of pH systems initially. Since pH systems are formulated closely to the underlying physical conservation laws, they allow to choose natural state variables. Finally a reduced order model obtained by a certain class of Petrov-Galerkin projections remains pH, if the full order model was pH, which is used and described in chapter 4.

3.8.2 Semi-discrete port-Hamiltonian description for heating networks

The control system obtained from upwind discretization of the energy transport on pipelines is shown to be Lyapunov stable in section 3.6. To allow for a pH description, the input- and output operators must fulfill additional properties defined in (3.66). Specifically, the input- and output spaces have to be of identical size to form the dissipation function $u^T y$. It shall be noted that passivity is a special case of dissipativity, in which a generalized dissipation function

$$s(u, y) = \begin{pmatrix} u(t) \\ y(t) \end{pmatrix}^T S \begin{pmatrix} u(t) \\ y(t) \end{pmatrix}$$

is considered in the inequality (3.64). This allows to describe the energy balance of systems for which the input- and output spaces are not of equal dimension. Subsequently, an embedding of the control system (3.27) to the port-Hamiltonian description is discussed.

Linear time varying parameter systems

An important generalization of linear time-invariant pH systems is given by linear time varying pH systems [58], which naturally occur by linearization of nonlinear dynamical systems. A state space representation appears as [58]

$$E\dot{x} = [(J - R)Q - EK]x + (B - P)u \quad (3.68a)$$

$$y = (B + P)^T Qx + (S + N)u, \quad (3.68b)$$

where $E, Q \in C^1(\tau, \mathbb{R}^{n \times n})$, $J, R, K \in C^0(\tau, \mathbb{R}^{n \times n})$, $B, P \in C^0(\tau, \mathbb{R}^{n \times |u|})$. System (3.68) is of pH type, if $\forall t \in \tau$

$$\begin{aligned} Q^T(t)E^T(t) &= E^T(t)Q(t), \\ \frac{d}{dt}(Q^T(t)E^T(t)) &= Q(t)^T[E(t)K(t) - J(t)Q(t)] \\ &\quad + [E(t)K(t) - J(t)Q(t)]^T Q(t), \\ Q^T(t)E(t) - H_0 &\geq 0, \\ \begin{pmatrix} Q^T(t)R(t)Q(t) & Q^T(t)P(t) \\ P^T(t)Q(t) & S(t) \end{pmatrix} &\leq 0, \quad W(t) = W^T(t), \end{aligned}$$

where H_0 is a constant, symmetric matrix. The existence of a unique solution is obtained by the continuity of the described operators. For a splitting of hydrodynamic and thermal equations as performed in (3.27), it holds that $E = \mathbb{1}$, and P, K, S, N are zero in their corresponding dimensions. If additionally a time-independent energy matrix Q is assumed, the remaining properties for a pH formulation are, $t \in \tau$,

$$J(t), R(t) \in C^0(\tau, \mathbb{R}^{n \times n}), \quad (3.69a)$$

$$Q = Q^T, \quad R(t) = R^T(t), \quad J(t) = -J^T(t), \quad (3.69b)$$

$$Q^T R(t) Q \geq 0. \quad (3.69c)$$

The following theorem discusses one option to embed control system (3.27) into the port-Hamiltonian framework [59] and addresses the properties (3.69).

Theorem 11. *Let \bar{q} be a (spatially discretized) solenoidal volume-preserving time-continuous vector of volume flows. Then, the semi-discrete network model (3.27) can be embedded into a family of parameter-dependent port-Hamiltonian systems*

$$\frac{d}{dt}e = (J(\bar{q}) - R(\bar{q}))Qe + \tilde{B}(\bar{q})\tilde{u}, \quad \tilde{y} = \tilde{B}^T(\bar{q})Qe,$$

with $\tilde{u} = (u, 0, \dots, 0)^T \in \mathbb{R}^{1+2|C|}$ which contains the original outputs as subset. Here, Q is the energy matrix suggested in theorem 7.

Remark 12. *For the solenoidal transport of thermal energy and the quasi-stationary case of the momentum balance defined in section 3.1.5, theorem 7 states that there exists an energy matrix Q such that*

$$QA(\bar{q}) + A^T(\bar{q})Q \leq 0 \quad (3.70)$$

for all volume-preserving volume flow fields \bar{q} . Thus, the Hamiltonian $\mathcal{H}(e) = e^T Q e$ is a Lyapunov function for the parameter-dependent system [22].

Proof of Theorem 11. Let the positive definite diagonal matrix $Q \in \mathbb{R}^{n \times n}$ with

$$Q_{f_Z(\alpha, \beta), f_Z(\alpha, \beta)} = \Phi_\alpha h_\alpha > 0$$

be given. Then, the matrices J and R are defined by

$$J(\bar{q}) = \frac{1}{2}(A(\bar{q})Q^{-1} - (A(\bar{q})Q^{-1})^T), \quad R(\bar{q}) = -\frac{1}{2}(A(\bar{q})Q^{-1} + (A(\bar{q})Q^{-1})^T). \quad (3.71)$$

Note that the decomposition of a matrix M into a symmetric and a skew-symmetric part has a unique solution. Obviously, $A(\bar{q}) = (J(\bar{q}) - R(\bar{q}))Q$ holds. The properties $J = -J^T$ and $R = R^T$ of port-Hamiltonian system matrices are satisfied by construction. The time-continuity of the system operators $J(\bar{q}(t)), R(\bar{q}(t))$ is given since a time-continuous volume flow field is assumed. The positive semi-definiteness of R follows from the Lyapunov inequality (3.70). Consider now

$$M(\bar{q}) = QA(\bar{q}) + A^T(\bar{q})Q, \quad M_{f_Z(\alpha, \beta), f_Z(\alpha, \beta)}(\bar{q}) = -2Q_{f_Z(\alpha, \beta), f_Z(\alpha, \beta)} \frac{\bar{q}_\alpha}{h_\alpha} = -2q_\alpha \leq 0.$$

The volume-preservation of \bar{q} ensures that the symmetric matrix $M(\bar{q})$ is weakly diagonal dominant. Hence, $M(\bar{q})$ is negative semi-definite, yielding

$$x^T R(\bar{q})x = -\frac{1}{2}(Q^{-1}x)^T M(\bar{q}) (Q^{-1}x) \geq 0 \quad \text{for all } x \in \mathbb{R}^\kappa.$$

Here, $R(w)$ acts as a passivity matrix. The port matrix $\tilde{B}(\bar{q}) \in \mathbb{R}^{\kappa \times 1+2|\mathcal{C}|}$ defined by

$$\tilde{B}(\bar{q}) = [B(\bar{q}), (CQ^{-1})^T]$$

ensures that the outputs of the network model are contained in the output set of the port-Hamiltonian system, i.e., $\tilde{B}^T(\bar{q})Q = [B^T(\bar{q})Q, C]^T$. Finally note that the parameter-dependent port-Hamiltonian system matrices $J(\bar{q})$, $R(\bar{q})$, and $\tilde{B}(\bar{q})$ are continuous in time due to the given time-regularity of the parameter \bar{q} . \square

The presented framework holds for the mentioned assumptions neglecting thermal losses to the pipeline environment and assuming the quasi-stationary limit for the hydrodynamic equations. A consistent description as a port-Hamiltonian system including any of the two neglected terms is a non-trivial task. To incorporate the cooling term, the port-Hamiltonian description has to be generalized, which is an active field of research [60, 61]. Including the temporal derivative of the velocity augments the set of differential variables entering the DAE. The resulting additional contribution in the Hamiltonian H has to fulfill passivity again. This task is non-trivial since the differential equation for the velocity contains a non-linear part by frictional losses in the turbulent regime. In addition, if absolute pressure levels are part of the state space variables, the index of DAE increases to two, which requires to perform a regularization, before applying the port-Hamiltonian description [58].

To illustrate the structure of J, R for the upwind discretization on district heating networks, an example for one pipeline in the flow network is provided. In this setup,

$$R = -\frac{A + A^T}{2} = \frac{-v}{2h} \begin{pmatrix} -2 & 1 & & \\ 1 & -2 & & \\ & & \ddots & \\ & & & 1 \\ & & & 1 & -2 \end{pmatrix},$$

$$J = \frac{A - A^T}{2} = \frac{v}{2h} \begin{pmatrix} & -1 & & \\ 1 & & \ddots & \\ & \ddots & & -1 \\ & & & 1 \end{pmatrix}.$$

The numerical diffusion introduced by the upwind scheme expresses in the port-Hamiltonian setting in the non-vanishing R matrix.

3.9 Conclusions

In this chapter, an upwind scheme was used to discretize the solenoidal advection dominated transport of energy density. In the friction dominated regime, the momentum balance reduces to an algebraic constraint. Together with the power balance at consumer stations and the conservation of volume, it forms an algebraic system defining the velocity field for a given vector of energy densities. The resulting DAE is Lyapunov stable for arbitrary network topologies. By suggesting an energy matrix Q serving as the Kernel of the corresponding Lyapunov function, the DAE was embedded into the port-Hamiltonian framework. In addition, networks with nonzero velocity fields excluding circular flow configurations were proven to be asymptotically stable. Similarly, for networks without cycles in the flow- and the return part, existence and uniqueness of solutions was proved, given that the input energy density and the consumption signals are continuous in time. In the friction dominated limit neglecting the contribution of acceleration in the momentum balance, the differentiation index of the DAE reduces to 1. A system formulation was established in the form of a linear time varying system in the energy densities, in which the velocity field acts as a time varying parameter generated by algebraic constraints. This description provides the basis for model order reduction techniques discussed in the following chapter.

Chapter 4

Model order reduction for district heating networks

Model order reduction aims at approximating the input output relation of a dynamical system using a surrogate model which is computationally less complex to evaluate [22]. To this end, the original state space $\mathcal{X} \subset \mathbb{R}^n$ is reduced to a subspace $\mathcal{X}_r \subset \mathbb{R}^r$ of smaller dimension, $r \ll n$. In this chapter, a reduced order model is developed, describing the dynamical transport of the energy density in district heating networks based on the DAE (3.27) analyzed in chapter 3. Using the upwind discretization, a solenoidal model for the incompressible Euler-like equations with a stationary momentum equation leads to system (3.27), which is rewritten below for readability,

$$\dot{e} = A(q)e + B(q)u_T, \quad e(t_0) = e_0 \quad (4.1a)$$

$$y = Ce, \quad (4.1b)$$

$$0 = g(e, q, p, \Gamma). \quad (4.1c)$$

Eq. (4.1) is an index-1 DAE with state variables volume flow q , energy density e , and pressure p . From the perspective of system theory, different classifications of (4.1) are valid. Considering the entire state space to be $x = (e, q, p)^T$, and assuming that the velocity field has fixed directions, it can be written as a quadratic, bilinear system, referring to a product of state space variables due to the advective transport and a bilinear contribution by the product of volume flow and thermal input u_T . A detailed discussion of quadratic bilinear systems is performed below. An alternative interpretation is a linear-time varying system in the vector of energy densities e , where the algebraic equations g act as generators for the trajectory of the volume flow field. This interpretation will form the basis for the developed reduced order model, in which the transport of energy (4.1a) is reduced with the volume flow acting as a time-varying parameter.

The computational cost of solving a task using reduced order models splits in two phases. First, an offline-phase, in which the reduced order model is generated based on training data. Second, an online-phase in which the generated reduced order model is used to simulate or solve the problem in question. In the case of heating networks, the reduced order model depends on the topology and the boundary conditions which can be expected. After its determination, it can be reused for an identical topology

with different boundary conditions. Thus, the time to determine the surrogate model is not considered within this thesis, and we alternatively aim at minimizing the online time.

Reduction of energy networks

Concerning the reduction of energy networks, in [26] a linear model of the dynamics in gas networks is discussed, formulated in the state variables pressure and mass flow. After proving that the presented transport dynamics are port-Hamiltonian, a projection to a reduced order model is derived, originating from Krylov subspace methods. In the reduction of electrical circuits, [62, 63] mostly linear dynamics are considered. A central difficulty arises from the large number of input- and output channels with is solved using clustering techniques. Concerning the reduction of heating networks, selected works are discussed briefly. In [13], a linear model for the hydrodynamic equations in the state variables pressure and mass flow is derived. Subsequently it is reduced using radial basis functions. The thermal transport of energy is not considered. In [28], pipeline classes are identified. For each class, specific forms of transfer functions are matched to simulation results. The resulting reduced pipeline models are concatenated. The output of the preceding pipeline acts as input to the following pipeline. This strategy yields two disadvantages. First, by approximating each pipeline with an own reduced model, the approximation error in the output of a given pipeline will amplify with each pipeline. Second, the computational saving of reducing a single pipeline element is potentially small compared to its full order description. Other publications do not pursue a system theoretic reduction approach but truncate analytical solutions of the transport equation [11] or assume constant transport time delays from source to consumption [12] to obtain a simplified model of the energy transport in the network. In this thesis, an approach close to concepts from system theory is proposed, based on the underlying Euler equations. Subsequently different approaches for model order reduction of dynamical systems are discussed and evaluated for the applicability to the dynamics of heating networks (4.1).

4.1 Reduction by projection

Many tools from model reduction can be formulated as a projection from a high-dimensional space \mathcal{X} to a subspace \mathcal{X}_r . The properties of the resulting reduced order models mainly differ by the method used to compute the projection. As a start, a generic nonlinear system is considered

$$\dot{x}(t) = f(x(t), u(t)), \quad x(t_0) = x_0, \quad (4.2a)$$

$$y(t) = J(x(t), u(t)), \quad (4.2b)$$

where $u : \mathcal{T} \rightarrow \mathbb{R}^{|u|}$ is the input to the dynamical system, $f : \mathbb{R}^n \times \mathbb{R}^{|u|} \rightarrow \mathbb{R}^n$ defines the ODE shaping the dynamics and $J : \mathbb{R}^n \times \mathbb{R}^{|u|} \rightarrow \mathbb{R}^{|y|}$ is the function measuring

the relevant output $y \in \mathbb{R}^{|y|}$. Using the projection $\Pi = VW^*$, where $V, W \in \mathbb{R}^{n \times r}$ denote orthogonal matrices with $W^*V = \mathbb{1}$, the reduced order system resulting from (4.2) reads

$$\dot{x}_r(t) = W^*f(Vx_r(t), u(t)), \quad (4.3a)$$

$$y_r(t) = J(Vx_r(t), u(t)). \quad (4.3b)$$

The projection Π is of Petrov-Galerkin type, if $W \neq V$ and of Galerkin type, if $W = V$ [22]. In addition, M^* denotes the complex conjugate transpose of a matrix M . A common problem for nonlinear reduced order models lies in the evaluation of the nonlinear function f . In its general form, it requires to project the reduced order state to the full vector of dimension n , evaluate the n dimensional function f and project it back to the subspace \mathcal{X}_r . The transition between full and reduced order spaces has to be performed in each evaluation of (4.3), prohibiting a decrease in computational complexity. To overcome this difficulty, the discrete empirical interpolation method was introduced [64]. Based on empirical data, the function f is approximated by interpolation of discrete points. If f in contrast exhibits a structure or is close to linearity, different techniques can be used for reduction as discussed below.

Structure preserving reduction

Structure preserving reduction denotes methods in which the reduced order model preserves certain properties of the full order model. These properties can refer to stability of the dynamical system, the interpretation as e.g. a network structure [65, 66] or passivity. For linear port-Hamiltonian systems

$$\dot{x} = (J - R)Qx + Bu \quad (4.4a)$$

$$y = Cx + Du, \quad (4.4b)$$

it can be shown that including Q in the projection preserves the port-Hamiltonian property [67, 68, 69, 70, 71, 57]. Specifically, based on a projection matrix $\tilde{V} \in \mathbb{R}^{n \times n}$, the preserving Petrov-Galerkin projection is defined by

$$\tilde{V}^T Q \tilde{V} = \zeta^T \zeta, \quad (4.5a)$$

$$V = \tilde{V} \zeta^{-1}, \quad (4.5b)$$

$$W = QV, \quad (4.5c)$$

where ζ is the Cholesky decomposition of $\tilde{V}^T Q \tilde{V}$. It is well-defined since Q is positive definite for the suggestion in theorem 7. For a fixed energy matrix Q , (4.5) is a one-sided (Galerkin) projection by construction. Since Q is not unique, additional options occur for V, W based on a given projection \tilde{V} . As discussed in section 3.6, the solution to the Lyapunov inequality is, considering general topologies of heating networks, not unique. As an alternative to the projection (4.5), a state space transformation of (4.4) can be performed, in which $Q = \mathbb{1}$. The transformed port-Hamiltonian system can then be reduced by arbitrary Galerkin projections.

A similar result can be obtained for system (4.1). In particular, applying the projection (4.5) to (4.1) results in

$$\dot{e}_r = W^* A(q) V e_r + W^* B(q) u_T, \quad (4.6a)$$

$$y_r = C V e_r, \quad (4.6b)$$

$$0 = g(e_r, q, p, \Gamma). \quad (4.6c)$$

Inserting the reduced order system operator in the Lyapunov inequality leads to (4.5)

$$(W^* A(\omega) V)^* + W^* A(\omega) V = V^* (Q^* A(\omega) + A^*(\omega) Q) V. \quad (4.7)$$

Consequently, (4.7) is negative semi-definite, if the full order Lyapunov inequality is fulfilled. Stability is still coupled to the claim that $A(\omega)$ is formed by a velocity vector ω satisfying volume conservation.

An additional preservation property for system (4.1) following from projection based reduction addresses the affine decomposition of the system operators discussed in section 3.3. The projection matrices V, W are solely applied to the time-independent matrices, leading to

$$A_r(q) := W^* A(q) V = \sum_{\nu=1}^{n_q} \gamma_{\nu}^{\tilde{q}} W^* A_{\nu}^{\tilde{q}} V, \quad B_r(\tilde{q}) = \sum_{\nu=1}^{n_q} \gamma_{\nu}^{\tilde{q}} W^* B_{\nu}^{\tilde{q}}, \quad (4.8a)$$

$$C_r = C V. \quad (4.8b)$$

In (4.6) the time-independent matrices can be reduced in the offline-phase. Thus, the time-dependent reduced order operators are recalculated entirely in the reduced subspace. For a fixed volume flow field, (4.1) defines a linear system in the energy densities. Consequently, (4.6) preserves both the affine decomposition and the Lyapunov stability of the full order system for arbitrary Galerkin projections \tilde{V} transformed by (4.5). In (4.8) any affine decomposition is preserved by projection by definition and can be reduced in the offline phase. Independent volume flows were chosen as an example representation, since this representation yields a small number of parameters and thus necessary summations, and is used in the numerical analysis presented in chapter 5.

4.2 Reduction of linear time varying systems

Hereafter two different strategies for the generation of Galerkin projections for the linear time varying system (4.1) are discussed.

4.2.1 Proper orthogonal decomposition

Proper orthogonal decomposition (POD) [72, 73, 74] aims at approximating a snapshot matrix $Z \in \mathbb{R}^{n \times m}$

$$Z = [z(t_1), \dots, z(t_m)] = \left[\begin{pmatrix} z_1(t_1) \\ \vdots \\ z_n(t_1) \end{pmatrix}, \dots, \begin{pmatrix} z_1(t_m) \\ \vdots \\ z_n(t_m) \end{pmatrix} \right] \in \mathbb{R}^{n \times m}, \quad (4.9)$$

by a set of $r < m$ basis functions $\hat{Z} = \{\hat{z}_i\}$, $\hat{z}_i \in \mathbb{R}^n$, $i \in [1, \dots, r]$. Here, n denotes the state space dimension and m the number of time samples taken from the dynamical process to be reduced. It shall be noted that POD approximates generic matrices Z . However, in this subsection the specific application is studied in which Z has the interpretation of a snapshot matrix. According to the Schmidt-Mirsky-Eckard result, [22], the best rank r approximation of Z in the induced 2 norm is given by

$$\min_{\text{rank}(\hat{Z}) \leq r} \|Z - \hat{Z}\|_2 = \|Z - U_r U_r^* Z\|_2. \quad (4.10)$$

The solution $U(:, 1:r) = U_r \in \mathbb{R}^{n \times r}$ of the minimization problem (4.10) is provided by the leading r left singular vectors of the snapshot matrix Z . These are a result of the singular value decomposition (SVD) defined by

$$Z = U \Sigma L^*, \quad (4.11)$$

for two orthogonal matrices $U, L \in \mathbb{R}^{n \times r}$. Hence, POD allows to extract a r -dimensional subspace in which a dynamical system evolves. The corresponding reduced order system is obtained by Galerkin projection using the projection matrix U_r .

Reduced basis methods [75, 76] aim at deriving a reduced base for the state space which optimally approximates the outputs of a dynamical systems for the relevant input signals. These methods often approximate the input-to-state map making use of the proper orthogonal decomposition (POD) technique. The latter bases on snapshots of the system state for time-domain simulations to generate a low dimensional subspace in which the relevant dynamics evolve. For advection dominated phenomena, it is known that the singular value decay of the corresponding snapshots is slow, resulting in large surrogate models [19]. In fig. 4.1 an example is visualized in which a Gaussian is transported in space. For a given location in space, it can be described by a single reduced order mode. However, due to its constant relocation by advection, a new reduced order mode is required for every time, explaining the high number of reduced order modes. Different approaches were proposed to overcome this problem by shifting the transport dynamics to a time-invariant reference frame using the velocity information of the flow field [19, 77, 21, 78]. While these methods achieve good approximations for the presented examples, the case of a large network poses severe difficulties. For a network setup, a wave front entering a node with three coupling edges splits up into two wave fronts with a modified distribution. Thus, the relevant information can not be described by a mode valid for the original mode and the

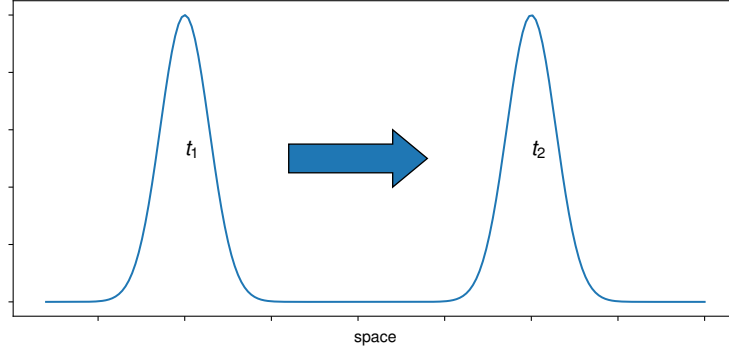


Figure 4.1: Transport of a Gaussian impulse along space.

reduced basis has to be enriched. Conversely, this also holds for two wave fronts interfering at a junction. Since in a large scale network there usually exist many nontrivial nodes, tracking the wave fronts is prohibitively complex. Other techniques calculate a dictionary of solutions for the relevant dynamics in the offline phase and weight them to obtain a minimal L_1 error [79].

4.2.2 Model reduction by interpolation

For the context of energy networks, it suffices to capture the relevant outputs at distinct points in the network. In particular, the energy densities at the consumer stations are a necessary input for the power balance defining the local volume flow. As a consequence, we aim at reproducing the input to output behavior of the system based on the properties of its transfer function. To illustrate the concept of moment matching, the following linear system is considered,

$$E\dot{x} = Ax + Bu, \quad x(t_0) = x_0, \quad (4.12a)$$

$$y = Cx + Du. \quad (4.12b)$$

Subsequently, the linear descriptor system (4.12) shall be characterized in the frequency domain. To this end, a Laplace transform is applied to (4.12) resulting in

$$\mathcal{L}_{y(t)}(s) = C(sE - A)^{-1}Ex_0 + [C(sE - A)^{-1}B + D]\mathcal{L}_{u(t)}(s), \quad (4.13)$$

where $\mathcal{L}_{f(t)}(s)$ denotes the Laplace transform of a function f . Eq. (4.13) exhibits two contributions. One stemming from the initial state x_0 and one dynamical contribution from the input u driving the system. The relation between the Laplace transforms of input u and output signal y of a linear dynamical system is provided by the transfer function $H(s)$,

$$H(s) = C(sE - A)^{-1}B + D. \quad (4.14)$$

With common abuse of notation, the Hamiltonian and the transfer function of a linear system are both abbreviated by the symbol H . Concerning the reduction of a

linear dynamical system by projection, important relations exist between the transfer function of the full and the reduced order system. First, for multiple input, multiple output (MIMO) linear systems it is straight forward to show [22, 44] that

$$\|y\|_{\mathcal{L}_\infty} \leq \|H\|_{\mathcal{H}_2} \|u\|_{\mathcal{L}_2}. \quad (4.15)$$

According to (4.15), the infinity norm of the output is bounded by the product of the \mathcal{H}_2 -norm of the transfer function and the \mathcal{L}_2 -norm of the input signal. This allows to relate the approximation error in the output to the approximation error in the transfer function of full and reduced order systems. Furthermore, altering the projection matrices V, W allows to define the connection of the full and the reduced order transfer functions [80] as follows. Assume interpolation points $\sigma, \mu \in \mathbb{C}$ s.t. the Kernels for the full and reduced order system $sE - A$, $sE_r - A_r$ are invertible for the frequencies $s = \sigma, \mu$, and let $b \in \mathbb{C}^m$, $c \in \mathbb{C}^l$ be fixed nontrivial direction vectors. Then the following holds,

$$\text{a) if } ((\sigma E - A)^{-1}E)^{j-1}(\sigma E - A)^{-1}Bb \in \text{Im}(V), \quad j = 1, \dots, N \quad (4.16a)$$

$$\text{then } H^l(\sigma)b = H_r^l(\sigma)b, \quad l = 0, \dots, N - 1 \quad (4.16b)$$

$$\text{b) if } ((\mu E - A)^{-T}E)^{j-1}C^T c(\mu E - A)^{-1} \in \text{Im}(W), \quad j = 1, \dots, M \quad (4.16c)$$

$$\text{then } c^T H^l(\mu) = c^T H_r^l(\mu), \quad l = 0, \dots, N - 1 \quad (4.16d)$$

$$\text{c) if } \text{a) and b) hold, and } \sigma = \mu \quad (4.16e)$$

$$\text{then } c^T H^l(\mu)b = c^T H_r^l(\mu)b, \quad l = 0, \dots, M + N - 1, \quad (4.16f)$$

where H^l , $l \in \mathbb{N}$ is the l -th moment of the transfer function. Hence, if the presented vectors are within the range of the projection matrices V, W , the reduced transfer function H_r interpolates the full order transfer function H at distinct frequencies. To determine the points in frequency space at which the transfer full transfer function should be evaluated, the iterative rational Krylov approximation (IRKA) algorithm was suggested [81]. It relies on the assumption that $H(s)$ shall be interpolated at the mirror images of the eigenvalues of the reduced order model. To determine those, a fixed-point iteration is initialized. Although IRKA has no convergence guarantees for non-symmetric linear systems, it proved to be useful in different applications. It can be shown that a first order interpolation using (4.16) yields necessary optimality conditions for the deviation of full and reduced order model in the \mathcal{H}_2 -norm. The \mathcal{H}_2 -norm is defined by [22]

$$\|H\|_{\mathcal{H}_2}^2 = \frac{1}{2\pi} \sup_{x>0} \int_{-\infty}^{\infty} \|H(x + iy)\|_F^2 dy,$$

where $\|\cdot\|_F$ is the Frobenius norm of a matrix, $\|M\|_F = \sqrt{\text{trace}(M^*M)}$.

In contrast to approximating the state space, the transfer function of the dynamical system is approximated. In the latter case, the input-output behavior of the system is considered, which depending on the problem in question, can be of much lower dimension than the relevant state space. Reconsidering the transport of a local peak information, the advection velocity is constant in time as long as the boundary condition at the end of the pipeline remains unchanged. The corresponding linear system remains constant in time, as well.

4.2.3 Parametric model order reduction

Different works address the problem of parameterized model order reduction [82, 83, 44]. Typically, linear parameterized systems are considered, in which the system operators carry an affine relation to the parameter vector $p \in \Omega \subset \mathbb{R}^d$,

$$E(p)\dot{x} = A(p)x + B(p)u, \quad x(t_0, p) = 0, \quad (4.17)$$

$$y = C(p)x. \quad (4.18)$$

The aim is to construct a reduced order model, based on which the transfer function of full and reduced order model show a small deviation with respect to the norm

$$\|H - H_r\|_{\mathcal{H}_2 \otimes \mathcal{L}_2(\Omega)}^2 = \frac{1}{2\pi} \int_{-\infty}^{\infty} \int_{\Omega} \|H(i\omega, p) - H_r(i\omega, p)\|_F^2 dp_1 \dots dp_d d\omega. \quad (4.19)$$

Eq. (4.19) is a joint norm in both the frequency space and the domain Ω of the parameter vector p . The parameterized transfer function is defined in agreement to the purely linear case

$$H(s, p) = C(p)(sE(p) - A(p))^{-1}B(p). \quad (4.20)$$

Eq. (4.20) does indeed correspond to the transfer function of the dynamical system, since the parameter vector $p \in \Omega$ is constant in time. While (4.17) is structurally similar to (4.1), where q takes the role of the parameter vector, the volume flow changes dynamically within the simulation. Still, approximating the linear function formed by a fixed volume flow q , leads to a reduced order model which approximates the local linearization of the full, dynamical model. Consequently, including suitable linearizations at selected volume flows in a global projection will form a reduced order model which approximates the dynamical, full order model. On this account, ideas from parameterized model order reduction concerning the combination of local approximations are still promising for the case of time varying parameters.

4.3 Transfer function on a single pipeline

To characterize the transfer function for the transport dynamics, the advection of the internal energy density on one pipeline is considered for times $t \in \mathcal{T}$

$$\partial_t e = -v\partial_x e, \quad e(t, 0) = u_T(t), \quad e(t_0, x) = e_0, \quad x \in [0, L]. \quad (4.21)$$

For the following considerations, the velocity v is assumed to be time-independent. Under this assumption, the energy density at the pipeline end $x = L$ and time t is given by

$$y(t) = e(t, L) = e\left(t - \frac{L}{v}, 0\right) = u_T(t - \tau), \quad (4.22)$$

where u_T is the boundary function supplied at the inflow boundary and $\tau = L/v$ is the ratio of pipeline length and velocity. Finally, y denotes the observable of interest. Applying the Laplace transformation to (4.22)

$$\mathcal{L}_y(s) = \mathcal{L}_{u_T(t-\tau)}(s) = \int_0^\infty \exp(-st) u_T(t-\tau) dt = \exp(-\tau s) \mathcal{L}_{u_T}(s),$$

results in the transfer function $H(s) = \exp(-\tau s)$ with the absolute value $|H(s)| = 1$. It is easy to verify that $\|H(s)\|_{\mathcal{H}_2} = \infty$ and thus $H(s)$ is not member of the \mathcal{H}_2 Hardy space.

Transfer function resulting from the upwind scheme

The analytical result of the transfer function is compared to the transfer function resulting from the upwind scheme. For one pipeline with $n \in \mathbb{N}$ finite volume cells, the transport process is written as

$$\dot{e}_1 = -\tau^{-1} n (e_1 - u_T) \quad (4.23)$$

$$\dot{e}_i = -\tau^{-1} n (e_i - e_{i-1}), \quad i \in [2, \dots, n], \quad (4.24)$$

where $\tau^{-1} = \frac{v}{L}$ with constant velocity v . Still, the energy density $e(t, L)$ at $x = L$ is the relevant output. For the upwind scheme, it is approximated by $y = e_n$. The corresponding system formulation for one pipeline reads

$$\dot{e} = -(\tau^{-1} \cdot n) G e + B u_T \quad (4.25a)$$

$$y = C e. \quad (4.25b)$$

Here $B = (\tau^{-1} \cdot n_T, \dots, 0)^T$, $C = (0, \dots, 1)$ are the input and output operators, and G is the velocity independent stencil resulting from the upwind scheme of first order. The transfer function referring to (4.25) is given by

$$H(s) = C \begin{pmatrix} -\tau^{-1} \cdot n + s & 0 & 0 \\ \tau^{-1} \cdot n & -\tau^{-1} \cdot n + s & 0 \\ 0 & \tau^{-1} \cdot n & -\tau^{-1} \cdot n + s \\ & & \ddots \end{pmatrix}^{-1} B \quad (4.26a)$$

$$= \frac{(\tau^{-1} \cdot n)^{n-1}}{(s + \tau^{-1} \cdot n)^n} \tau^{-1} \cdot n \quad (4.26b)$$

$$= \left(\frac{\tau^{-1} \cdot n}{s + \tau^{-1} \cdot n} \right)^n. \quad (4.26c)$$

In the limit of infinitely many finite volume cells, (4.26) converges to the analytical result, $\lim_{n \rightarrow \infty} H(s) = \exp(-\tau s)$. The discretized transfer function has a pole of order n at $s = -\tau^{-1} \cdot n$. The modulus of (4.26) reads

$$|H(s)| = \frac{(\tau^{-1} \cdot n)^n}{(s^2 + \tau^{-2} n^2)^{n/2}}, \quad (4.27)$$

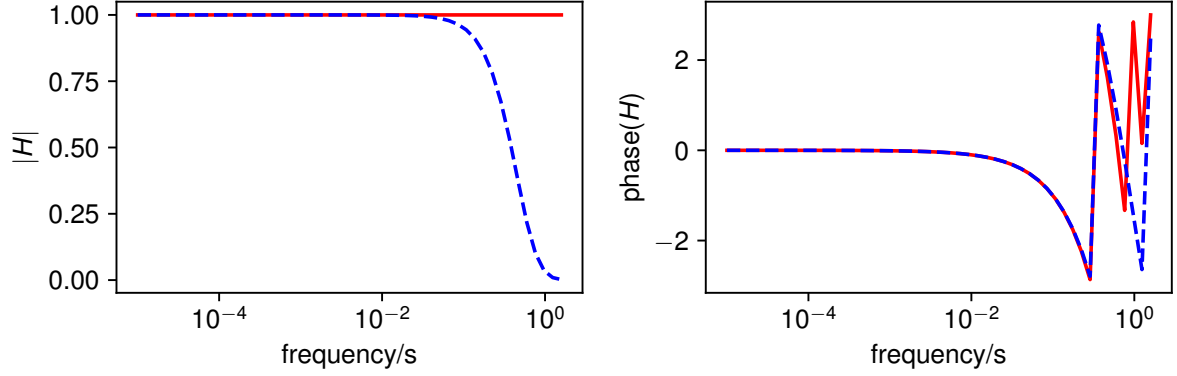


Figure 4.2: Bode plot of the transfer function H for one pipeline with fixed velocity comparing the PDE solution (red, solid) to the numerical approximation using the upwind scheme (blue, dashed).

which approaches 1 for $n \rightarrow \infty$. The transfer function shows the numerical diffusion introduced by the upwind scheme. It holds that $|H(s)| < 1$, $\forall s \in \mathbb{R} \setminus \{0\}$. Hence, any output signal will exhibit a loss in modulus compared to the original input signal. For a given frequency s of an input signal with a sinusoidal component, the loss in modulus amplifies with an increasing time delay τ between start and end of the pipeline. Next, the \mathcal{H}_2 norm of the ODE system shall be evaluated. This leads to

$$\begin{aligned} \|H\|_{\mathcal{H}_2}^2 &= \sup_{x>0} \left[\int_{-\infty}^{\infty} |H(x + iy)|^2 dy \right] \\ &= \sup_{x>0} \left[(\tau^{-1}n)^{2n} \int_{-\infty}^{\infty} \frac{1}{((x + \tau^{-1}n)^2 + y^2)^n} dy \right] \\ &\leq \sup_{x>0} \left[(\tau^{-1}n)^{2n} \int_{-\infty}^{\infty} \frac{1}{((x + \tau^{-1}n)^2 + y^2)^1} dy \right] \\ &= \sup_{x>0} \left[(\tau^{-1}n)^{2n} \frac{\pi}{|x + \tau^{-1}n|} \right] = \pi(\tau^{-1}n)^{2n-1}. \end{aligned}$$

As a result, the transfer function (4.26) for one pipeline resulting from the upwind scheme is element of the \mathcal{H}_2 space, in contrast to its PDE equivalent. A Bode plot of the transfer function resulting from the PDE description and the numerical approximation using the upwind scheme is visualized in fig. 4.2. It shows the absolute value $|H(i\omega)|$ and the phase $\arg(H(i\omega))$ for real frequencies ω evaluated at the imaginary axis. The chosen time delay is given by $\tau = L/v = 10$ s. The numerical scheme is approximated using $n = 10$ cells. As derived above, the transfer function resulting from the dynamics at the PDE level carries a constant absolute value of 1, while the phase is proportional to the frequency, $\arg(\exp(-is\tau)) = -s\tau$. The oscillations in the phase result from the logarithmic scaling of the abscissa in combination with resifting the angle to the standard domain $\pm\pi$. The numerical approximation agrees with the PDE results up to a frequency of at least 10^{-2} , until the absolute value of the numerical approximation converges to 0. The phase is approximated to even higher frequencies.

4.4 Further reduction approaches

In addition to the reduction approaches mentioned so far, a variety of other methods exist [84]. Data driven methods [85, 86] produce a minimal system description of a dynamical process, solely based on measurements of the transfer functions. Furthermore, connections of model order reduction and deep learning are addressed intensively recently [87, 88, 20]. Dynamic mode decomposition (DMD)[89], and its extension to control systems (DMDc) [90], aim at approximating a (non-)linear dynamical system by a linear, time invariant system of reduced dimension. In contrast to projection based reductions, the resulting linear operator A_r is constructed by the identified modes and thus is constant in time for the later simulation. For the dynamics of district heating networks, the time-independent volume flows at consumer stations induce qualitatively different linearizations, which is why DMD is not promising for this particular application. Subsequently, two reduction techniques for nonlinear systems are discussed in more detail due to their strong connection to the dynamics of heating networks.

Quadratic-bilinear differential algebraic equations

Quadratic-bilinear differential algebraic equations (QBDAEs) [91, 92, 93, 94] denote the following class of systems

$$E\dot{x}(t) = Ax(t) + M(x(t) \otimes x(t)) + \sum_{k=1}^{|u|} N_k x(t) u_k(t) + Bu(t) \quad (4.28)$$

$$y = Cx(t), \quad x_0 = 0, \quad (4.29)$$

where $M \in \mathbb{R}^{N \times N^2}$, $A \in \mathbb{R}^{N \times N}$, $N_k \in \mathbb{R}^{1 \times N}$ $k \in [1, \dots, |u|]$, $B \in \mathbb{R}^{N \times |u|}$, $C \in \mathbb{R}^{|y| \times N}$, and \otimes denotes the Kronecker product. By defining the state space variables as $x = (e, v, p)^T$ and posing additional assumptions, (4.1a) can be written in the form (4.28). First, density and friction factor are constants. Second, the direction of each component of the velocity vector has to be constant, which can be either ensured by the correct input signal or by the network topology. Third, the network topology only includes junctions with $l \in \mathbb{N}$ inflowing pipelines and one outflowing pipeline or vice versa. The first assumption ensures that the Euler momentum balance carries $v|v|$ as the highest nonlinearity. The second assumption removes the absolute value from the velocity vector, since its direction is static component wise. The last assumption ensures that each energy density can be written as a linear combination of products of velocities and energy densities. It shall be noted that these assumptions are sufficient for a description as a QBDAEs but potentially not necessary. For specific types of nonlinearities, introducing additional virtual state variables allows to formulate a QBDAE. As a drawback, this increases the state space dimension in contrast to the aim of model order reduction. This is in line with the findings in [91] where a simplified version of the Navier-Stokes equation is considered on a simple domain.

Concerning the reduction of (4.28), the authors suggest to use a projection based interpolation of generalized transfer functions. The central drawback in the reduction of district heating networks formulated as QBDAEs arises from the possible elimination of algebraic equations corresponding to the conservation of volume and energy over network nodes. Thus, there are no guarantees for obtaining a Lyapunov stable reduced order model.

Trajectory piecewise linear

Trajectory piecewise linear (TPWL) approaches [95, 96] linearize a nonlinear DAE at selected points in state space and interpolate the linearizations to approximate the nonlinear model. Specifically, the nonlinear state space description

$$E\dot{x} = f(x) + \tilde{B}(x)u, \quad (4.30a)$$

$$y = Cx, \quad (4.30b)$$

is described by $s \in \mathbb{N}$ linearizations

$$E\dot{x} = \sum_{i=1}^s w_i(x_i)[f(x_i) + \tilde{A}_i(x - x_i) + \tilde{B}_i u]. \quad (4.31a)$$

$$y = Cx. \quad (4.31b)$$

The nonlinear function f is approximated to first order using a Taylor expansion with $\tilde{A}_i = df/dx(x_i)$. The state dependent input matrix is approximated by a constant, $\tilde{B}_i = \tilde{B}(x_i)$. The quantities w_i , $i \in [1, \dots, s]$ represent weighting functions for the chosen linearizations. To derive a reduced order model for (4.30), the authors [95, 96] suggest to calculate local Krylov subspaces for each linearization and combine them using a SVD. Applying approximation (4.31) to the description of heating networks, a linearization with respect to different state variables is possible. First, considering $x = (e, q)^T$ as the vector of state variables, the linearization of (4.1) also requires to linearize algebraic equations g defining the flow field. This might introduce undesired instabilities even for the full order model. Second, considering only energy densities as state variables, $x = e$, preservation of stability for the linearized model is still only ensured for a specific choice of weights and additional assumptions to the nonlinearity [95]. For $x = e$, the energy transport (4.1a) is the ODE to be linearized with the nonlinearity $A(q)$, where the volume flow is a function of e by power conservation at consumers. Preservation of stability for reduced order TPWL models requires that the Jacobian of the nonlinearity evaluated at the possible equilibrium point \bar{x} has to be negative definite,

$$x^T \frac{dA(q)e}{dx}(\bar{x})x < 0, \quad x \in \mathcal{X}.$$

Applying this to (4.1a) where $x = e$, and \bar{e} denotes the vector of energy densities leading to an equilibrium state,

$$\frac{dA(q)e}{de}(\bar{e}) = A(\bar{q}) + \frac{dA(q)\bar{e}}{de}. \quad (4.32)$$

The second contribution stemming from the derivative of the volume flow field with respect to the energy densities adds additional off diagonal terms to $A(\bar{q})$ destabilizing the system dynamics. To illustrate this, the example of a single pipeline in the flow network attached to a single consumer is considered. The additional contribution then reads

$$\frac{dA(q)\bar{e}}{de} = \frac{1}{\Phi h} \begin{pmatrix} 0 & \dots & -q'\bar{e}_1 \\ \vdots & \dots & -q'(\bar{e}_2 - \bar{e}_1) \\ 0 & \dots & -q'(\bar{e}_n - \bar{e}_{n-1}) \end{pmatrix}. \quad (4.33)$$

Here, q' refers to the derivative of the volume flow at consumer stations with respect to the contributing energy density e_n ,

$$q'(e_n) = \frac{d}{ds} \frac{G}{s - e_R}(e_n) = \frac{-q}{e_n - e_R}.$$

For a single pipeline, the equilibrium state is given by $\bar{e}_i = \bar{u}$, $i \in [1, \dots, n]$. Inserting this to (4.32) yields

$$\frac{dA(q)e}{de}(\bar{e}) = \frac{1}{\Phi h} \begin{pmatrix} -q & & -q'e_1 \\ q & \ddots & \\ & q & -q \end{pmatrix} = \frac{q}{\Phi h} \begin{pmatrix} -1 & & \frac{\bar{u}}{\bar{u} - e_R} \\ 1 & \ddots & \\ & 1 & -1 \end{pmatrix}. \quad (4.34)$$

For a sufficiently large ratio of $\bar{u}/(\bar{u} - e_R)$, the matrix (4.34) is indefinite.

Remark 13. *It shall be noted, that the system operator $A(q)$ for general network topologies is not even negative semi-definite. To overcome this, the system description can be transformed to scaled energy coordinates E , resulting in a scaled system operator A^E which is guaranteed to be negative semi-definite. However, for a single pipeline, already $A(q)$ is negative semi-definite and the above chain of arguments applies, showing that linearization introduces instabilities for the dynamics of heating networks.*

4.5 Generation of suitable Galerkin projections

We seek to construct a global, stable, surrogate model of the quadratic in state index-1 DAE (4.1), which, after offline generation, can be reused for all admissible inputs $u \in \mathcal{U}_T$. Consequently, the time to generate the surrogate model is not considered. Note that the surrogate model is generated for the ODE system (4.1a) with a given number of finite volume cells, and not for the PDE system itself. The reduction presented subsequently bases on local linearizations of (4.1) at fixed volume flow fields. Consequently, the momentum balance defining the flow field can also include the acceleration contribution for the suggested strategy. In contrast, thermal losses due to an imperfect isolation of pipelines are a nonlinear contribution to the transport of energy density and are thus not in the scope of the presented algorithm. The information necessary to construct the surrogate model is the set of admissible controls

$\mathcal{U}_{\mathcal{T}}$, the expected consumption G , and the topology of the network represented by the graph \mathcal{G} . The admissible input signals are defined by technical restrictions and are summarized in the following space

$$\mathcal{U}_{\mathcal{T}} = \{u(t) = c_0 + \sum_{i=1}^m c_i \cos(i\omega t + \beta_i), m\omega \leq \hat{\omega}, |\dot{u}(t)| \leq u_d, u(t) \in [u_l, u_h] \forall t \in \mathcal{T}\}. \quad (4.35)$$

The control $u \in \mathcal{U}_{\mathcal{T}}$ is periodic with maximal contributing frequency $\hat{\omega}$, its absolute temporal derivative is bounded by u_d , and its image varies within the interval $[u_l, u_h]$.

In this section we focus on the generation of a Galerkin projection $V \in \mathbb{R}^{n \times r}$, which forms the desired surrogate model for the DAE system (4.1). As shown in [69, 67, 68], a Lyapunov stable system can be transformed to scaled co-energy coordinates, $E = \zeta^{-1}e$, where $\zeta^T Q \zeta = \mathbb{1}$, to obtain a representation in which $Q^E = \mathbb{1}$,

$$\begin{aligned} \dot{E} &= A^E(q)E + B^E(q)u_T(t) \\ y &= C^E E. \end{aligned} \quad (4.36)$$

One easily checks that $A^E + (A^E)^T = \zeta^T(QA + A^T Q)\zeta \leq 0$ itself fulfills the Lyapunov inequality. Hence, every Galerkin projection V applied to (4.36) produces a globally stable ROM ($V^T(A^E + (A^E)^T)V \leq 0$), without the need to imply Q in the reduction process. As shown in theorem 7, Q is diagonal and thus $\zeta = \text{diag}(Q_{11}^{-1/2}, \dots, Q_{nn}^{-1/2})$. The reduced order model resulting from an arbitrary Galerkin projection is given by

$$\begin{aligned} \dot{E}^r &= V^T A^E(q) V e^r + V^T B^E(q) u_T(t), \\ y^r &= C^E V E^r \\ 0 &= g(y^r, q, p, \Gamma). \end{aligned} \quad (4.37)$$

Thus we seek a global subspace in which the relevant dynamics of the nonlinear system (3.27) evolve, ensuring $y^r \approx y$, $u_T \in \mathcal{U}_{\mathcal{T}}$. Similar to the ideas discussed for parameterized systems in [83, 44], we focus on the reduction of the linear time varying problem (LTV) (4.36), which splits in two sub-tasks. The first is the choice of a scheme for the reduction of a locally linear system. The second task includes picking a robust set of linearizations, which enter the dynamical surrogate model. To discuss the first task of reducing linear systems, a measure for the approximation quality of the ROM to a linear model has to be defined. To this end, we use a weighted \mathcal{H}_2 -norm over the relevant frequency range $W \subset \mathbb{R}^+$ [97],

$$\|H\|_{\mathcal{H}_2(W)}^2 = \frac{1}{2\pi} \int_W \|H(i\omega, q)\|_F^2 d\omega, \quad (4.38)$$

where we define the transfer function as a parametric function, cf. (4.20). The parameter vector is given by the vector of volume flows. The interval of admissible frequencies $W = [W_l, W_h]$ is chosen close to the maximal frequency $W_h \approx \hat{\omega}$, and a minimal frequency W_l at which the transfer function converges. Consequently, we use a modified version of the iterative rational Krylov approximation (IRKA) [81] for the generation

Algorithm 2 Weighted IRKA

Require: error bound $\bar{\delta}$, system matrices A^E, B^E, C^E , initial interpolation frequencies $\sigma = \{\sigma_1, \dots, \sigma_r\}$, iteration limit N

Ensure: local Galerkin projection V

- 1: **while** $\varepsilon \geq \bar{\delta}$ **do**
- 2: initialize b_j by most dominant singular vector of $H(\sigma_j)$, $j \in [1..r]$
- 3: **for** $i=1$ to N **do**
- 4: $R(\sigma, b) = [(\sigma_1 \mathbb{1} - A^E)^{-1} B^E b_1, \dots, (\sigma_r \mathbb{1} - A^E)^{-1} B^E b_r]$
- 5: $V = \text{orth}\{\text{Im}(R(\sigma, b)), \text{Real}(R(\sigma, b))\}$
- 6: $\tilde{A} \leftarrow V^T A^E V$, $\tilde{B} \leftarrow V^T B^E$, $\tilde{C} \leftarrow C^E V$
- 7: determine error $\varepsilon_i = \delta_q(H, \tilde{H})$ cf. (4.39) of current ROM $\tilde{H} = \tilde{H}(\tilde{A}, \tilde{B}, \tilde{C})$
- 8: determine eigenvalues and left eigenvectors, $y_i^* \tilde{A} = \lambda_i y_i^*$
- 9: update $\sigma_i \leftarrow -\lambda_i$, and $b_i^T \leftarrow y_i^* \tilde{B}$
- 10: perform additional residue correction according to [99]
- 11: **end for**
- 12: $\varepsilon = \min_{i \in [1..N]} \varepsilon_i$
- 13: increase number of interpolation points σ
- 14: **end while**
- 15: **return** V

of the local reduction. In its original form, IRKA fulfills necessary conditions for a \mathcal{H}_2 optimal interpolation of the full transfer function of the system. Based on initial interpolation points σ and directions b, c in the frequency space, it uses a fixed point iteration to ensure that the reduced model interpolates the transfer function H at the mirror images of the reduced poles. Since we address a weighted error norm, convergence of the interpolation points does not fulfill necessary optimality conditions with respect to the modified norm $\|H\|_{\mathcal{H}_2(W)}^2$ [97, 98]. For this reason, we only perform $n \in \mathbb{N}$ iterations of IRKA and store the best iteration with respect to the relative error

$$\delta_q(H, H_r) = \frac{\|H(\cdot, q) - H_r(\cdot, q)\|_{\mathcal{H}_2(W)}}{\|H(\cdot, q)\|_{\mathcal{H}_2(W)}}. \quad (4.39)$$

The number of initial interpolation points σ is increased and IRKA is restarted until the currently best ROM fulfills the bound $\delta_q < \bar{\delta}$. After updating the interpolation directions in line 9 of alg. 2, an additional residue correction [99] proved to be beneficial. The local reduction strategy is summarized in alg. 2. Fig. 4.3 presents the Bode plot for the linear model resulting for a fixed volume flow field of the reference network district, cf. fig. 5.2. The approximation of $r = 17$ states resulting from alg. 2 is compared to the full ODE model including $n = 3008$ states. The input-output channel with the highest approximation error is displayed. We now focus on the second task of picking linearizations entering the global reduced model. Combining local projections to a global one includes the risk of creating a prohibitively large reduced system. Here, Krylov based reduction methods as presented in alg. 2 proved to be efficient with regard to the resulting reduced order [44]. To ensure that the global reduced order model captures the entire relevant system information, snapshots from a worst case

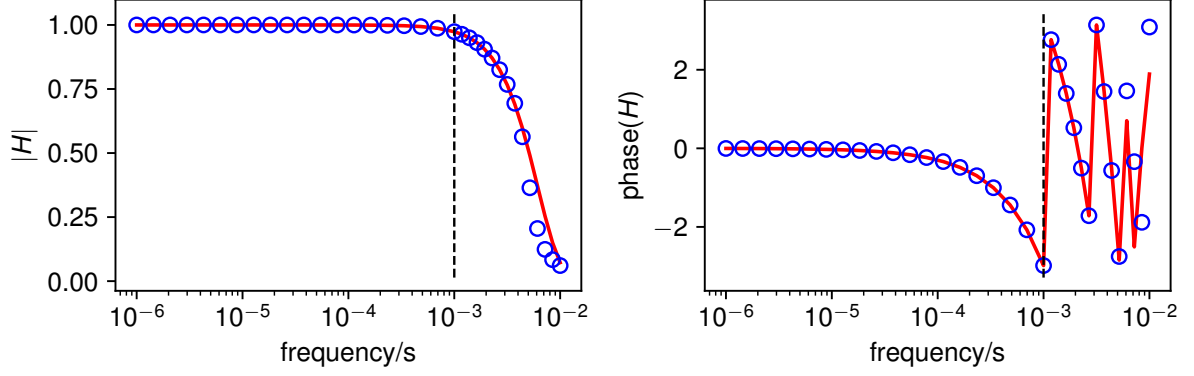


Figure 4.3: Bode plot of the transfer function H for a fixed velocity field comparing the full order model (red, solid line) resulting from the upwind scheme to the reduced order model (blue circles) resulting from alg. 2. Dashed vertical lines indicate the maximum frequency to be approximated by alg. 2.

training signal u_{tr} are generated, where the corresponding signal changes with maximal frequency and explores the entire allowed domain,

$$u_{tr} \in \mathcal{U}_T : \min_t(u_{tr}(t)) = u_l, \max_t(u_{tr}(t)) = u_h, m \cdot \omega = \hat{\omega}.$$

Specifically, the set of snapshots is denoted by \mathcal{D} and collects volume flows,

$$\mathcal{D} = \{q^1, \dots, q^{n_\delta}\}.$$

Subsequently, a greedy strategy is applied in frequency space to determine the linearizations within \mathcal{D} , which enter the global projection. It is started with an initial reduction V^i , generated by the Krylov subspace R^i , which is the initial value for the current interpolation space \mathcal{R}^{in} . The notation R^i addresses the Krylov subspace which results for applying alg. 2 to the linear system defined by the volume flow q^i ,

$$R^i := R^i(\sigma^i, b^i, q^i) = [(\sigma_1^i \mathbb{1} - A^E(q^i))^{-1} B^E(q^i) b_1^i, \dots, (\sigma_{n_i}^i \mathbb{1} - A^E(q^i))^{-1} B^E(q^i) b_{n_i}^i]. \quad (4.40)$$

Furthermore,

$$\mathcal{R}^{in} = \{R^i\}_{i=1, \dots, r}, \quad (4.41)$$

describes the union of the local interpolation spaces currently entering the global reduced order model. Iteratively, the parameter vector $q^M \in \mathcal{D}$ exhibiting the largest deviation to the full transfer function is determined,

$$M = \operatorname{argmax}_{j \in [1..n_\delta]} \delta_{q^j}(H, H_r). \quad (4.42)$$

Hereafter, the space R^M forming the Galerkin projection V^M is added to the current interpolation space \mathcal{R}^{in} , and the global projection V is updated using a singular value decomposition

$$V = V(\mathcal{R}^{in}; s) = \operatorname{SVD}(R^1, \dots, R^r; s). \quad (4.43)$$

Here s represents the truncation order of the singular value decomposition. It denotes the order of the logarithmic singular value decay between the largest and smallest singular value entering V . Since each of the local Galerkin projections $V^i = \text{orth}(R^i)$ supplied by alg. 2 is orthonormal by construction, the generating spaces R^i themselves are used in the generation of a global projection V . This avoids the problem that each space receives the same weight before entering the singular value decomposition. The procedure is repeated until the maximum local error in the transfer function with respect to all parameter values in the test set \mathcal{D} ,

$$\Delta^\delta(\mathcal{D}, V) = \max_{q \in \mathcal{D}} \delta_q(H, H_r^V), \quad (4.44)$$

is smaller than the global threshold $\bar{\Delta}$. Note that the projection matrix V in (4.44) yields the reduced order transfer function which is expressed in the notation H_r^V . Using the singular value decomposition (4.43) to combine local spaces removes undesired redundancies and decreases the resulting order of the surrogate model. Still, the global projection might include modes which are not redundant but unnecessary for the approximation of the relevant time domain simulations. Therefore, it is useful to vary also the initial reduction starting the greedy selection. It was not added by the largest error criterion and thus might introduce unwanted properties of the final projection. The procedure of calculating a global Galerkin projection is summarized in alg. 3. The effect of varying the initial linearization entering alg. 3 and the order of

Algorithm 3 Determination of global projection matrix V : frequency greedy

Require: Evaluation points of volume flow vectors $\mathcal{D} = \{q^1, \dots, q^{n_\delta}\}$, error bounds $\bar{\delta}$, $\bar{\Delta}$, order s of SVD

Require: Local interpolation space $R^i = R^i(\sigma^i, b^i, q^i)$ s.t. $\delta_{q^i} < \bar{\delta} \ \forall q^i \in \mathcal{D}$

Ensure: Global Galerkin projection V

```

1: for  $i=1 : n_\delta$  do
2:   Initialize  $\mathcal{R}^{in} = R^i$ , with  $q^i \in \mathcal{D}$ 
3:   set initial, global projection  $V = \text{SVD}(\mathcal{R}^{in}; s)$ 
4:   determine initial, global error  $\Delta^\delta(\mathcal{D}, V)$ 
5:   while  $\Delta^\delta \geq \bar{\Delta}$  do
6:     determine evaluation with largest deviation  $M = \arg\max_{j \in [1..n_\delta]} \delta_q(H, H_r^V)$ 
7:     augment interpolation space  $\mathcal{R}^{in} = \mathcal{R}^{in} \cup R^M$ 
8:     determine global Galerkin projection  $V = \text{SVD}(\mathcal{R}^{in}; s)$ 
9:     update global error  $\Delta^\delta(\mathcal{D}, V)$ 
10:  end while
11: end for
12: return  $V$ 
```

the singular value decay of the global projection V is visualized exemplarily in fig. 4.4. It shows a Pareto frontier, containing points which are unique in the sense that each other point either represents a larger reduced dimension or a larger approximation error in frequency space. When sampling from this frontier two extreme cases occur. First, the smallest projection matrix fulfilling the approximation error $\bar{\Delta}$. Second, the smallest approximation matrix, exhibiting the smallest measured approximation

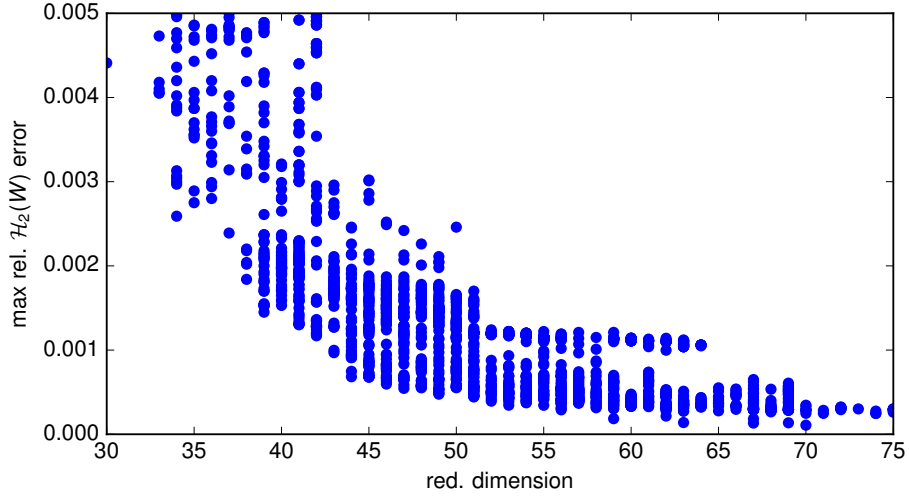


Figure 4.4: Scatter plot of Galerkin projections resulting from alg. 3 for the reference network street, cf. fig. 5.1. Visualized is the variation of the initial volume flow field q^i entering the global interpolation space first, as well as the variation of the truncation order s of the singular value decomposition.

error. In addition, a heuristic quality indicator κ is defined which aims at finding a compromise between both extreme points

$$\kappa = \Delta^\delta r^2. \quad (4.45)$$

When associating a higher quality to a lower value of κ , (4.45) penalizes a large error linearly and a large size r of a global reduced order model quadratically. A precise description of the parameters for alg. 2, 3 yielding specific Galerkin projections is provided with the numerical examples in section 5.2, 6.2.

Remark 14. *The local interpolation spaces required in alg. 3 are computed very fast by using parallelization, since each instance of alg. 2 can be independently run on an own core. Similarly, the for loop in alg. 3 is parallelized as well, by assigning an own initialization to each core. Thus, the offline-time required to generate the reduced order model can be reduced significantly.*

4.6 Conclusions

In this chapter an algorithm to construct a global Galerkin projection for the reduction of the DAE (4.1) describing the dynamics of district heating networks was presented. The reduction aimed at the advective transport of energy densities, while preserving the algebraic equations and variables defining the temporal evolution of the velocity field. The global Galerkin projection is given by a SVD of local reduced order models resulting from the reduction of linearizations of the quasi-linear dynamical DAE. The

corresponding linearizations are defined by volume flow fields fixed in time. The local reductions result from a moment-matching technique in frequency space, focusing on the transfer function of the linearizations. A greedy strategy is employed to iteratively pick linearizations, at which the current Galerkin projection shows the largest approximation error in the local transfer function of full- and reduced order models. The benefits of the presented reduced order model are investigated numerically in the following chapters.

Chapter 5

Numerical analysis of the reduced order model

In this chapter, the reduced order model presented in section 4.5 is analyzed numerically for two real-world heating networks shown in fig. 5.1, 5.2. The first network mimics a typical combination of streets supplied by district heating networks and is referred to as reference network street (RNS). The second network represents the topology of a larger district and is referred to as reference network district (RND). The outline data of the considered networks are given in tab. 5.1. After discussing assumptions to the dynamical model investigated in this chapter, a decomposition algorithm is suggested, splitting the network model into several subnetworks. The decomposition empowers the suggested Galerkin projection by preserving a certain sparsity structure in the reduced order operators. A major complexity in the reduction of RND arises from dynamical changes of flow direction. The latter are included in an own subnetwork (SNF). Finally, the numerical analysis is performed comparing full- and reduced order models for varying number of finite volume cells and different time integration schemes. The results obtained in this chapter are conducted using MATLAB[®](R2016b) on an Intel[®]Xeon[®]CPU E5-2670 @ 2.60GHz. The simulations are performed on a cluster environment, in which no additional processes interfere. The resulting run times are averages based on three repetitions.

Network	Edges	Nodes	Cycles	Pipelines	Consumers	Pipeline length
District	1108	770	6	775	333	8676 m
Street	114	81	1	81	32	837 m

Table 5.1: Outline data for the flow part of the heating networks RND and RNS presented in fig. 5.1, 5.2.

5.1 Model assumptions

The algorithm to generate Galerkin projections applies to the full DAE (3.27), discussed in section 3.1.5. In this chapter, the numerical analysis presented subsequently is conducted for a submodel as discussed in the following. For times $t \in \mathcal{T} \subset \mathbb{R}$ we consider

$$\dot{E} = A(q)E + B(q)u_T, \quad (5.1a)$$

$$y = CE, \quad (5.1b)$$

$$Kq = 0, \quad (5.1c)$$

$$G_a(t) - q_a(t)(e_{a:k}(t) - e_R) = 0, \quad a = (k, m) \in \mathcal{C}, \quad (5.1d)$$

$$\lambda \sum_{a \in \xi} \frac{L_a}{2d_a} v_a |v_a| = 0, \quad \xi \in \mathcal{L}_{\mathcal{G}}, \quad (5.1e)$$

$$G_a(t) = \bar{G}_a. \quad (5.1f)$$

Eq. (5.1a) describes the transport of the scaled energy density within the flow network subject to the energy density injected at the power plant u_T . The scaled energy density used in the numerical simulations in this chapter is defined by

$$E = \sqrt{Q} \frac{e - e_R}{e_R}. \quad (5.2)$$

Eq. (5.2) incorporates two transformation steps. First, a transformation of the vector of energy densities $e \in \mathbb{R}^n$ with respect to the return energy density $e_R \in \mathbb{R}$ which is performed component-wise. Using this description, numerical simulations are independent of the return energy density. Second, applying \sqrt{Q} transforms (5.1a) to co-energy coordinates, in which any Galerkin projection can be applied directly while ensuring Lyapunov stability, cf. section 4.5. The operators $A(q), B(q)$ already include the conservation of energy and are formed based on the affine decomposition defined by the independent volume flows as described in section 3.3. Full- and reduced order system operators considered in this chapter are defined by

$$A(q) = Q^{\frac{1}{2}} \left(\sum_{\nu=1}^{n_q} \gamma_{\nu}^{\tilde{q}}(q) A_{\nu}^{\tilde{q}} \right) Q^{-\frac{1}{2}}, \quad B(q) = Q^{\frac{1}{2}} \left(\sum_{\nu=1}^{n_q} \gamma_{\nu}^{\tilde{q}}(q) B_{\nu}^{\tilde{q}} \right), \quad (5.3a)$$

$$A_r(q) = V^T A(q) V, \quad B_r(q) = V^T B(q), \quad C_r = CV, \quad (5.3b)$$

where $\tilde{q} \in \mathbb{R}^{|\mathcal{L}_{\mathcal{G}}|+|\mathcal{C}|}$ denotes the vector of independent volume flows, and $n_q \geq |\mathcal{L}_{\mathcal{G}}|+|\mathcal{C}|$ is the number of parameters necessary to parameterize the flux configurations including changes of flux direction, cf. section 3.3. Concerning the flow defining equations (5.1c - 5.1e), the mass density $\rho = 10^3 \text{ kg m}^{-3}$ and the friction factor $\lambda = 0.03$ are set to constant values, and thus the variation with energy density and velocity is not modeled. As a consequence, in the derivation of the cycle defining flows according to (5.1e) both quantities do not contribute to the model. The summation in (5.1e) is performed along a (closed) cycle in which the density is assumed to be a global

constant. Hence, the summation over the height differences along each pipeline in a cycle cancels to zero, since the same level of height is realized at the start and the end of the summation. By using (5.1e) to define the volume flow field, the pressure does not enter the state variables and does not affect the simulation results. Since the pressure only poses technical constraints and does not constraint the simulation of the energy transport itself, it is not considered within this chapter. In addition, thermal losses are not considered. Consequently, the return part of the presented networks is not included in the simulation. For the discussed network topologies, identical energy densities e_R are injected in the return part of the heating network (5.1d). This leads to the fact that no dynamics can be expected, and e_R is simply transported back to the power plant. The consumption profiles G_a are modeled constant in time (5.1f), where the constant \bar{G}_a results from the normalized yearly consumption of the corresponding consumer.

5.2 Simulation setup

Subsequently, the simulation setup used in this chapter is described. It applies to the numerical studies performed to analyze the decomposition strategy section 5.3 and the numerical tests of the reduced order model presented in section 5.4. According to the transformation (5.2), energy densities e' and outputs y presented below are dimensionless,

$$e' = \frac{e - e_R}{e_R}. \quad (5.4)$$

The given, total number n of finite volume cells is distributed to pipelines according to

$$n_i = \max\{n_{\min}, \text{round}\left(c_r \frac{L_i v_r}{L_r v_i}\right)\} \quad \forall i \in \mathcal{P}, \quad (5.5)$$

where L_r, v_r, c_r denote length, velocity and the expected number of cells of the reference pipeline. Eq. (5.5) aims at minimizing the variance of the CFL numbers $\Lambda_i = n_i v_i / L_i$, $i \in \mathcal{P}$ among the set of pipelines. A large variance of CFL numbers forces high diffusion of the resulting numerical solution, which is why we aim at limiting this quantity. The reference pipeline is thus the one with the largest CFL condition, where its velocity is obtained from a simulation employing typical inputs. On network systems, distributing finite volume cells on pipelines according to (5.5) leads to an adaptation of the discretization length h_α on each pipeline $\alpha \in \mathcal{P}$. In addition, the numerical results are significantly less diffusive compared to other meshing strategies such as aiming at a constant discretization h on each pipeline. A solution to decrease the high diffusion resulting from restricting the time step to the maximal CFL condition $\hat{\Lambda}$, is applying local time stepping [100]. In this approach, each pipeline is updated on a local time scale according to its individual CFL condition. The used discretization scheme is the upwind method. When coupling pipelines at junctions,

each of the coupling pipelines has to stay within a consistent time frame. In contrast, within this section global time stepping methods are discussed, allowing for an application to the suggested reduced order model. The considered error Δ^t in the time domain is defined as follows

$$\Delta^t = \max_{i \in [1..|\mathcal{C}|]} \frac{\|\hat{y}_i - \hat{y}_i^r\|_2}{\|\hat{y}_i\|_2}. \quad (5.6)$$

Here, $\hat{y}_i = (y_i(t_1), \dots, y_i(t_{|\hat{\mathcal{T}}|}))^T \in \mathbb{R}^{|\hat{\mathcal{T}}|}$, $i = [1..|\mathcal{C}|]$ collects an approximation to the PDE solution of output $i = [1..|\mathcal{C}|]$ at discrete points in time denoted by the set $\hat{\mathcal{T}}$. Similarly, $\hat{y}_i^r \in \mathbb{R}^{|\hat{\mathcal{T}}|}$ collects the evaluation of output i of the reduced order model at discrete points of time $\hat{\mathcal{T}}$. Using the maximum relative 2-norm as an error indicator ensures that each output is approximated precisely, regardless of its absolute value and other outputs. The reference solution \hat{y} is obtained by extrapolation of simulation results with increasingly fine spatial resolution. The reference model used to this end is the upwind scheme in the default combination with an explicit Euler method for the time integration. For the training phase the input signal $u_{in} \in \mathcal{U}_{\mathcal{T}}$ is used,

$$u'_{in}(t) = 0.4 + 0.2 \cos(\omega t), \quad \frac{2\pi}{\omega} = 14 \times 10^3 \text{ s}, \quad t \in \mathcal{T}, \quad (5.7)$$

spanning the allowed range for the energy density. This input signal is referred to as the in-sample signal. The Galerkin reduction resulting from algorithm 3 is further tested for the (out-of-sample) signal $u'_{out} \in \mathcal{U}_{\mathcal{T}}$

$$u'_{out}(t) = c_0 + \sum_{i=1}^2 [c_i \cos(i\omega t) + s_i \sin(i\omega t)], \quad \frac{2\pi}{\omega} = 28 \times 10^3 \text{ s}, \quad t \in \mathcal{T}, \quad (5.8)$$

with the coefficients $(c_0, c_1, c_2) = (0.37, -0.078, 0.089)$, $(s_1, s_2) = (c_1, -c_1)$. The input signals defined in (5.7-5.8) are highly volatile compared to practical controls. Note that u'_{in}, u'_{out} are defined in the transformed coordinate system given in (5.4). For signal (5.7), the energy density in the flow network achieves its extrema $e' \in [0.2, 0.6]$ within half the time period, $14 \times 10^3 \text{ s} \approx 3.9 \text{ h}$. The initial state for all simulations equals the equilibrium state defined by the initial control

$$e'_{\alpha,\beta}(t_0) = u'(t_0), \quad \alpha \in \mathcal{P}, \quad \beta \in \mathcal{Z}_{\alpha}.$$

As a consequence, both input signals u'_{in}, u'_{out} are continuous in time, while u'_{in} is in addition differentiable, since $\dot{u}'_{in} = 0$.

Parameter choice for the generation of Galerkin projections

The simulations presented subsequently are run along the time interval $\mathcal{T} = [0, 8 \times 10^4] \text{ s}$. To generate data for the training phase of alg. 2, 3 the input signal u'_{in} was simulated with snapshots equidistant in time with a step size of 5 min. Subsequently, typical parameter choices for the generation of projections matrices according to alg. 2,

Network	Strategy	#(subnetworks)	Figures	Pareto frontier
RNS	Reduce entire network	1	fig. 5.1	quality (4.45)
RND	No reduction of SNF	29	fig. 5.2	smallest error
RND	No reduction of SNF	16	fig. 5.6	smallest error
RND	Reduction of SNF	16	fig. 5.6	smallest size

Table 5.2: Summary of topologies and reduction strategies considered within this chapter. Subnetworks correspond to the domain decomposition discussed in the following section. The numerical results presented in section 5.4.1 are obtained by reducing RNS as one network, not as the decomposed network shown in fig. 5.1. The column Pareto frontier indicates how global Galerkin projections are chosen for the major part of subnetworks.

3 are presented. The set of admissible frequencies is set to $W = [10^{-5}, 10^{-3}] \text{ s}^{-1}$, cf. (4.39). The weighted transfer function (4.38) is approximated using a Gauß-Legendre quadrature with 30 base points. Concerning the determination of a local Galerkin projection using alg. 2, an error indicator $\bar{\delta} = 10^{-2}$ is used. Initial interpolation points are distributed logarithmically between 10^{-7} and 10^0 along the real axis. For the determination of a local reduction, IRKA is initialized with two interpolation points. If the local error of the determined ROM (4.39) is larger than $\bar{\delta}$, the number of interpolation points is increased by 2. The number of iterations in a single instance of IRKA is limited by $N = 15$.

The determination of a global projection according to alg. 3 is performed with a global threshold $\bar{\Delta} = 5 \times 10^{-3}$. The order of the singular value decomposition is chosen within the range $s \in [10..14]$. For the different topologies discussed hereafter, different strategies are used to pick Galerkin projections matrices from the Pareto frontier introduced by alg. 3. For the RNS, the quality criterion (4.45) is used. For selected subnetworks of RND, the choice of reduction matrices from the Pareto frontier and the global error indicator $\bar{\Delta}$ have to be adjusted to meet the desired accuracy in the time domain simulations. In addition, initializing the interpolation frequencies σ along the positive imaginary axis proved to be advantageous in some situations. An overview mapping network topologies and reduction strategies studied in this chapter is provided in tab. 5.2.

5.3 Domain decomposition of heating networks

When applying dense Galerkin projections $V \in \mathbb{R}^{n \times r}$, the sparsity of the operator $A(q)$ introduced by the network structure transforms to a highly dense reduced matrix. While $A(q) \in \mathbb{R}^{n \times n}$ for typical heating networks has $c \cdot n$, $c \in [2, 3]$ nonzero entries, $V^T A V$ carries r^2 nonzeros entries. To reduce large scale networks more efficiently, a decomposition into several subnetworks is performed [101]. This allows to apply the dense Galerkin projection to each subsystem separately and preserves sparsity in the

resulting reduced order operators. Furthermore, a decomposition into subnetworks allows for an efficient parallelization of simulations tasks. Due these facts, clustering techniques and related domain decompositions are an active field of research [102, 101, 66, 103].

5.3.1 Decomposition into main- and subnetworks

A description of heating networks decomposed in a main- and several subnetworks is proposed in the following form

$$\begin{pmatrix} \dot{E}^0 \\ \dot{\tilde{E}} \end{pmatrix} = \begin{pmatrix} A^0(q) & \\ & \tilde{A}(q) \end{pmatrix} \begin{pmatrix} E^0 \\ \tilde{E} \end{pmatrix} + \begin{pmatrix} B^0(q) & \\ & \tilde{B}(q) \end{pmatrix} \begin{pmatrix} u_T \\ \tilde{y} \end{pmatrix}, \quad (5.9a)$$

$$\begin{pmatrix} \tilde{y} \\ y \end{pmatrix} = \begin{pmatrix} C_{\tilde{y}}^0 & \\ C_h^0 & \tilde{C} \end{pmatrix} \begin{pmatrix} E^0 \\ \tilde{E} \end{pmatrix}, \quad (5.9b)$$

$$0 = g(E, q, \Gamma). \quad (5.9c)$$

Eq. (5.9) is equivalent to (3.27). As in (3.27), the algebraic constraints (5.9c) result from the coupling of pipelines at nodes of the network and gather three contributions (5.1c - 5.1e): the conservation of volume, Kirchhoff's second law claiming that pressure differences along network cycles sum up to zero, and the power balance at consumers. It forces the product of volume flow q at consumer stations and observed energy density y to equal the power consumption G . Hence, (5.9c) collects quadratic constraints in the state variables E , q . Absolute pressure values p are not considered within this chapter as they only enter optimization constraints which are discussed in chapter 6.

The system description is decomposed to a main network with state vector E^0 to which the thermal control u_T is applied, and $c \in \mathbb{N}$ subnetworks forming \tilde{E} which receive observables \tilde{y} as artificial inputs. Observables y are measured by both main- and subnetworks, while \tilde{y} is the system state of the main network at attachment points to subnetworks. $\tilde{A}, \tilde{B}, \tilde{C}$ represent continued block diagonal matrices,

$$\tilde{A}(q) = \begin{pmatrix} A^1(q) & & \\ & \ddots & \\ & & A^c(q) \end{pmatrix}, \quad \tilde{B}(q) = \begin{pmatrix} B^1(q) & & \\ & \ddots & \\ & & B^c(q) \end{pmatrix}, \quad \tilde{C} = \begin{pmatrix} C^1 & & \\ & \ddots & \\ & & C^c \end{pmatrix}.$$

Their blocks $A^s, B^s, C^s, s \in \{1, \dots, c\}$ describe the dynamics of the subnetworks. Both $A^s(q)$, and $B^s(q)$ depend on the vector of volume flows q , and are represented by the parameterization (5.3)

$$A^s(q) = \sum_{i=1}^{n_q} \gamma_i(\tilde{q}) A_i^s, \quad B^s(q) = \sum_{i=1}^{n_q} \gamma_i(\tilde{q}) B_i^s, \quad s \in \{0, \dots, c\}.$$

We approximate the input-output characteristics of each system $s \in \{0, \dots, c\}$ using the greedy strategy described in chapter 4. Thus, for each system, an individual projection V^s , $s \in \{0, \dots, c\}$ results, forming the global projection

$$V = \begin{pmatrix} V^0 & \\ & \tilde{V} \end{pmatrix}. \quad (5.10)$$

Application of V to (5.9) defines the reduced order model for the decomposed network description.

5.3.2 Preservation of Lyapunov stability

Subsequently it is shown that the application of the Galerkin projection V (5.10) to the system (5.9) allows to conclude for Lyapunov stability of the reduced, decomposed system. To this end \tilde{y} is eliminated in (5.9a), using (5.9b). Hence, one obtains a system description as a single network (5.11) equivalent to (5.9) where the links of main- and subnetworks are rewritten to the system matrix $A(q)$

$$\begin{pmatrix} \dot{E}^0 \\ \dot{\tilde{E}} \end{pmatrix} = \begin{pmatrix} A^0 & \\ \tilde{B}C_{\tilde{y}}^0 & \tilde{A} \end{pmatrix} \begin{pmatrix} E^0 \\ \tilde{E} \end{pmatrix} + \begin{pmatrix} B^0 \\ 0 \end{pmatrix} u_T, \quad (5.11a)$$

$$y = (C_h^0 \quad \tilde{C}) \begin{pmatrix} E^0 \\ \tilde{E} \end{pmatrix}. \quad (5.11b)$$

For simplicity of presentation, the algebraic equation (5.9c) is dropped in this section. As shown in theorem 7, system (5.11) and its reduced model obtained by a Galerkin projection are Lyapunov stable for an upwind discretization. To show that the reduced order system obtained by (5.9) is stable as well, (5.9) is reduced by the Galerkin projection (5.10), leading to

$$\begin{pmatrix} \dot{E}^0 \\ \dot{\tilde{E}} \end{pmatrix} = \begin{pmatrix} (V^0)^T A^0 V^0 & \\ & \tilde{V}^T \tilde{A} \tilde{V} \end{pmatrix} \begin{pmatrix} E^0 \\ \tilde{E} \end{pmatrix} + \begin{pmatrix} (V^0)^T B^0 \\ \tilde{V}^T \tilde{B} \end{pmatrix} \begin{pmatrix} u_T \\ \tilde{y} \end{pmatrix} \quad (5.12a)$$

$$\begin{pmatrix} \tilde{y} \\ y \end{pmatrix} = \begin{pmatrix} C_{\tilde{y}}^0 V^0 \\ C_h^0 V^0 \quad \tilde{C} \tilde{V} \end{pmatrix} \begin{pmatrix} E^0 \\ \tilde{E} \end{pmatrix}. \quad (5.12b)$$

In (5.12), \tilde{y} is again eliminated resulting in

$$\begin{pmatrix} \dot{E}^0 \\ \dot{\tilde{E}} \end{pmatrix} = \begin{pmatrix} (V^0)^T A^0 V^0 & \\ \tilde{V}^T \tilde{B} C_{\tilde{y}}^0 V^0 & \tilde{V}^T \tilde{A} \tilde{V} \end{pmatrix} \begin{pmatrix} E^0 \\ \tilde{E} \end{pmatrix} + \begin{pmatrix} (V^0)^T B^0 \\ 0 \end{pmatrix} u_T \quad (5.13a)$$

$$y = (C_h^0 V^0 \quad \tilde{C} \tilde{V}) \begin{pmatrix} E^0 \\ \tilde{E} \end{pmatrix}. \quad (5.13b)$$

It is straight forward to see that (5.13) is the Galerkin projection of (5.11), concluding for Lyapunov stability of (5.12).

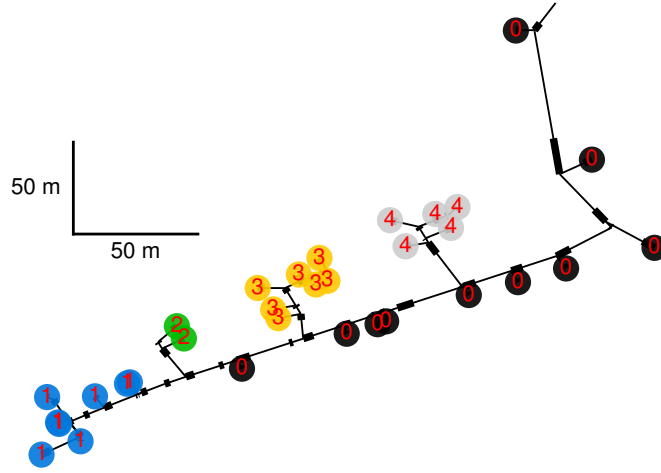


Figure 5.1: Illustration of the proposed decomposition algorithm for an existing network RNS with 32 observables at 32 consumers (colored circles). Numbers and colors visualize subnetworks.

5.3.3 Decomposition strategy and numerical validation

Towards a beneficial network decomposition, we aim at equalizing the number of observables $n(y^s)$ to be approximated in each subnetwork. To this end, the following strategy is proposed. In a directed graph \mathcal{G} , a recursive tree search is performed. The number of allowed outputs in potential subnetworks is restricted to $\{2, \dots, \tilde{N}\}$, where $\tilde{N} \in \mathbb{N}$ is an external parameter. Based on the current root node r , the dimension $n(y^s)$ of the output vector y^s in the underlying subnet S_s is counted. If $n(y^s) \in \{2, \dots, \tilde{N}\}$, and S_s contains no outputs which are already clustered, S_s is defined to be a new subnet. Since the optimal choice of \tilde{N} is not defined a-priori, the cost function

$$\mathcal{J}(\tilde{y}) = n(\tilde{y})^2 + \sum_{s=0}^c n(y^s)^2 \quad (5.14)$$

is evaluated to indicate beneficial cluster decompositions. $\mathcal{J}(\tilde{y})$ penalizes both the number of connection points $n(\tilde{y})$ of main- and subnetworks, and the number of observables in each subnetwork $n(y^s)$ quadratically. The suggested algorithm is summarized in alg. 4. For the reference network street (RNS), the cost-minimal choice $\tilde{N} = 8$ resulting from the variation of \tilde{N} is visualized in fig. 5.1.

Numerical validation

The influence of the proposed decomposition on the simulation runtime is demonstrated for a computationally more demanding reference network district (RND) including $n(y) = 333$ outputs. Since it includes changes of flux directions which are

Algorithm 4 Network decomposition strategy: $\text{node}(k, \mathcal{G}, \tilde{N})$ **Require:** Graph structure \mathcal{G} , root node k , max. number of observables \tilde{N} **Ensure:** Subnetworks C

```

1: for child nodes  $k'$  of root (breadth first) do
2:    $S \leftarrow$  subgraph defined by node  $k'$ 
3:    $y \leftarrow$  observables of  $S$ 
4:   if  $\#(y) \in [2, \dots, \tilde{N}]$  and  $y_i \notin C_j$ ,  $i = [1, \dots, |y|]$ ,  $j = [1, \dots, c]$  then
5:     add  $S$  as own cluster:  $c \leftarrow c + 1$ 
6:      $C_c \leftarrow S$ 
7:   else
8:     call algorithm recursively:  $\text{node}(k', \mathcal{G}, \tilde{N})$ 
9:   end if
10: end for
11: return  $C$ 

```

	runtime/s	rel. error Δ^t	DOF
FOM 1 subnet	2297	8.52×10^{-3}	47508
FOM 29 subnets	592	8.52×10^{-3}	47508
ROM 29 subnets	336	8.39×10^{-3}	10928

Table 5.3: Maximum relative error Δ^t , runtime and estimated complexity for the reference network RND. The error Δ^t , cf. (5.6) compares the PDE solution vector y to the approximation y^r . DOF denotes the number of finite volume cells for both full and reduced models. The time integration for all models is performed by the MATLAB[®] implicit Runge-Kutta scheme ode15s.

complex to reduce, we encapsulate them in a single subnet (highlighted in green in fig. 5.2) which is not reduced. We then compare three simulation models. The full order model discretized by the upwind scheme with 1 subnet (FOM 1), the FOM with 29 subnets proposed by our algorithm (FOM 29), displayed in fig. 5.2 and the ROM obtained from reducing all 29 subnetworks except for the one including flux changes (ROM 29), cf. tab. 5.3. Comparing FOM 1 to FOM 29 shows that a large speed up already results for the unreduced system by network decomposition. Although the number of nonzero entries in the full order operator is nearly identical, the block diagonal structure allows for a more efficient solution of the nonlinear root problems occurring in an implicit time integration. Furthermore, the operator assembly of $A(q)$ is more efficient in the decomposed description (5.9). Expressing $A(q)$ by volume flows q as time dependent weights introduces redundant multiplications when forming $q_i(t)A_i$. The part of the system operator A of a single pipeline $k \in \mathcal{P}$ coupling to e.g. two volume flows q_a, q_b could also be formed by a single multiplication of the relevant cells with the velocity on the pipeline. Defining block diagonal parts which are only multiplied with the volume flows relevant for the corresponding subnetworks, relaxes these redundancies to some extent. Concerning the reduced order operator the same observations hold. Using a network decomposition significantly accelerates the assignment of the reduced order operator $A_r(q)$ based on the affine decomposition

including volume flows. The reduced order modes resulting from Galerkin projections are now confined to the subnetworks they refer to. An additional saving of computational complexity is accounted to the reduced dimension itself. For both the training phase and the numerical evaluation presented in tab. 5.3, the input energy density u'_{in} defined in (5.7) was used.

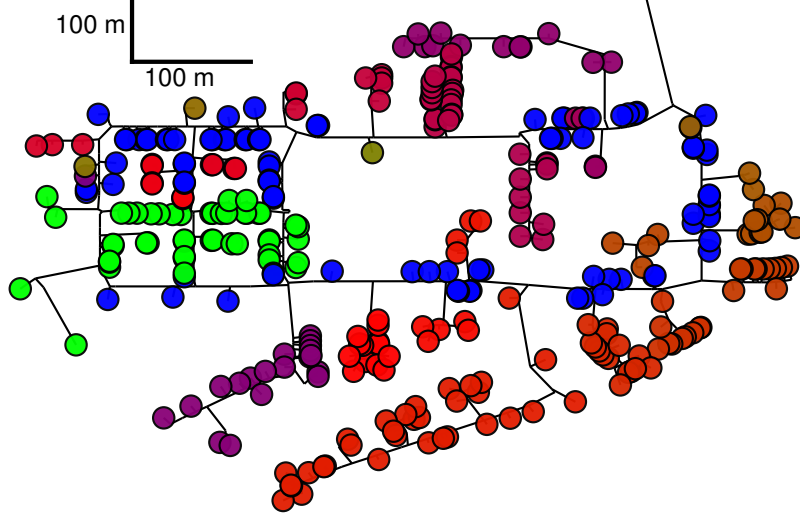


Figure 5.2: Illustration of the proposed decomposition algorithm for an existing network RND with 333 observables at consumers (colored circles). The network is decomposed to a main network (dark-blue circles) and 28 additional subnetworks including the flux changing network (green).

5.4 Numerical analysis of the reduced order model

In this section, we study the approximation quality and the runtime of the reduced model presented in section 4.5 for different input scenarios and different real world networks. In the benchmark, different time integration schemes are considered, as well as higher order hyperbolic schemes. Furthermore, different approximation qualities defined by the number of finite volume cells are studied. For network RNS the network decomposition discussed in section 5.3 is not considered due to the smaller size of the network. For the second test case, RND, the simulation results of the reduced order model are obtained by applying a network decomposition and applying Galerkin projections to each subnetwork afterwards. For the full order models, no decomposition strategy is performed.

5.4.1 Test case street network

The first example represents a street with 32 consumers and one cycle forming 33 independent volume flows (parameters), cf. fig. 5.1. Due to its small size, no network decomposition is performed for the simulations presented in this section for both full- and reduced order models. The reduced order models are calculated for the entire flow network. Figure 5.3 a), b) show the PDE solution for the two input signals (5.7, 5.8)

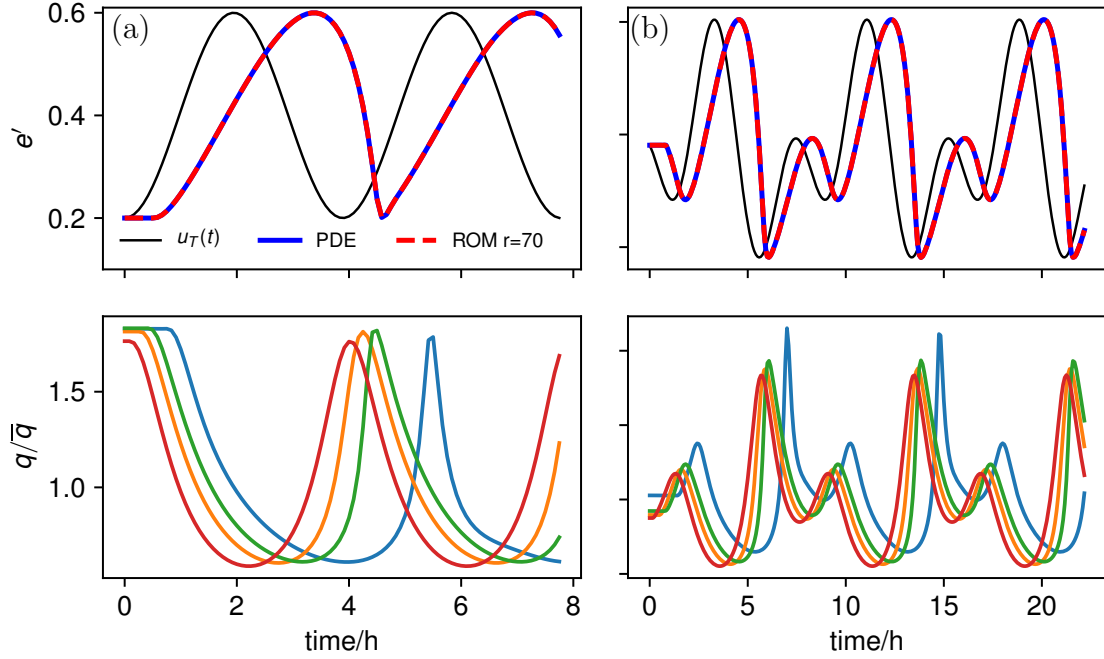


Figure 5.3: Comparison of the PDE solution and the reduced model with $r = 70$ states for the street network RNS for the in-sample signal(a), and the out-of-sample signal(b) showing the output with largest error in the time domain. The black line presents the corresponding input signal. The lower part of both plots shows the normalized temporal variation of volume flows at selected consumers, cf. (5.1d).

and the output y of the ROM exhibiting $r = 70$ states. The original cosine wave is inclined asymmetrically due the time dependent transport velocity. The ROM is able to precisely reflect the nonlinear dynamics of the street network for both in-sample and out-of-sample signals. The presented dimension reduction from full $n = 22652$ to $r = 70$ states is remarkable given the high number of 32 outputs to be approximated, cf. tab. 5.4. The time integration scheme used in fig. 5.3 is the ode15s integrator of MATLAB®, an implicit Runge-Kutta with variable step size. An analytical estimate for the Jacobian is passed to the function. The lower part of fig. 5.3 presents the normalized volume flow at selected consumer stations. The phase shift of the flow signals visualizes the transport delay from source to consumption and is a measure for

Dimension n FOM	2269	4529	11330	22652	37760	9538	47508	94991
Dimension r ROM	47	47	55	70	94	2579	10848	21106

Table 5.4: State space dimensions of full and reduced order model leading to comparable errors in the time integration for network RNS(left part) and RND(right part). For RND the presented dimensions are sums of the dimensions of each subnetwork.

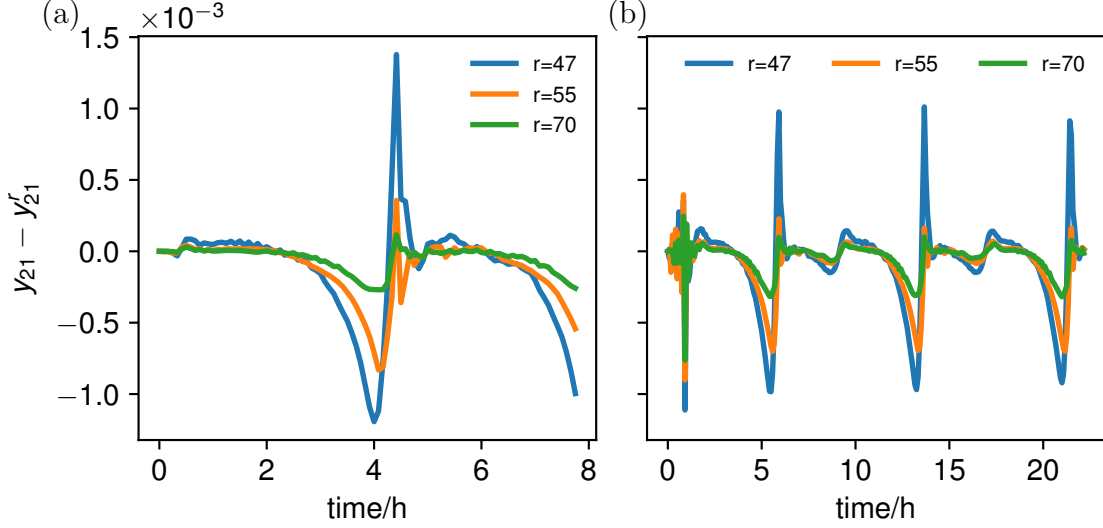


Figure 5.4: Absolute error of output 21 in network RNS which is the most distant to source, comparing in-sample input signal(a) to the out-of-sample signal(b). The size of the ROM is changes by reducing finer resolutions of the full order model, cf. tab. 5.4.

the nonlinearity of the dynamics. Employing an upwind discretization of the PDE, the number of finite volume cells is increased to compare the development of runtime, approximation error and size of full and reduced models. Figure 5.4 visualizes the time domain error of ROMs resulting from the reduction of increasingly fine full order models. By reducing a finer full order model, the corresponding ROM shows a smaller time domain error at the expense of an increasing reduced dimension.

Comparison of runtime and error

To further investigate the effects on the runtime of the ROM for different resolutions of the spatial discretization, the number of finite volume cells is varied and different time integration schemes are applied to both full and reduced models, cf. fig. 5.5. More precisely, FOM Euler (FOM ode15s) denotes an upwind discretization of the full order model, where the time integration is performed using the explicit Euler scheme

(the implicit, adaptive Runge-Kutta-method ode15s supplied by MATLAB[®]). Additionally, FOM ADER 1(2) denote ADER schemes [104] of order 1(2) for hyperbolic conservation laws, which are integrated by an explicit Euler scheme. The latter represent higher order numerical schemes for hyperbolic PDEs discussed in section 3.1. Finally, ROM ode15s is the reduced order model of the upwind discretization in space, integrated in time using ode15s. Since ode15s chooses the size of the time step adaptively based on tolerances, simulations for a given number of finite volume cells are repeated for different absolute and relative tolerances. Fig. 5.5 only presents advantageous tolerance choices, which are either more accurate or faster than other tolerance choices. It turns out that the reduced order model can be simulated with default tolerance goals, while the tolerance for the full order model has to be refined when using a higher number of finite volume cells. It shall be noted that the explicit Euler method does not ensure a stable time integration of the reduced order model. First, due to the nonlocality of the reduced order modes, there exists no CFL condition ensuring a stable time integration. Second, the ODE describing the transport of energy density is a nonlinear function of the energy density, due to the power balance at consumers stations, relating advection velocity and energy density. As a consequence, the stability radius of the time step of the explicit Euler method is only valid locally, and does not guarantee stability for larger time steps of the reduced order model. For this reason, the explicit Euler integration is not presented for the ROM.

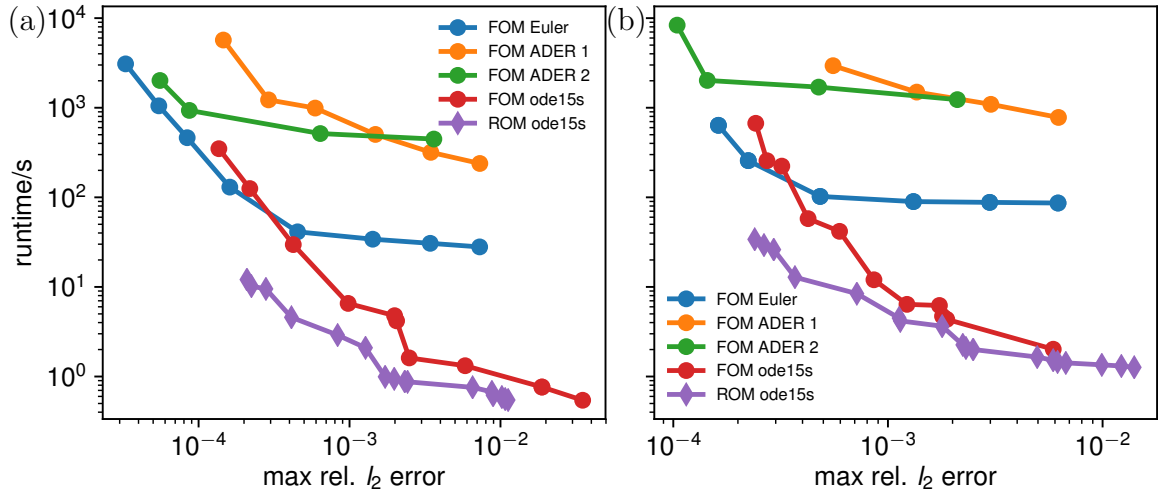


Figure 5.5: Runtime versus time domain error Δ^t for the reference network RNS varying both time- and space discretizations for the in-sample signal (a) and the out-of-sample signal (b).

Going from higher to smaller approximation errors, two regimes are visible. In the first one denoted by synchronization regime, the numerical transport velocities reflected by the CFL number $\Lambda_i \in \mathcal{P}$, synchronize over all pipelines. Here, explicit time integration schemes, in which the time step is restricted by $\hat{\Lambda} := \max_{i \in \mathcal{P}} \Lambda_i$, show a high computational effort compared to implicit time integration schemes for higher errors.

This effect aggravates for ADER schemes of order p since they require a minimum number of p cells, further diminishing the maximum step size. Increasing the number of finite volume cells, $\hat{\Lambda}$ remains constant in the synchronization phase and explicit time stepping models improve in accuracy without larger additional costs. Towards the end of the synchronization, $\hat{\Lambda}$ increases in the number of cells n and the computational costs increase superlinear in n . The implicit time integration of the upwind scheme is in particular fast in the synchronizing regime in which the problem is stiff. With increasing number of cells, the stiffness of the problem reduces, and the benefits of the full order implicit time integration vanish as well. An advantage of implicit time integration schemes results from the time-varying advection velocity. For an explicit time integration, the velocity at time t is assumed to be constant throughout the following time step. Implicit integration schemes in contrast solve for a future time step at which the new velocity field is automatically implied. Comparing the implicit time integration for full and reduced order models, the speed-up increases towards finer resolutions. As a consequence, the reduced model shows the smallest runtime within the considered error range. This range is suitable for optimal control purposes, in which an exact solution is not the central objective, but a fast estimate of it.

5.4.2 Test case district network

In the second example we consider a larger network with $|\mathcal{C}| = 333$ consumers, $|\mathcal{P}| = 775$ pipelines and $|\mathcal{L}_G| = 6$ cycle flows, which represents the network topology of an existing district, cf. fig. 5.6. Due to multiple cycles in the left part of the

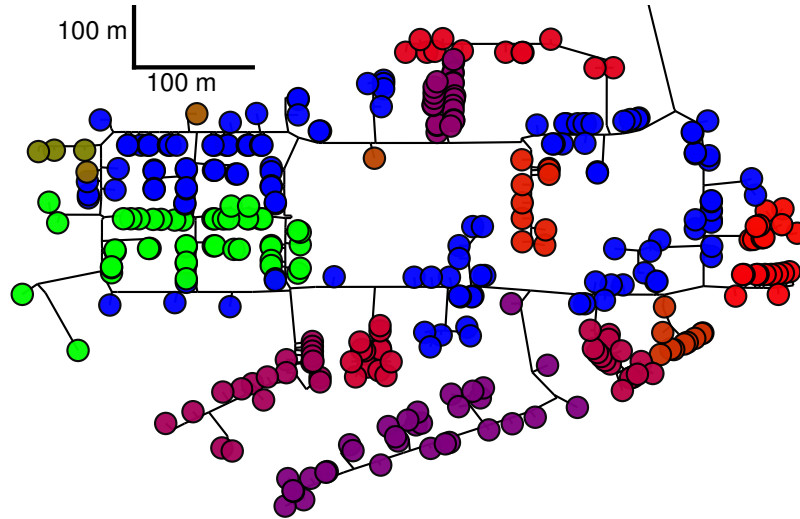


Figure 5.6: Reference network "RND" with 333 consumers, 775 pipelines and 6 cycles modeling an existing network for a city district. Colors show the manual decomposition of the network including a main network (blue), the subnetwork "SNF" exhibiting changes of the flux direction (green) and 14 additional subnetworks.

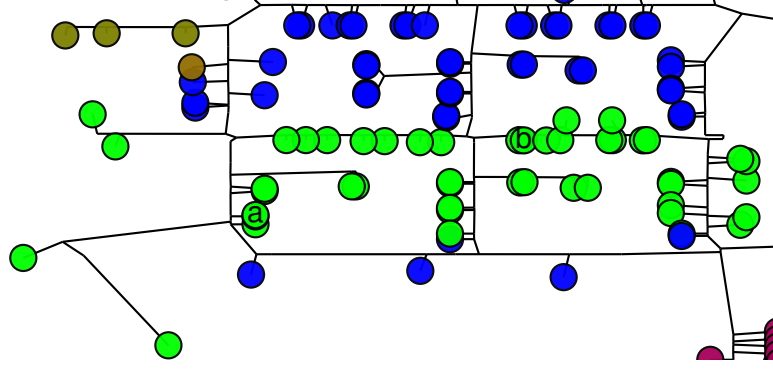


Figure 5.7: Zoom to the subnetwork exhibiting changes of flux direction, cf. fig. 5.6. Highlighted consumers correspond to signals displayed in fig. 5.9, 5.10 for consumer (a), and fig. 5.11 for consumer (b).

network, changes in the flow direction occur for the chosen control. The latter modifies the coupling structure of the finite volume cells in the reverting pipelines, since the boundary cells supplying incoming information change with the inflow boundary. The corresponding system matrix $A(q)$ changes its sparsity structure, in contrast to the case of constant flux direction, where a change of volume flow modifies the relative weights of the entries. When generating projections for this network incorporating these nonlinearities, a prohibitively large reduced dimension results. This is a very challenging aspect of simulating heating networks, which only occurs in distinct parts of large networks, where multiple cycle structures are directly connected. To isolate flux changes, the network is decomposed into a main- and 14 subnetworks, cf. fig. 5.6. Specifically, the subnetwork highlighted in green gathers all pipelines undergoing a change of flux direction and is referred to as "SNF". An augmented representation of SNF is visualized in fig. 5.7. It shall be noted that the decomposition studied subsequently differs from the output of alg. 4 presented in fig. 5.2. The aim of section 5.3 is to demonstrate that a network decomposition similar to the one considered in this section can be derived systematically.

We compare two strategies. First, a reduced order model is derived by alg. 3 for every subnetwork, and second, we perform a hybrid approach in which only the subnetwork including flux changes remains in full order. In case of the full order model, no decomposition algorithm is performed. We start with strategy 2 and discuss the runtime of the resulting ROMs. Concerning the dynamics, changes in the flux direction introduce a highly nonlinear response of the system, compare fig. 5.9, 5.10. A simple sine-wave will lead to oscillatory outputs at consumer stations. By preserving the full order in these regions, flux changes can be resolved adequately. Although the subnetwork containing the flux changes receives outputs from other reduced order models due to the network decomposition, the resulting errors are still within the resolution of the original FOM. Without reduction of SNF carrying the essential part of discretization cells, the dimension of the problem decreases from $n = 47508$ to $r = 10848$. Focusing on the runtime comparison for different accuracies, the hybrid ROM with an implicit time integration outperforms both implicit and explicit time

integrations of the FOM for the considered error range, cf. fig. 5.8. Furthermore the speed-up of the reduced order model is shifted towards smaller relative errors. This reduction in computational complexity has two origins. Firstly, due to the network decomposition, diagonal blocks in the system matrix $A(q)$ are formed, which allow for an efficient assembly of $A(q)$ defined in (5.3), as well as an efficient LU decomposition, when solving for the new time step in an implicit integration scheme. Secondly, due to the reduced state, each block is smaller in absolute size.

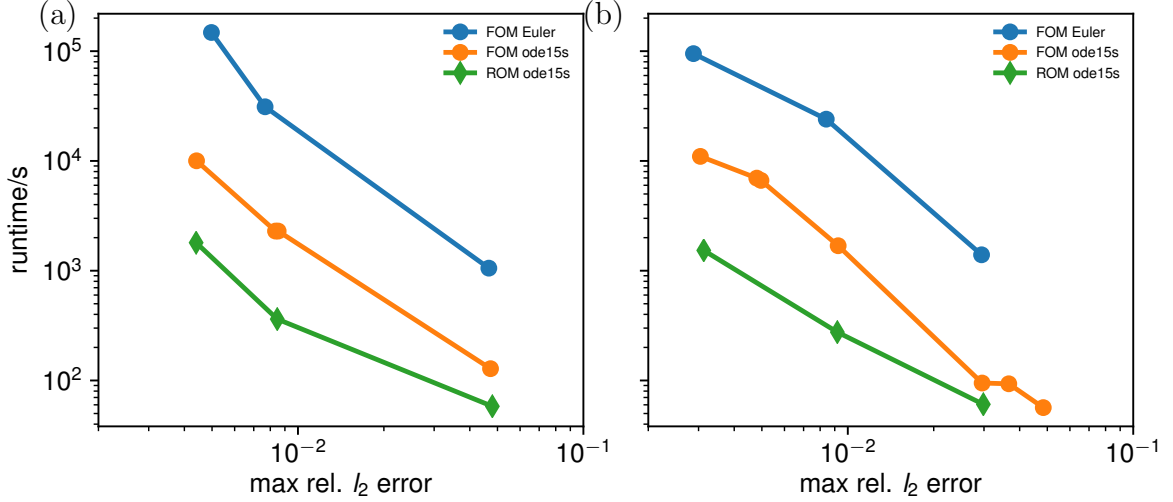


Figure 5.8: Runtime versus time domain error Δ^t for the reference network RND varying both time- and space discretizations for the in-sample signal (a) and the out-of-sample signal (b).

5.4.3 Reduction of subnetworks including changes of flow direction

While being accurate in regions of flux changes, the hybrid approach has two central drawbacks. By not reducing all parts of the network, the number of time steps for the implicit time integration is still defined by the unreduced subnetwork. In addition, it dominates the resulting reduced state space dimension, cf. tab. 5.4. To this end, we discuss the reduction of SNF. Deriving a Galerkin projection for SNF is significantly more complex than for other networks. To encapsulate all flux changes, SNF requires six attachments points at which inflowing states are measured cf. fig. 5.6. These transfer to input channels when performing the model reduction, resulting in a six-fold number of input-output channels to be approximated. Despite this fact, and the structural changes of the system matrix $A(q)$, alg. 3 produces a highly accurate ROM, cf. fig. 5.11. Furthermore, by constructing a global ROM both the the number of time steps and the state space dimension decrease significantly from $n = 47508$ to $r = 1377$. In contrast, the increasing cost for the evaluation of the dense reduced model SNF detracts the decrease in runtime, while exhibiting a larger relative error in the time domain, cf. fig. 5.5. Still, the runtime of the model also reducing SNF is

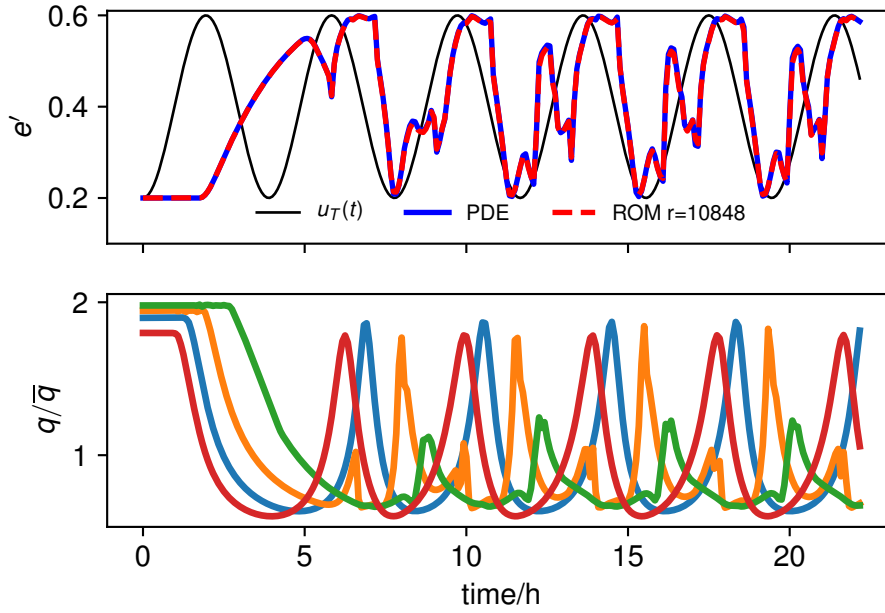


Figure 5.9: Comparison of the PDE solution and the reduced scheme for the district network RND for the in-sample input at consumer (a) in fig. 5.7. The black line presents the corresponding input signal. The high number of reduced states results from the unreduced subnetwork SNF. The lower part of both plots shows the normalized temporal variation of volume flows at consumers, cf. (5.1d).

	FOM($n = 47508$)	ROM hybrid($r = 10848$)	ROM($r = 1377$)
runtime/s	2274	363	322
rel. error Δ^t	8.34×10^{-3}	8.46×10^{-3}	11.83×10^{-3}

Table 5.5: Runtime and relative error for RND comparing the full order model (FOM), its reduction excluding flux changes (ROM hybrid) and its reduction including flux changes (ROM) for the in-sample input signal.

smaller than the runtime of the hybrid approach. As a consequence, both approaches lead to comparable results concerning accuracy and runtime. As already mentioned, the analytical Jacobian is passed to the implicit time integration scheme ode15s. Still, calculating the Jacobian is more complex than evaluating the differential part of the DAE (5.1). However, the adaptive implicit time integration scheme ode15s does not evaluate the Jacobian in every time step, but in only a fraction of those. This is in contrast to the implicit midpoint rule presented in chapter 6, in which the Jacobian has to be determined in every time step. As a consequence, the benefits of including the flux changing network in the reduction depend on the choice of the time integration scheme and the application of interest.

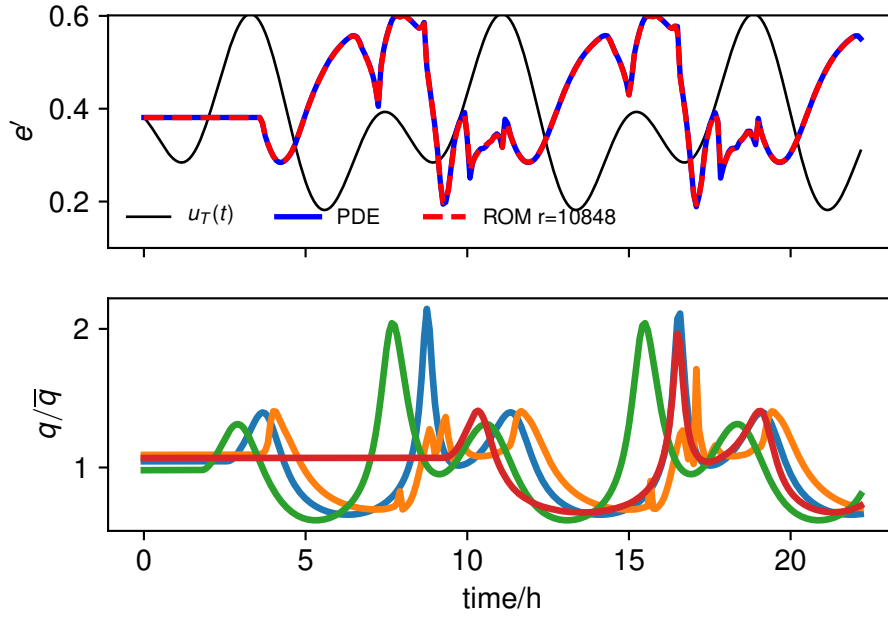


Figure 5.10: Comparison of the PDE solution and the reduced scheme for the district network RND for the out-of-sample signal at consumer (a) in fig. 5.7. For further details we refer to fig. 5.11.

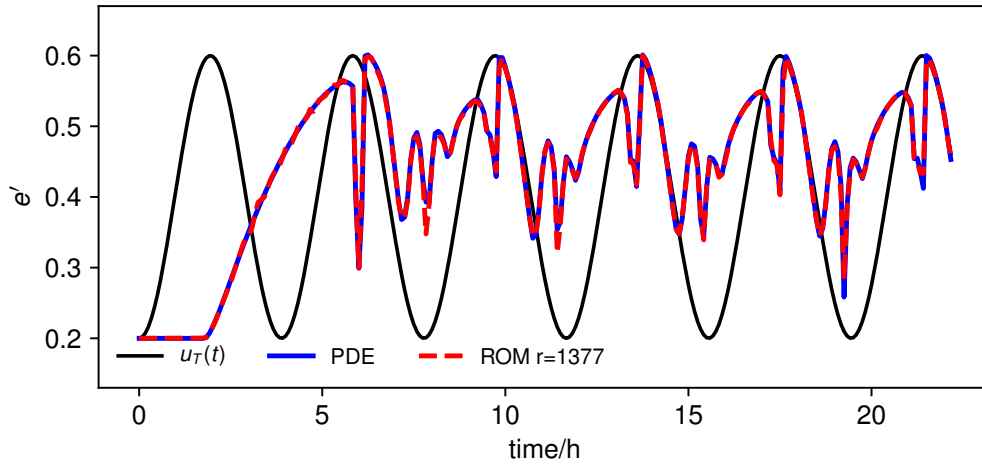


Figure 5.11: Comparison of the PDE solution to the ROM including a reduction of all subnetworks for RND at consumer (b) in fig. 5.7. The black solid line presents the corresponding in-sample input signal.

5.5 Conclusions

In this chapter the reduced order model resulting from the Galerkin projection proposed in chapter 4 was analyzed numerically. The full order DAE results from the solenoidal transport of energy density in which mass density and friction coefficient

are modeled as global constants. The contribution of acceleration in the momentum balance of the Euler-like equations was neglected. The surrogate model allows for a speed up of up to one order of magnitude compared to full order hyperbolic schemes in the error range of interest. An adaptive, implicit Runge-Kutta scheme achieves the best results among the studied time integration schemes. Runtime and error of the reduced order model are evaluated for both the training data used to generate the ROM and an out-of-sample signal, differing from the training signal. Computational benefits are shown for two existing heating networks, including a large scale network. The latter exhibits highly demanding changes of flow directions in its dynamics, which are a central difficulty in modeling and simulating heating networks. Employing a network decomposition prior to the application of the Galerkin projection is responsible for a significant decrease in simulation time, due to a more efficient assembly of the reduced operators $A_r(q)$, $B_r(q)$. In addition, the dimension of the reduced order model decreases the computational complexity even further. Concerning the decomposition strategy, two approaches were compared. In the first, the subnetwork allowing for changes of flux direction SNF is reduced as a separate subnetwork. In the second, a hybrid approach was used, in which SNF remains as a full order subnetwork. For the purpose of a forward simulation, both approaches yield comparable results concerning runtime and approximation error.

Chapter 6

Optimal control of heating networks using reduced order models

In this chapter an optimal control problem for district heating networks is solved using the reduced order model suggested in chapter 4. The objective is to minimize the temporal variation and absolute value of the energy density supplied by the power plant while fulfilling a constraint to the maximum injected feed-in power. The corresponding optimization problem is solved using the MATLAB[®] function `fmincon`. Instead of imposing the transport dynamics as optimization constraints, the dynamics are solved explicitly using the reduced order model and the results are passed to the optimizer. Employing this strategy, full- and reduced order model are compared for three different test scenarios.

6.1 Optimization objectives of heating networks

Heating networks are of particular interest for low-carbon energy supply due to their flexibility in using different sources of energy [2, 3]. The energy density u_T injected at a power plant is guided to consumers of different sizes using a network of pipelines referred to as flow network. At the consumers, the local volume flow is regulated using heat exchangers to match the time dependent power consumption G given the currently available energy density e . Fig. 6.1 illustrates an existing large scale network considered in this contribution. Its outline data is supplied in tab. 5.1. A central aim of operating these networks lies in efficiently planning the input energy density u_T . It defines the power feed-in $P = (u_T - e_R)q^\Sigma$ in combination with the aggregated volume flow q^Σ , and the energy density of the cooled fluid e_R entering the plant in the return network. Due to the high transport times from source to consumption in large scale networks, the power feed-in $P(t)$ at each point of time t needs not to match the current power consumption G at the heat exchangers. While both quantities are coupled by conservation of energy within the heating network, there exists an essential optimization potential in distributing u_T over time. Injecting a high energy density in times of large volume flows q^Σ requires firing additional vessels which might be unfavorable for economic and ecological reasons. Vice versa, planning might also

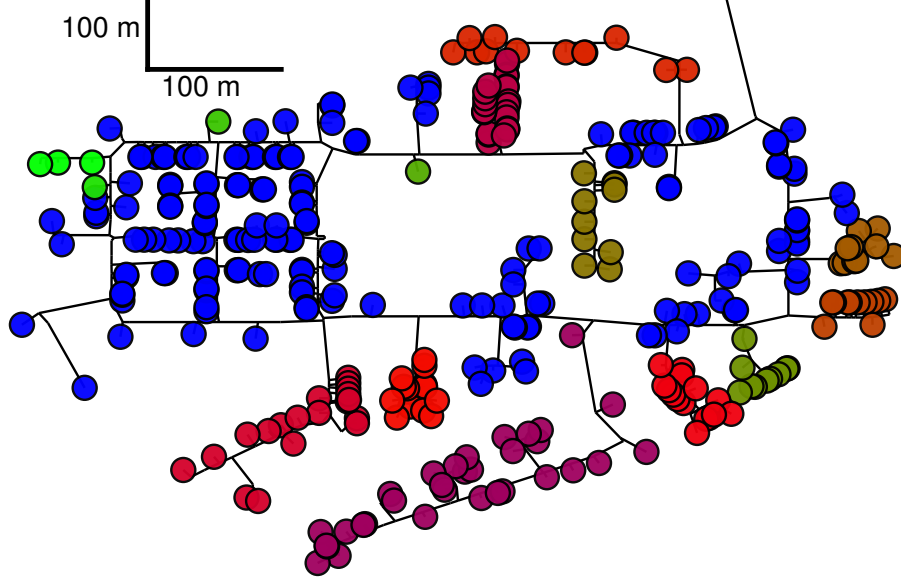


Figure 6.1: Topology of an existing heating RND network supplying a district. The network is decomposed to a main network (dark-blue circles) and 14 sub-networks. Pipelines changing flux direction are part of the main network.

enable to use external overcapacities of energy resulting from renewable energies. In the specific application, a waste to heat incineration plant is able to deliver power up to a maximum level at no cost. When exceeding this level for only a short time interval, significant costs result from using gas boilers to cover peaks in the injected power.

In the optimization task, the dynamical energy transport on these complex networks is an essential constraint to ensure a physically relevant control and requires a significant amount of computation time. Since controls of power plants are updated every 15 min in application, the corresponding optimization needs to be sufficiently fast. To this end, the usage of reduced order models is central [105, 76, 106]. For network systems, both tasks of defining an optimal control [107], as well as formulating reduced order models are complex. Due to their mathematical complexity and the large benefits, the optimization of energy networks such as electric [4], water [6], gas and heating networks is an active field of research. Concerning the model order reduction of energy systems, different works already exist for gas networks [26, 108], electric networks [62] and other applications [109]. Similarly, many publications focus on the optimization of gas networks [7, 10, 6, 18, 8, 9]. While gas networks are modeled by compressible Euler equations, the transport fluid for heating networks is water in the fluid phase inducing incompressible dynamics. On the one hand this simplifies the equations for the conservation of mass and momentum significantly. On the other hand, for heating networks the conservation of inner energy describing the dynamical transport of thermal energy is the dominant effect and mathematically the most challenging one. It leads to a time-dependent advection of the injected thermal energy yielding a large,

dynamically changing delay in the energy transport between source and consumption. Towards the formulation of a reduced order model, advection on network systems is a demanding problem.

Selected works discussing the optimal control of heating networks are mentioned subsequently. In [13], pumping costs resulting from the variation of pressure and massflow are optimized using a reduced order model without reflecting the dynamically changing thermal transport. In [11], a predictive controller is formulated. The advection of thermal energy is reflected by the method of characteristics on each pipeline assuming a constant time delay between source and households. In [12] the transport of thermal energy from source to each consumer is described by virtual single pipelines including a constant time delay from source to consumption points. The design of the district heating network is itself an interesting optimization task. In [14], the authors optimize the investment and operation costs over 30 years, formulating a mixed integer non-linear programming model based on steady states. In this contribution, the topology is fixed and visualized in fig. 6.1. Similar to the approach used for gas networks, a model very close to the underlying Euler equations is formulated, allowing to precisely model the thermal transport dynamics and addressing the central difficulties of heating networks. These are dynamically changing delay times from source to consumers, as well as changes of flux direction. Using a system theoretic approach to model the dynamics allows to use effective tools from model order reduction.

6.2 Model assumptions

The model used to derive optimal control strategies bases on the full DAE (3.27) discussed in section 3.1.5 and is summarized subsequently. It differs from the model analyzed in chapter 5 in three ways. First, pipeline dependent friction factors are considered and second, the power consumption at consumer stations is modeled by time-dependent standardized profiles. Third, the pressure levels at every heat exchanger are evaluated after the each simulation of the dynamics. For the continuous time interval $t \in \mathcal{T}_c = [t_0, t_e] \subset \mathbb{R}^+$ the corresponding model reads

$$\dot{e} = A(q)e + B(q)u_T, \quad e(t_0) = e_0, \quad (6.1a)$$

$$y = Ce, \quad (6.1b)$$

$$Kq = 0, \quad (6.1c)$$

$$\Phi_\alpha v_\alpha = q_\alpha \quad \alpha \in \mathcal{P} \quad (6.1d)$$

$$G_a - q_a(e_{a:k} - e_R) = 0, \quad a = (k, m) \in \mathcal{C}, \quad (6.1e)$$

$$\sum_{\alpha \in \xi} \frac{\lambda_\alpha L_\alpha}{2d_\alpha} v_a |v_\alpha| = 0, \quad \xi \in \mathcal{L}_\mathcal{G}, \quad (6.1f)$$

$$\frac{\rho \lambda_\alpha L_\alpha}{2d_\alpha} v_a |v_\alpha| + \rho g L_\alpha (z_m - z_k) = -(p_m - p_k), \quad \alpha = (k, m) \in \mathcal{P} \quad (6.1g)$$

$$p_{s:m}(t) = p_{s:k}(t) + \Delta p_s(t), \quad s = (k, m) \in \mathcal{S}, \quad (6.1h)$$

$$p_{s:k}(t) = p_R(t), \quad s = (k, m) \in \mathcal{S}. \quad (6.1i)$$

Eqs. (6.1) base on the control system (3.27) discussed in section 3.1.5, with certain assumptions to the equations of state and the determination of the friction factor explained subsequently. Eq. (6.1a) describes the solenoidal transport of energy, including the conservation of energy at network nodes. Additional, the conservation of volume is claimed (6.1c). In the flow defining equations (6.1e, 6.1f) the mass density $\rho = 10^3 \text{ kg m}^{-3}$ is assumed to be globally constant, and the contribution of acceleration is neglected. The friction factor λ_α , $\alpha \in \mathcal{P}$ is constant in time but in contrast to chapter 5 depends on the diameter of each pipelines. It is defined by the Colebrook-White equation (2.5) for a fixed Reynolds number $\text{Re} = 10^6$ and a roughness of $\sigma = 0.047 \text{ mm}$. The high Reynolds number ensures to determine a friction coefficient in the turbulent regime. Since a constant density is assumed, both the density and the sum over height differences cancel from the flow-defining equations of Kirchhoff type, resulting in (6.1f). The consumption profile of each consumer exhibits an identical energy density in the return part (6.1e). The pressure change along pipeline α (6.1g) is determined according to the momentum balance of the Euler-like equations, as explained for (6.1f). Eqs. (6.1f) are used to solve for the flow field and thus are presented in the above model, although they formally are a consequence of (6.1g). Since the return energy densities at consumer stations are identical, and thermal losses by conduction to the pipeline wall are neglected, the return network is not included the simulation model. The controllable pressure levels at flow- and return part of the power plant defined in (6.1h, 6.1i) will be collected in u_p .

Eqs. (6.1) refer to the full order model. The reduced order model is obtained by replacing (6.1a - 6.1b) with its Galerkin projection

$$\dot{e}_r = V^T A(q) V e_r + V^T B(q) u_T, \quad e(t_0) = e_0 \quad (6.2a)$$

$$y_r = C V e_r, \quad (6.2b)$$

as described in section 4.5. Full- and reduced system operators are formed as in chapter 5,

$$A(q) = Q^{\frac{1}{2}} \left(\sum_{\nu=1}^{n_q} \gamma_{\nu}^{\tilde{q}}(q) A_{\nu}^{\tilde{q}} \right) Q^{-\frac{1}{2}}, \quad B(q) = Q^{\frac{1}{2}} \left(\sum_{\nu=1}^{n_q} \gamma_{\nu}^{\tilde{q}}(q) B_{\nu}^{\tilde{q}} \right), \quad (6.3a)$$

$$A_r(q) = V^T A(q) V, \quad B_r(q) = V^T B(q), \quad C_r = C V. \quad (6.3b)$$

The corresponding projection matrix V is obtained by alg. 2, 3, using the reference parameters described in section 5.2. A modification of the reference parameters is done for the values $\bar{\delta} = 2 \times 10^{-2}$, $\bar{\Delta} = 5 \times 10^{-2}$. The number of initial interpolation points is set to $r = 4$. The latter are set along the positive part of the imaginary axis. Precisely, the interpolation points are distributed logarithmically between $10^{-7}i$, and 10^0i . An increment of 2 is applied for initializations of IRKA which do not meet the desired error $\bar{\delta}$. The order of allowed singular value decays is set to $s \in [8..14]$. To sample from the Pareto frontier resulting from alg. 3, the projection matrix leading to the smallest reduced order model was used, which satisfies the error indicator $\bar{\Delta}$.

6.3 Control problem

For the set of discrete points of time $\mathcal{T}_d = \{t_0, \dots, t_e\}$, and the corresponding continuous interval $\mathcal{T}_c = [t_0, t_e]$ we seek at determining a parameterized control $u_T^{\kappa} : \mathcal{T}_c \mapsto \mathbb{R}$ of the input energy density, minimizing the following objective within $t \in \mathcal{T}_d$

$$\mathcal{J}(u_T^{\kappa}) = \eta_1 \|\dot{u}_T^{\kappa}(\cdot)\|_{l_2(\mathcal{T}_d)}^2 + \|u_T^{\kappa}(\cdot) - \eta_2\|_{l_2(\mathcal{T}_d)}^2, \quad (6.4)$$

subject to, $t \in \mathcal{T}_d$,

$$u_T^{\kappa}(t) \leq \bar{u}, \quad (6.5)$$

$$e_{a:k}(t) \geq \bar{e}, \quad a = (k, m) \in \mathcal{C} \quad (6.6)$$

$$p_{a:k}(t) \leq p_h^{\max}, \quad a = (k, m) \in \mathcal{C} \quad (6.7)$$

$$p_{a:k}(t) \geq p_h^{\min}, \quad a = (k, m) \in \mathcal{C} \quad (6.8)$$

$$(u_T^{\kappa}(t) - e_R) \sum_{a \in \mathcal{C}} q_a(t) \leq \bar{P}, \quad (6.9)$$

$$D(\dot{e}, e, e_0, q, p, u_T^{\kappa}, \Gamma) = 0. \quad (6.10)$$

The objective function (6.4) penalizes the temporal variation and the distance to the regularization parameter η_2 of the parameterized control u_T^{κ} . The regularization parameters η_1, η_2 are used to equalize both contributions in the objective which are

motivated as follows. Minimizing the temporal variation leads to realistic controls, which can be realized properly by the power plant. In addition, high temperature gradients harm the pipeline material mechanically. By choosing η_2 sufficiently small, the mean value of the control decreases which systematically reduces thermal losses by cooling effects. Decreasing the injected energy density will lead to higher pressures in the network, which are restricted as explained below. Constraints (6.5 - 6.8) are technical restrictions in line with standard operation instructions formulated as optimization constraints. The upper energy limit $\bar{u} = \min(e(T_{max}^F), e(T_{max}^{\text{net}}))$ in (6.5) reflects both the maximal temperature allowed in the network and at consumer stations, forcing the fluid to remain in the liquid phase. By conservation of energy, energy densities realized in the network can never exceed u_T . Since thermal losses are not considered, the input energy density will eventually be realized at the consumer stations. Consequently, it is sufficient to pose the upper temperature limit at the power plant. In (6.6) a minimal energy density is required for proper operating conditions of the heat exchangers, reflecting both the minimal energy density at the flow part of consumer stations (2.12e) and the minimal temperature difference from flow to return temperatures (2.12f). In addition, the pressure levels of consumption nodes in the flow network are restricted to upper and lower bounds (6.7, 6.8). As presented in section 2.1.4, there exist additional pressure constraints for the absolute pressure levels at the return part of consumer stations, as well as for every node in flow- and return network. These constraints are considered indirectly by choosing appropriate pressure bounds (p_h^{\min}, p_h^{\max}) as discussed below. Eq. (6.9) sets an upper bound to the maximal injected power, which avoids the use of additional energy sources. Below this limit, the power plant can supply demands by energy stemming from a waste to heat incineration plant at no costs. Due to the transport time of the injected energy from source to consumers, the control has a delayed effect on the consumer, allowing to influence the temporal distribution of the injected power. Finally, (6.10) reflects the energy transport (6.1a) along the network restricted by the algebraic coupling conditions (6.1c - 6.1g) and the initial state $e_0(u_T^K)$. The boundary conditions stored in Γ are given by

$$\Gamma := (u_p, G, e_R)^T.$$

For the full order model (6.10) is given by (6.1). In the reduced order case, (6.1a - 6.1b) are replaced by (6.2) respectively.

The consumption G is assumed to be known a-priori, which is a typical assumption in the simulation of heating networks. Since cooling effects are neglected and the energy densities in the return network are modeled equal and constant, an open loop control problem results. The return network exhibits a constant energy density e_R entering the feed-in power (6.9) as a parameter.

The required pumping power P_{hyd} necessary to retain a fluid flow in the network is stemmed by the pumps in the depot. It is bounded above as follows,

$$P_{\text{hyd}}(t) = \Delta p_s(t) \sum_{i \in \mathcal{C}} \frac{G_i(t)}{e_{i:k}(t) - e_R}, \quad i = (k, m) \in \mathcal{C}, \quad (6.11a)$$

$$\leq \frac{\max_{t \in \mathcal{T}_c}(\Delta p_s(t))}{\min_{t \in \mathcal{T}_c} e(t)} \max_{t \in \mathcal{T}_c} \sum_{i \in \mathcal{C}} G_i(t), \quad (6.11b)$$

where Δp_s describes the pressure difference achieved at the source edge representing the depot. For typical networks, the maximum pressure difference at the depot is smaller than 10 bar. Approximating the energy density by $e \approx \rho c_p T$, with material constants described in section 6.5.2, a maximum aggregated power consumption of 1 MW leads to a corresponding pumping power of 16 kW. Thus, the pumping power is suppressed by almost two orders of magnitude compared to the thermal power.

Treatment of pressure constraints

Subsequently, we explain how to fulfill the pressure constraints (6.7, 6.8) in a simplified manner. Incorporating different additional pressure constraints by defining effective values for p_h^{\min} , p_h^{\max} is addressed afterwards. Simplifying constraints (6.7, 6.8) relies on limiting the difference of the maximum and minimum pressure levels measured at all consumption points. This allows to adjust the pressure control $u_p : \mathcal{T}_c \mapsto \mathbb{R}$ after finding the optimal control of the energy density.

By (6.1g), the pressure difference from source $s = (k_s, m_s)$ to consumption point $h = (k_h, m_h) \in \mathcal{C}$ is defined by

$$\Delta p_h \equiv p_{h:k_h} - p_{s:m_s} = \rho g(z_{s:m_s} - z_{h:k_h}) - \rho \sum_{i \in K_h} \lambda_i \frac{L_i}{2d_i} v_i |v_i|, \quad (6.12)$$

where K_h denotes an arbitrary path from the source to consumer $h \in \mathcal{C}$. Although the pipeline velocities change dynamically, diameters, lengths and the height profile on the path from source to each consumer station determine the resulting pressure difference to a large extent. This stabilizes the constraint limiting the maximum pressure difference. For simplicity of notation, we abbreviate the pressure levels at the flow node of the source edge and the flow nodes of consumer stations by

$$p_s := p_{s:m}, \quad s = (k, m) \in \mathcal{S}, \quad p_h := p_{h:k}, \quad h = (k, m) \in \mathcal{C}.$$

This allows to formulate the following proposition.

Proposition 15. *The pressure constraints (6.7, 6.8) are satisfied by defining an alternative constraint on the difference of the maximum and minimum pressure realized at all consumption points,*

$$\max_{h \in \mathcal{C}}(\tilde{p}_h(t)) - \min_{h \in \mathcal{C}}(\tilde{p}_h(t)) \leq \overline{\Delta p}, \quad t \in \mathcal{T}_d, \quad (6.13)$$

where \tilde{p}_h denotes the pressure level at consumption point h valid in a simulation with an arbitrary source pressure \tilde{u}_p . Here, $\overline{\Delta p} \leq p_h^{\max} - p_h^{\min}$ is the true limit for the pressure difference entering the alternative optimization constraint (6.13). The control of the pressure level leading to admissible pressures at consumption points is obtained a-posteriori by a time dependent shift,

$$u_p(t) = p_h^{\min} - \min_{h \in \mathcal{C}}(\Delta p_h(t)) \quad t \in \mathcal{T}_d. \quad (6.14)$$

Proof. By limiting the difference between maximal and minimal absolute pressure levels in (6.13), their value relative to the pressure control is limited as well,

$$\max_{h \in \mathcal{H}}(\tilde{p}_h - \tilde{u}_p) - \min_{h \in \mathcal{C}}(\tilde{p}_h - \tilde{u}_p) = \max_{h \in \mathcal{C}}(\Delta p_h) - \min_{h \in \mathcal{C}}(\Delta p_h) \leq p_h^{\max} - p_h^{\min}, \quad (6.15)$$

where Δp_h denotes the pressure difference from house to source, which is independent of the pressure control at the source by (6.12). Thus, the pressure level at each consumption point for an arbitrary source pressure p_s reads,

$$p_h = p_s + \Delta p_h.$$

Inserting the suggested control (6.14) allows to determine the minimum pressure at each consumption point by

$$\min_{h \in \mathcal{H}}(p_h) = p_s + \min_{h \in \mathcal{H}}(\Delta p_h) = p_h^{\min} - \min_{h \in \mathcal{H}}(\Delta p_h) + \min_{h \in \mathcal{H}}(\Delta p_h) = p_h^{\min}.$$

Similarly, the maximum pressure level is limited by

$$\begin{aligned} \max_{h \in \mathcal{H}}(p_h) &= p_s + \max_{h \in \mathcal{H}}(\Delta p_h) \\ &= p_h^{\min} - \min_{h \in \mathcal{H}}(\Delta p_h) + \max_{h \in \mathcal{H}}(\Delta p_h) \\ &\leq p_h^{\min} + p_h^{\max} - p_h^{\min} \\ &= p_h^{\max}, \end{aligned} \quad (6.16)$$

where the inequality in (6.16) is obtained by using (6.15). \square

Additional pressure constraints

Proposition 15 describes how to exactly fulfill the constraints (6.7, 6.8). Instead of checking $2|\mathcal{C}|$ constraints at each time $t \in \mathcal{T}_d$, only a single constraint has to be checked. In addition, there exist global pressure constraints on all network nodes as well as for the pressure difference at each consumer stations, cf. tab. 6.1, and the technical restrictions [35]. Checking these explicitly would lead to additional $N + |\mathcal{C}|$ constraints at each time $t \in \mathcal{T}_d$, increasing the complexity of the optimization task significantly. As an alternative, we adjust (p_h^{\min}, p_h^{\max}) to achieve an approximation to the remaining pressure constraints. By assuming a symmetric topology of flow- and return network, a constraint limiting the pressure difference at consumer stations

in the flow part of the network will also limit the pressure range at the return part of consumer stations by $\overline{\Delta p}$. Furthermore, it is assumed that consumer stations are distributed sufficiently dense along the network to avoid evaluating pressure levels of the nodes not covered by consumer stations. Using these assumptions, the choice $p_h^{\min} = 6.6$ bar, $p_h^{\max} = 9.1$ bar, $\overline{\Delta p} = 2.5$ bar approximates a realistic pressure scenario.

p_{min}^F	p_{min}^F	p_{min}^R	p_{max}^R	Δp_{min}^c	Δp_{max}^c
4.3 bar	9.1 bar	3.5 bar	8.3 bar	0.8 bar	5 bar

Table 6.1: Pressure restrictions at consumer stations for the network RND.

Feed-in power and control of energy density

The feed-in power is the central constraint to limit additional costs, since it avoids the usage of additional energy resources. It is defined by

$$P = (u_T^\kappa(t) - e_R) \sum_{i \in \mathcal{C}} q_i(t) \quad (6.17)$$

$$= (u_T^\kappa(t) - e_R) \sum_{i \in \mathcal{C}} \frac{G_i(t)}{e_{i:k}(t) - e_R}, \quad i = (k, m) \in \mathcal{C}. \quad (6.18)$$

The control u_T^κ affects the feed-in P (6.17) in two ways. First, by setting the current input energy density u_T^κ and second, by defining the volume flow which results from the current energy densities at heat exchangers. These in turn equal the control $u_T^\kappa(\tau)$ at a past time τ . Depending on the current state e_{h,n_h} at consumer stations, the input control can both amplify and weaken the feed-in power with regard to the current consumption G . In the stationary case $e = u_0$, where u_0 denotes the constant input, the feed-in power is the temporally shifted consumption profile. Hence, it also matches the high characteristic power peaks in the morning and the evening hours. In contrast, by anticipating the expected consumption and the transport time of the injected power, peaks in the injected power can be reduced. Since the determination of an optimal control is initialized with a constant temperature, the red, solid lines in parts (b) of fig. 6.2, 6.4, 6.5 visualize the consumption profile equaling the displayed feed-in.

6.4 Determination of an optimal control

Subsequently, we discuss the computation of an optimal control for the problem (6.4-6.10). The main idea is to eliminate the transport dynamics from the optimization constraints by solving them explicitly and passing the remaining constraints to the MATLAB nonlinear optimization tool `fmincon`.

Supplying an initial control which satisfies all constraints is an open problem. Hence, the initial parameter set κ_0 generally at least violates the feed-in constraint (6.9) and the determination of a feasible solution is performed initially. For the current parameter vector κ_i , the transport dynamics described by the DAE (6.10) are solved along \mathcal{T}_d . In the solution process, both the trajectory of state variables and their parameter gradients are calculated. This allows to evaluate the true optimization constraints (6.5 - 6.6, 6.9, 6.13), and their gradients with respect to the current parameter κ_i . In this step, the limits for the pressure levels (6.7, 6.8) are replaced by (6.13) as described in proposition 15. This allows to focus on the determination of the thermal control $u_T^{\kappa_i}$ in solving the optimal control problem. The required pumping power resulting from the pressure control u_p can be neglected as described in section 6.3. Solving the dynamics explicitly avoids the large computational cost of passing them as optimization constraints. Values and gradients of the optimization constraints for the current parameter are passed to `fmincon` using the active set method together with the value and parameter of the objective function (6.4). A summary of the algorithm used to determine the optimal control is provided in alg. 5.

Algorithm 5 Numerical computation of an optimal control

Require: Initial parameter set κ_0 , convergence tolerance of nonlinear optimization.

- 1: **while** convergence tolerance not satisfied **do**
- 2: Solve DAE (6.10) using the implicit midpoint rule (6.21) for the current parameter vector κ_i .

$$D(\dot{e}, e, e_0, q, p, u_T^{\kappa_i}, \Gamma) = 0, \quad t \in \mathcal{T}_d.$$

- 3: Determine constraints K defined in (6.5-6.6, 6.9, 6.13), and their parameter gradients $\partial_{\kappa_i} K$ based on the solution of (6.10).
 - 4: Evaluate objective function $\mathcal{J}(u_T^{\kappa_i})$ defined in (6.4) and its gradient $\partial_{\kappa_i} \mathcal{J}(u_T^{\kappa_i})$.
 - 5: Update parameter $\kappa_{i+1} \leftarrow \text{fmincon}(\mathcal{J}(u_T^{\kappa_i}), \partial_{\kappa_i} \mathcal{J}(u_T^{\kappa_i}), K, \partial_{\kappa_i} K)$.
 - 6: **end while**
 - 7: Adjust pressure control u_p according to proposition 15.
-

Extraction of parameter gradients

To estimate the effect of a change in the parameterized control on the relevant outputs of the heating networks, the sensitivities of both the objective function and the constraints with respect to the parameters have to be determined $\forall t \in \mathcal{T}_d$. To this end, gradients of both the control and state variables regarding the control parameters have to be extracted from the forward solution of the DAE (6.10). For the input signals typically applied to heating networks, an implicit time integration of the DAE proved

to be beneficial. A general implicit time integration scheme, in which x_μ and $x_{\mu+1}$ denote the state variables at former and future time levels can be written as

$$\tilde{f}(x_\mu, x_{\mu+1}, u) = 0. \quad (6.19)$$

The derivative of the future state variable $\partial_\kappa x_{\mu+1}$ is obtained by the derivative of the old state variable $\partial_\kappa x_\mu$ using the implicit function theorem,

$$\partial_\kappa x_{\mu+1} = - \left(\frac{\partial \tilde{f}}{\partial x_{\mu+1}} \right)^{-1} \left((\partial_{x_\mu} \tilde{f}) \partial_\kappa x_\mu + \partial_u \tilde{f} \partial_\kappa u \right). \quad (6.20)$$

Hence, based on the sensitivity of the initial state $\partial_\kappa e_{\alpha,\beta}(t_0)$, the gradient information can be propagated along the solution of the DAE. Using (6.20) allows to determine the gradient *after* solving for the new time step. This is in contrast to many automatic differentiation approaches in which the gradient information has to be tracked during the determination of the future time layer causing additional computational cost.

For the time integration of the DAE in this contribution, the implicit midpoint rule as a second order symplectic integrator is used,

$$\tilde{f}(x_\mu, x_{\mu+1}, u) = x_{\mu+1} - x_\mu - \text{dt} f \left(t_\mu + \frac{\text{dt}}{2}, \frac{1}{2}(x_\mu + x_{\mu+1}), u \right), \quad (6.21)$$

where dt denotes the time step, and f the dynamical part of the DAE (6.10).

6.5 Numerical validation

6.5.1 Time integration of the DAE

The solution of the forward problem (6.10) within the determination of an optimal control is performed by the system descriptions (6.1, 6.2). To solve these DAEs within the time horizon required for the optimal control, the implicit midpoint-rule (6.21) is used. Full order models are unreduced ($W = V = 1$), while for the reduced order model a Galerkin projection is applied. Sparse matrix operations are considered in the full order case. To solve systems (6.1,6.2) efficiently, a domain decomposition is performed [110]. Different parts of the network are treated as independent systems, with their linkages moderated by artificial inputs. This accelerates the formation of the system operators and the solution of the nonlinear equations introduced by the implicit time integration scheme. Full and reduced order models are simulated using the decomposition presented in fig. 6.1 including a main- and 14 subnetworks. In this chapter, pipelines undergoing changes of flux directions are included in the main network. Consequently, the Galerkin projection calculated for the main network also includes configurations in which certain pipelines change their flow direction. Compared to the hybrid approach, in which the resulting reduced order dimension remains

high by containing an unreduced subnetwork, reducing the entire network minimizes the reduced order dimension which is favorable when determining and using the Jacobian. Due to the affine system representation, the determination of the Jacobian can be determined analytically for both full- and reduced order models. The simulations presented in the following sections are performed using MATLAB[®]R2016b on an Intel[®]XEON[®]CPU E5-2670 processor @ 2.60GHz. The nonlinear system of equations resulting from both the algebraic equations and the time integration scheme are solved using the MATLAB[®]function `fsolve`.

6.5.2 Definition of test scenarios

To demonstrate the effectiveness of the reduced order model, the large-scale heating network presented in fig. 6.1 is studied. The cycles visible in the left part of the network pose a central difficulty since the thermal transport can take different paths at the same time to reach a certain destination in the network. Moreover, changes of flux direction occur, which change the set of possible paths the transported quantity takes dynamically.

The robustness of the reduced model towards its application in the optimization is evaluated for different environmental temperatures defining the consumption behavior for the large scale network. These scenarios cover the relevant mean daily temperatures $\{-3, 3, 7.5\}$ °C. The interval spanned by $[-3, 7.5]$ °C exhibits a large optimization potential in terms of distributing the feed-in power. For colder or warmer environmental temperatures, either all or none of the energy capacities within the power plant will be used. The lower and upper temperature constraints are in line with standard operation conditions of heating networks. Tab. 6.2 presents a detailed description of the optimization scenarios under investigation. The observation interval, in which the

$T_{\min}^{\text{cons}}, T_{\max}^{\text{net}} / ^\circ\text{C}$	$p_h^{\min}, p_h^{\max}, \overline{\Delta p} / \text{bar}$	\bar{P}	$T_d / ^\circ\text{C}$	$t_0, t_e / \text{h}$	dt / s
75, 110	6.5, 9.1, 2.5	$0.5(\hat{G} + G_0)$	-3, 3, 7.5	0, 72	300

Table 6.2: Description of the considered optimization scenarios. Test cases TC1-TC3 differ by the considered daily mean temperature changing from -3°C to 7.5°C . $T_{\min}^{\text{cons}}, T_{\max}^{\text{net}}$ denote the temperature equivalents of the optimization constraints (6.5, 6.6).

constraints and the objective function are evaluated, is set to $\text{dt} = 300 \text{ s}$, which is smaller than the typical plant operation interval of 900 s . This allows to approximate the underlying dynamics more precisely, while matching the relevant decision interval. The power constraint $\bar{P} \in [G_0, \hat{G}]$ is chosen within the mean (G_0) and maximum (\hat{G}) daily consumption. While the mean consumption G_0 naturally poses a lower limit for the maximum injected power, the maximum consumption \hat{G} is an upper limit, since it can always be achieved by a stationary control. Due to the initialization with a stationary solution, during the first period the power restriction is relaxed to the

maximum consumption. During this time, the output energy density and the corresponding constraints are shaped by the initial solution and not the control. The difference of maximal and minimal pressure levels at all consumption points in the flow network is given by $\overline{\Delta p} = 2.5$ bar and replaces the optimization constraints (6.8, 6.7).

For the gravitational constant we use a value of $g = 9.81 \text{ m s}^{-2}$. Specific heat capacity and density are set to $c_p = 4.16 \text{ kJ K}^{-1} \text{ kg}^{-1}$, and $\rho = 1000 \text{ kg m}^{-3}$. To transform energy densities to temperatures presented in the section, we use the approximation

$$e \approx \rho c_p T. \quad (6.22)$$

This allows to transform the constraints for the minimum energy density at consumer stations (6.6), as well as the maximum energy density in the network (6.5) to their corresponding temperature values T_{\min}^{cons} , and T_{\max}^{net} displayed in tab. 6.2.

The power extraction G is modeled using demand profiles typically employed in the simulation of heating networks [111]. Specifically, each heat exchanger exhibits the power demand

$$G_i(t) = c_i s_{m(i)}(t, T_d), \quad i \in \mathcal{C}, \quad t \in \mathcal{T}_c. \quad (6.23)$$

The customer specific scaling factor c_i represents an estimate for the total daily energy demand. The profile $s_m(t, T_d)$ models the time dependent demand for a given consumption class m and the daily mean environmental temperature T_d . Every member of the class thus shares the same normalized profile while exhibiting an own specific consumption. The available demand profiles adjust the daily consumption by hourly scaling factors. The latter also depend on T_d , adjusting the relative weights of each hour in the daily consumption. Based on these hourly values, a spline interpolating the consumption is generated. In the considered network, the largest part of consumers belongs to the same consumption class s_0 . To this end, all consumers are modeled by this class.

Since the typical consumption follows a periodic profile if the daily mean environmental temperature does not change, the control u_T^κ is parameterized by a Fourier series,

$$u_T^\kappa(t) = c_0 + \sum_{k=1}^K c_k \cos(k\omega t) + \sum_{k=1}^K s_k \sin(k\omega t), \quad (6.24)$$

which approximates any control $u \in L_2$. Here, the frequency $\omega = 2\pi/\theta$ is fixed to the period length θ of the consumption signal corresponding to 24 h. The remaining Fourier coefficients act as parameters to be optimized.

6.5.3 Numerical controls obtained by full and reduced order model

Subsequently, different spatial discretizations are used to determine an optimal control. To check for feasibility of the solution, the suggested optimal controls resulting from

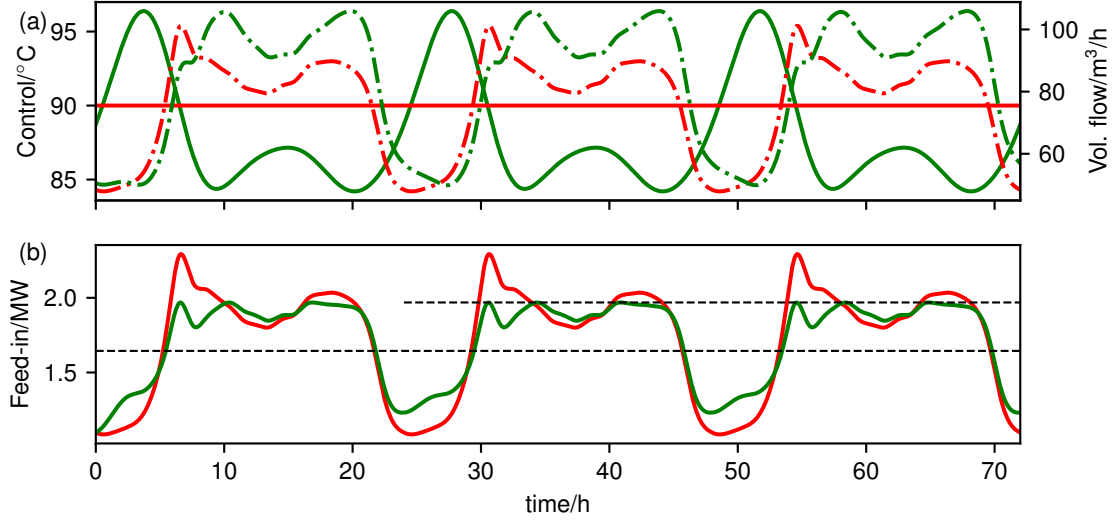


Figure 6.2: Optimal control problem for TC1 at -3°C comparing the initial control (red) to the optimized control (green), obtained by the reduced model ROM1. Part (a) shows controls (solid lines) and the total volume flow injected at the power plant (dashed lines). Part (b) presents the feed-in power for both controls together with the mean consumption (lower dashed line) and the feed-in constraint \bar{P} (upper dashed line).

both full- and reduced order models are compared and validated using a reference discretization FOMR. The latter is given by an upwind discretization in space with a high number of finite volume cells. This will answer the question, whether a coarse, unreduced model is appropriate for an optimization task as well. FOM0 denotes the minimal upwind discretization, in which each pipeline receives one finite volume cell. FOM1 is a finer discretization, with small approximation errors compared to FOMR. Finally, ROM1 is the reduced order model obtained by reducing the discretized model FOM1 cf. tab. . 6.3. Before comparing runtime and optimal controls obtained by different spatial discretizations, we analyze the optimal control suggested by ROM1.

The discussion of the numerical optimization results starts with TC1 simulating a mean daily temperature of -3°C with a mean and maximum consumption of 1.64 MW, and 2.29 MW. Based on a constant initial control of 90°C , avoiding high feed-in peaks forces the control to increase its temporal variation, cf. fig. 6.2(a). The resulting feed-in power fulfills the power constraint, while the limit is attained at several points of time cf. fig. 6.2(b). Since the mean temperature changes only slightly, the resulting total volume flow injected at the power plant also remains on the same level compared to the initial control, cf. fig. 6.2(a). The suggested temporal variation of the thermal control which is necessary to limit the feed-in power induces pre-heating effects, visualized in fig. 6.3. Thus, reflecting the transport delay from source to the sink, in certain time intervals marked in red, the injected feed-in power exceeds the current consumption. More specifically, the maximum temperature level is injected at the power plant before the maximum aggregated consumption occurs at the consumption

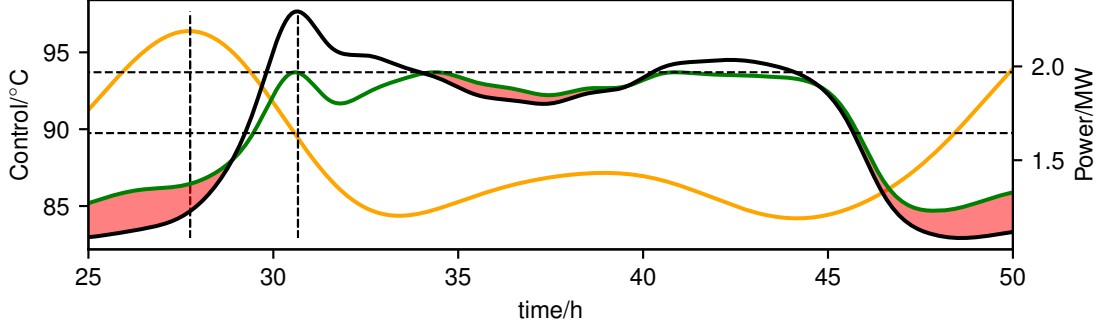


Figure 6.3: Result of the optimal control problem for TC1 at -3°C visualizing the control at the power plant (orange) leading to a feed-in power (green) below the maximum constraint (upper dashed line). Red areas indicate regions in which pre-heating happens: The feed-in power exceeds the current consumption (solid, black line). Vertical, dashed lines visualize the time difference between the maximum injected temperature and the maximum consumption. The lower, dashed line indicates the mean consumption during one day as a guide for the eye.

points. A common feature of the standardized consumption profiles are peak consumption around 6 a.m. and 6 p.m. Indeed, two pre-heating phases can be observed reflecting these two phases of high consumption, cf. fig. 6.3. To avoid finite horizon effects, in which the suggested optimal control exploits the energy incorporated in the initial state, the setup is simulated for three periods of 24 hours. Focusing on the injected power coupling to volume flows at consumer stations as state variables, a state close to periodicity is reached quickly.

	FOM 0	FOM 1	ROM 1	FOMR
runtime opt./s	2765.0	2640.0	608.5	16100.0
runtime sim./s	2685.0	2585.0	557.0	15900.0
# solves DAE	16	9	11	12
DOF	775	1789	180	9538
$\mathcal{J}(u)$	55.9	53.0	52.9	52.6
$\ u - \tilde{u}\ _2 / \ \tilde{u}\ _2$	8.10×10^{-3}	9.48×10^{-4}	7.25×10^{-4}	0
$\ P - \bar{P}\ _{\max} / \bar{P}$	5.41×10^{-3}	4.60×10^{-4}	4.49×10^{-4}	0
$\max_h \ y^h - y_R^h\ _2 / \ y_R^h\ _2$	3.03×10^{-2}	1.23×10^{-3}	5.28×10^{-3}	0

Table 6.3: Optimal controls and runtime comparison of TC1 (-3°C) for varying number of state variables (DOF) including full and reduced order models. The reference control \tilde{u} results from the optimal control strategy described in section 6.4 using the reference discretization FOMR. The feed-in P is measured by FOMR based on the control suggested by each coarse model. The last row measures the relative error of outputs y comparing reference model FOMR, and each coarse model.

Optimal controls resulting from different spatial discretizations

Tab. 6.3 compares the runtimes and approximation qualities of both full and reduced order models. As quality indicators of the optimal control, the objective function, the relative l_2 error of the control and the maximal relative error of the feed-in constraint are considered. In addition, the maximum relative l_2 error of all outputs y is measured. Here, $y_R^h \in \mathcal{C}$ refers to output h determined by the reference discretization. Specifically, \tilde{u} is the optimal control determined by the fine model FOMR, and $\|P - \bar{P}\|_{\max}/\bar{P}$ results from the control suggested by a coarse model simulated using FOMR.

Focusing on TC1 and the suggested objective functions $\mathcal{J}(u)$, FOM1, FOMR, and ROM1 converge to a comparable value with FOMR taking the minimum of 52.6. FOM0 deviates clearly to 55.9. Regarding the relative deviation to the reference control, ROM1 shows the best approximation with 7.25×10^{-4} , followed by the full order models FOM1 and FOM0. The relative violation of the feed-in constraint is smallest for ROM1, followed by FOM1 and FOM0, while all models exhibit relative errors below one percent. Regarding the approximation quality of the outputs, FOM0 shows the expected strong diffusion, leading to a maximum relative error of 3.03×10^{-2} . Although this error does not affect the feasibility of the feed-in constraint, it leads to violations of the temperature constraints, measurable in practical applications. In contrast, ROM1 still approximates the outputs with an error of 5.28×10^{-3} .

Focusing on the runtimes for determination of the optimal control, ROM1 allows for a speed-up of 4.5 of the entire optimization compared to the coarsest and thus fastest possible unreduced model FOM0. In addition, the speed up compared to FOM1 amounts to 4.3, while achieving comparable results. The runtime of FOM0 results from a higher number of iterations necessary to fulfill the optimization tolerances. For the determination of the optimal control, resimulating the dynamics for a new control candidate takes the largest computational cost.

Different environmental temperatures

Hereafter, test cases TC2, TC3 are discussed, simulating higher mean daily temperatures. In these scenarios, both mean and maximum power consumption decrease compared to TC1. To achieve comparable power constraints for different test cases, a relative constraint $\bar{P} = G_0 + 0.5(\hat{G} - G_0)$ for the feed-in is chosen.

In contrast to TC1, the optimal control suggested for TC2 by ROM1 decreases the thermal control u_T^k compared to the initial control at 90°C , cf. fig. 6.4. The corresponding average volume flow increases. This happens at the expense of increasing pumping costs which can be neglected as described in section 6.3. Since the total power consumption for TC2 is smaller, the resulting increase in the volume flow does not exceed the level of TC1, allowing for identical pressure differences within the required constraints. In addition to a decreased mean value of the thermal control, also

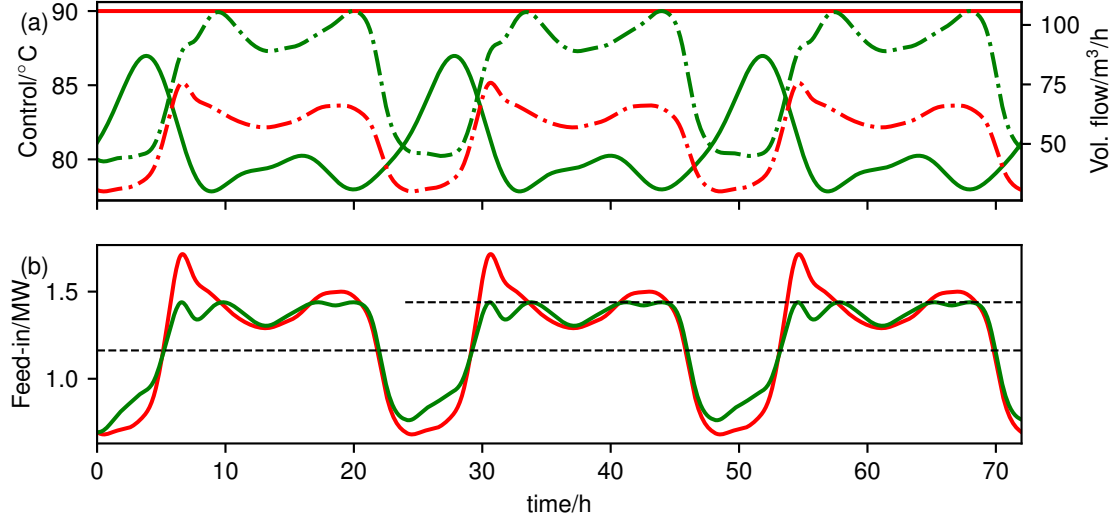


Figure 6.4: Optimal control problem for TC2 at 3 °C comparing the initial control (red) to the optimized control (green), obtained by the reduced model ROM1. For a detailed explanation we refer to fig. 6.2.

the temporal variation can be decreased. This leads to a smaller objective function of 14.6. Concerning error measures, the same observations discussed for TC1 apply, cf. tab. 6.4. The speed-up of ROM1 compared to FOM0(FOM1) results in a factor of 4.2 (5.4). For the last scenario TC3 simulating a mean daily temperature of 7.5 °C, the thermal control decreases in average value and temporal variation even further cf. fig. 6.5. The reduced consumption allows to increase the injected volume without violating pressure constraints. The injected flow temperature now approaches the lower limit defined at 75 °C. As observed for the other test cases, the approximation of the feed-in power is remarkably precise even for large deviations in the approximations of the outputs. For the coarsest discretization FOM0, the relative error of the feed-in constraint results in 1.46×10^{-2} , cf. tab. 6.5. To illustrate this observation for TC3, fig. 6.6(a) shows the output with the largest relative error compared to the reference discretization FOMR. The robustness of the feed-in constraint towards errors in the state-space approximation is unexpected by (6.17), in which the feed-in depends on the volume flows at household points defined by the thermal outputs y . Two explanations can be supplied for this effect. First, the feed-in depends on the sum of volume flows over all consumer points, allowing approximation errors to cancel. Furthermore, as the upwind discretization is a conservative finite volume scheme, the total stored energy is preserved on every discretization level.

In contrast to the large deviations observed for FOM0, ROM1 displayed in fig. 6.6(c,d) exhibits smaller errors in the output approximation. Specifically, it mainly deviates around the large gradient at $t = 54$ h resulting from changes in the flux direction occurring in the dynamical simulation visible for the reference discretization. Again, the error in the feed-in constraint resulting from an imprecise approximation of flux changes is small by two reasons. First, only few consumers are affected by changing

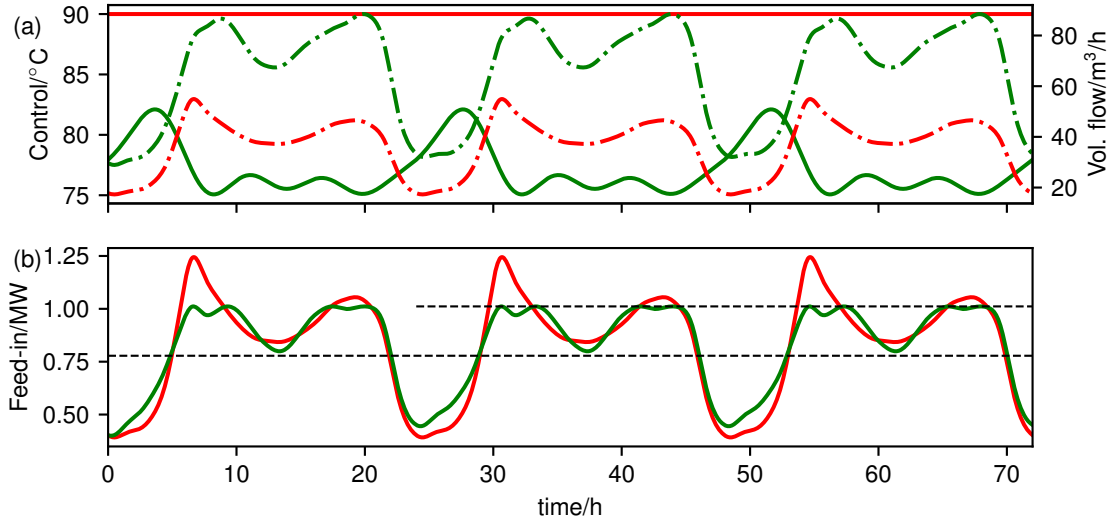


Figure 6.5: Optimal control problem for TC3 at 7.5 °C comparing the initial control (red) to the optimized control (green), obtained by the reduced model ROM1. For a detailed explanation we refer to fig. 6.2.

flux directions. Second, a change of flux directions is associated with the volume flow tending to zero, forcing the implied power to be zero as well. Hence, the absolute error in the power approximation remains small.

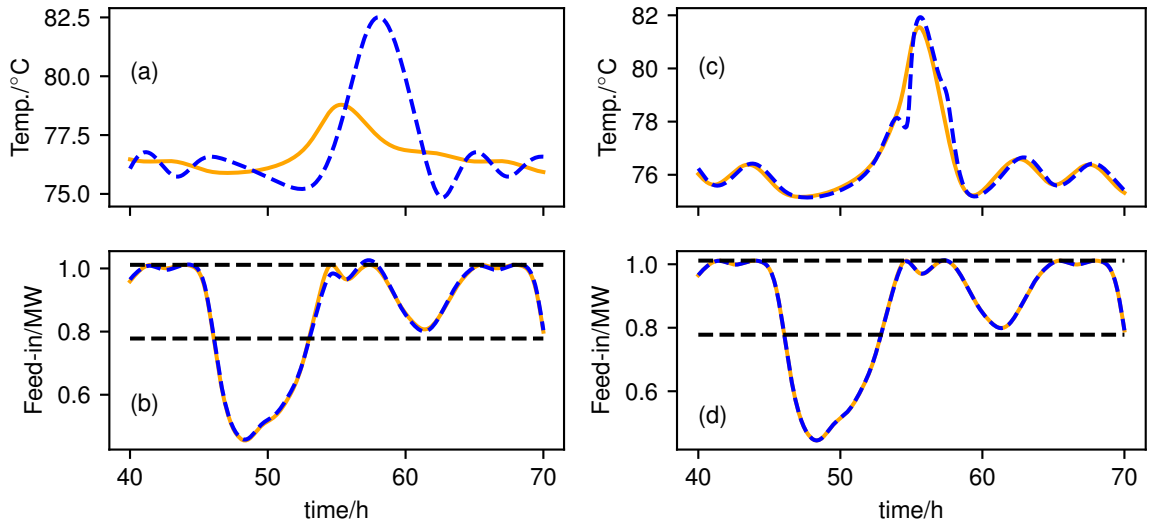


Figure 6.6: Temperature signal for TC3 at the consumer exhibiting the largest relative l_2 error (top) and feed-in power (bottom) comparing FOM0 (left) and the reduced model ROM1 (right). The output of both models (orange, solid) is compared to their validation using the reference discretization FOMR (blue, dashed line).

	FOM 0	FOM 1	ROM 1	FOMR
runtime opt./s	2525.0	3210.0	596.2	18300.0
runtime sim./s	2455.0	3146.7	546.2	18100.0
# solves DAE	15	11	11	13
DOF	775	1789	180	9538
$\mathcal{J}(u)$	16.5	14.8	14.8	14.6
$\ u - \tilde{u}\ _2 / \ \tilde{u}\ _2$	7.10×10^{-3}	6.17×10^{-4}	5.26×10^{-4}	0
$\ P - \bar{P}\ _{\max} / \bar{P}$	8.11×10^{-3}	6.86×10^{-4}	6.80×10^{-4}	0
$\max_h \ y^h - y_R^h\ _2 / \ y_R^h\ _2$	2.60×10^{-2}	1.25×10^{-3}	4.72×10^{-3}	0

Table 6.4: Optimization results and runtime comparison of TC 2(+3 °C) for different spatial discretizations including full and reduced order models. For a detailed explanation we refer the reader to table 6.3.

	FOM 0	FOM 1	ROM 1	FOMR
runtime opt./s	3165.0	5930.0	801.8	16400.0
runtime sim./s	3070.0	5795.0	735.2	16200.0
# solves DAE	19	21	15	13
DOF	775	1789	180	9538
$\mathcal{J}(u)$	6.7	5.6	5.6	5.5
$\ u - \tilde{u}\ _2 / \ \tilde{u}\ _2$	6.16×10^{-3}	6.14×10^{-4}	9.63×10^{-4}	0
$\ P - \bar{P}\ _{\max} / \bar{P}$	1.46×10^{-2}	1.34×10^{-3}	1.37×10^{-3}	0
$\max_h \ y^h - y_R^h\ _2 / \ y_R^h\ _2$	2.35×10^{-2}	1.57×10^{-3}	5.01×10^{-3}	0

Table 6.5: Optimization results and runtime comparison of TC 3(+7.5 °C) for different spatial discretizations including full and reduced order models. For a detailed explanation we refer the reader to table 6.3.

6.5.4 Components of the speed-up of the reduced order model

As discussed above, resimulating the dynamics is the central computational cost in determining an optimal control. One cause for the speed-up of the ROM is the few number of simulations of the forward problem to satisfy the tolerances for constraints and the objective function. The second cause is the speed-up resulting for a single solution of the DAE (6.10), which is discussed subsequently. For the implicit midpoint rule with n_t time steps, the computational cost c_{sim} splits into the following parts,

$$c_{sim} = n_t(n_{imp}(c_h + c_f) + c_J), \quad (6.25)$$

where n_{imp} is the number of iterations to solve for the upcoming time step, c_h is the cost of solving the algebraic equations (6.1e-6.1g) defining the flow field, and c_f is the cost of evaluating the differential part of the DAE. Finally, c_J denotes the cost to determine the Jacobian of the DAE with respect to energy densities. Since only the thermal transport is reduced, c_h is identical for both full and reduced order models. The cost for the evaluation of the ODE scales with the number of entries implied in the system operators $A(q), A_r(q)$ defined in (6.3). Using the upwind discretization,

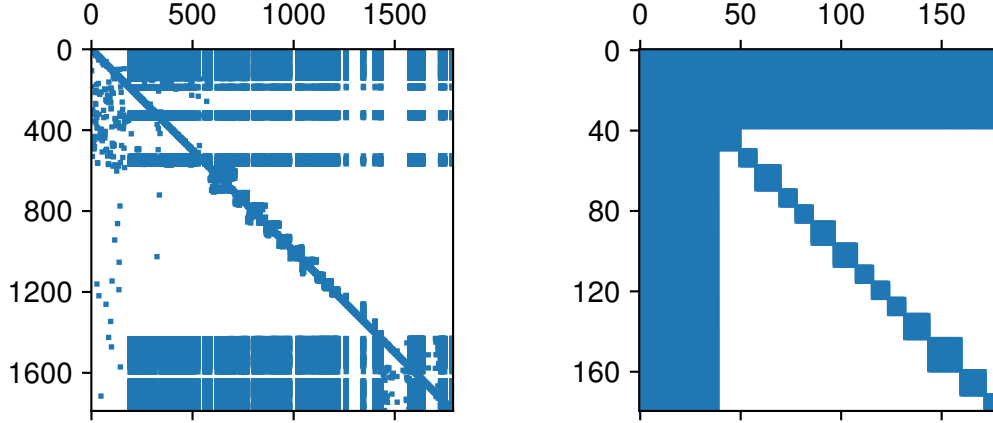


Figure 6.7: Illustration of the Jacobian matrix for the models FOM1 (left) and ROM1 (right) corresponding to the values shown in tab. 6.6.

$A(q) \in \mathbb{R}^{n \times n}$ is a sparse matrix. For typical networks, the number of nonzero entries can be limited by $3n$. In contrast, the system operator $A_r(q) \in \mathbb{R}^{r \times r}$ resulting from a Galerkin projection is dense with r^2 nonzero entries. As a consequence, the number of reduced states needs to be significantly smaller to reduce the computational cost. For the coarse discretization sufficient for the determination of an optimal control, this degree of reduction is barely possible. The key saving in applying the reduced order model stems from the computation of the Jacobian matrix. Based on the system operator description (6.3) and the structure of the equations defining the volume flow (6.1c - 6.1f), the Jacobian reads

$$J_{\dot{e}}(q, e) = \frac{\partial \dot{e}}{\partial e} = A(q) + \sum_{i=1}^{n_q} \frac{\partial \gamma_i}{\partial e} (A_i e + B_i u_T).$$

Since by the power balance at consumers (6.1e) and volume conservation (6.1c) each velocity depends on the energy densities at consumer stations, $J_{\dot{e}}(q, e)$ carries significantly more non-zero entries in the full order case than $A(q)$, cf. tab. 6.6, and fig. 6.7. In contrast, since the reduced order operator $A_r(q)$ is already densely populated by Galerkin projection, the number of non-zero entries does not increase significantly for the reduced Jacobian.

	FOM 0	FOM 1	ROM 1	FOMR
# nonzero entries $A(q)$	1555	3583	8519	19081
# nonzero entries $J_{\dot{e}}(q, e)$	67837	139922	14018	662200
DOF	775	1789	180	9538

Table 6.6: Maximal population density determined in the simulation of system operator and Jacobian for different discretizations. DOF denotes the number of differential state variables.

6.6 Conclusions

In this contribution, the optimal control of district heating networks using the reduced order model (ROM) suggested in chapter 4 was discussed. The suggested optimal controls resulting from minimizing the temporal variation of the control successfully limited the maximum feed-in power to the average of mean and maximum total consumption. In addition, practically relevant constraints on temperature and pressure were included reproducing realistic operation conditions. For the presented scenarios, this allowed to avoid the usage of additional, unfavorable sources of energy. While the ROM approximates both relevant state variables and gradient information sufficiently fine for the determination of an optimal control, it allowed for a speed up of the entire optimization phase by at least a factor 4, compared to even coarse levels of upwind discretizations used as full order models. For distinct test scenarios we observed even higher speed-ups of 7.3. Thus, the ROM gaps the bridge towards the determination of an optimal control within an online planning. The effectiveness of the ROM was demonstrated for an existing large scale network in which different pipelines change their flux direction dynamically. Runtime and approximation quality were studied for multiple real world scenarios including varying daily mean temperatures. This allows to apply the presented model to other networks and operation conditions relevant in practice.

Chapter 7

Conclusions and outlook

This work aimed at deriving a reduced order model for an efficient simulation and optimization of district heating networks. A suitable model for the description of the energy transport of heating networks was derived based on hyperbolic Euler-like equations in the incompressible limit. Using an upwind discretization of the internal energy density, a DAE which is quadratic in state resulted, including coupling conditions at pipeline junctions as algebraic constraints. The latter DAE describes an advection dominated, solenoidal transport of thermal energy along pipelines. The time- and state dependent boundary conditions formed by heat exchangers in combination with the momentum balance occurring in the Euler-like equations yield a nonlinear system of equations defining the velocity field. By neglecting the acceleration contribution in the momentum balance, the differentiation index of the DAE reduces from 2 to 1. This description allowed to derive a control system, for which Lyapunov stability of arbitrary topologies of district heating networks was proven under the assumption of volume conservation at network nodes. The existence of a unique solution is ensured for networks without cycles in the flow- and the return part of the topology. For networks in which no changes of flux directions occur, asymptotic stability to equilibrium states was shown. In proving Lyapunov stability, the corresponding Lyapunov function was explicitly constructed based on an energy matrix Q . This allows to embed the control system into a family of parameter varying port-Hamiltonian systems.

By splitting the DAE into a differential part describing the transport of energy density and an algebraic part defining the volume flow field, a linear time-varying system in the vector of energy densities results. The velocity field acts as a time-varying parameter to the advection equation on the network. This formulation enables to use concepts from parameterized model order reduction. To face the difficulties in the reduction of hyperbolic systems, a moment matching technique in frequency space was applied, approximating the input output relation defined by the transfer function. For linear models arising from fixed volume flow fields, a local Galerkin projection is determined. Subsequently, the Krylov subspaces of the local models are combined to a global Galerkin projection using a SVD. By incorporating the Kernel of the Lyapunov function Q , the reduction using the global Galerkin projection ensures a Lyapunov stable reduced order model. The linearizations entering the global projection are determined by a Greedy method. Using a frequency weighting in the determination

of the corresponding approximation error of the transfer function allows to further decrease the dimension of the reduced order model.

Decomposing the district heating network into subnetworks allows to define a block structure in the system operators which is preserved when applying a Galerkin projection. The suggested decomposition algorithm aims at equalizing the number of outputs in each subnetwork. Numerical investigations were conducted for two existing heating networks, including a large scale network exhibiting changes of flow directions. The investigations showed that the decomposition allows for a faster assembly of the system operators, and for a more efficient solution for a future time step when using implicit time integration schemes. A further decrease in computational time is accounted to the smaller dimension of the suggested reduced order model. The global Galerkin projection resulting from reduced order models of local linearizations is able to approximate the time-varying transport process with high accuracy. Using the approximation error of the global model to the local transfer functions proved to be a sufficient indicator for the approximation error in the time domain of the resulting simulations. An implicit Runge-Kutta scheme with an adaptive choice of the time step yielded the best results for the time integration of the DAE system resulting from upwind discretization.

The benefits of the suggested reduced order model were also validated in the determination of an optimal control. The optimization problem consisted of minimizing the absolute value and the temporal variation of the input energy density subject to a limit in the feed-in power as the central optimization constraint. The control problem was solved using the MATLAB[®] function `fmincon`. A key feature of the presented approach consisted of solving the DAE for the transport of energy density explicitly, and only passing the results including the objective function and technical constraints to `fmincon`. To facilitate the evaluation of sensitivities of relevant system outputs to the parameter vector, the implicit midpoint rule was used as a time integration scheme. Expressing the transport of energy in a system description allowed to analytically derive the Jacobian matrix in an efficient fashion. The suggested reduced order model proved to be significantly faster in the determination of an admissible control within three test scenarios. A main decrease in computational complexity arose from the formation of the Jacobian.

The results achieved in this thesis raise interesting further research topics. A central task is a model refinement towards three directions. First, incorporating thermal losses adds an additional nonlinear term to the transport of energy density. While this term is expected to further stabilize the system dynamics, embedding it into a port-Hamiltonian formulation is difficult. Specifically, even for a locally constant velocity field, the resulting dynamics of energy densities are nonlinear, and thus the reduction approach by moment matching in the transfer function can not be applied directly. A possible strategy is a linearization of the nonlinear thermal losses, to apply the suggested reduction approach. Second, adding the acceleration contribution to the momentum balance will effect the resulting solutions of the velocity fields for a given vector of energy densities. Moreover, an additional differential component is

introduced to the system which might qualitatively change the stability analysis of the DAE, as well as its port-Hamiltonian description. Still, the suggested algorithm to generate a reduced order model can be applied to the thermal transport. It will be interesting to study how the acceleration contribution alters the solutions of the velocity field, also in terms of flow changing pipelines in large scale networks. Third, adapting mass density and friction factor dynamically during the simulation will lead to a more accurate approximation of realistic transport dynamics. The achieved results concerning the stability of the resulting DAE and the benefits of the reduced order model are not expected to change, since solely the solution space of the velocity field is modified. An open task is a more efficient treatment of pipelines changing the direction of flow dynamically. These act as an additional nonlinearity by qualitatively changing the coupling structure of energy densities. To this end, it will be interesting to study different schemes for model order reduction as well as other discretization schemes for hyperbolic systems of equations.

Concerning the determination of optimal controls for the setup considered in chapter 6, a comparison to direct optimization approaches will be appealing, in which the transport dynamics of the network directly appear as optimization constraints, avoiding to resimulate the network dynamics in each iteration of the optimization routine. The number of additional optimization constraints resulting from the dynamics will be very high for a sufficiently fine discretization of the presented large scale network. A key observation will be the determination for which network topology which strategy performs best.

Bibliography

- [1] H. Lund et al. “4th Generation District Heating (4GDH)”. In: *Energy* **68** (2014), pp. 1–11.
- [2] B. Rezaie and M. A. Rosen. “District heating and cooling: Review of technology and potential enhancements”. In: *Applied Energy* **93** (2012), pp. 2–10.
- [3] B. Talebi et al. “A Review of District Heating Systems: Modeling and Optimization”. In: *Frontiers in Built Environment* **2** (2016), pp. 1–14.
- [4] S. Göttlich, M. Herty, and P. Schillen. “Electric transmission lines: Control and numerical discretization”. In: *Optimal Control: Applications and Methods* **37.5** (2016), pp. 980–995.
- [5] Y.-L. Jiang. “On Time-Domain Simulation of Lossless Transmission Lines with Nonlinear Terminations”. In: *SIAM Journal on Numerical Analysis* **42.3** (2004), pp. 1018–1031.
- [6] B. Geißler et al. “Mixed integer linear models for the optimization of dynamical transport networks”. In: *Mathematical Methods of Operations Research* **73.3** (2011), pp. 339–362.
- [7] V. Mehrmann, M. Schmidt, and J. J. Stolwijk. “Model and Discretization Error Adaptivity Within Stationary Gas Transport Optimization”. In: *Vietnam J. Math.* (2018).
- [8] M. Gugat et al. “MIP-based instantaneous control of mixed-integer PDE-constrained gas transport problems”. In: *Computational Optimization and Applications* **70.1** (2018), pp. 267–294.
- [9] M. Gugat et al. “Towards simulation based mixed-integer optimization with differential equations”. In: *NETWORKS* **72.1** (2018), pp. 60–83.
- [10] B. Geißler et al. “Solving power-constrained gas transportation problems using an MIP-based alternating direction method”. In: *Computers & Chemical Engineering* **82** (2015), pp. 303–317.
- [11] G. Sandou et al. “Predictive control of a complex district heating network”. In: *IEEE Conference on Decision and Control*. Vol. 44. 8. Citeseer. 2005, p. 7372.
- [12] R. Bavière and M. Vallée. “Optimal Temperature Control of Large Scale District Heating Networks”. In: *Energy Procedia* **149** (2018), pp. 69–78.
- [13] E. Guelpa et al. “Optimal operation of large district heating networks through fast fluid-dynamic simulation”. In: *Energy* **102** (2016), pp. 586–595.

- [14] T. Mertz et al. “A MINLP optimization of the configuration and the design of a district heating network: Academic study cases”. In: *Energy* **117** (2016), pp. 450–464.
- [15] A. Keçebaş and İ. Yabanova. “Thermal monitoring and optimization of geothermal district heating systems using artificial neural network: A case study”. In: *Energy and Buildings* **50** (2012), pp. 339–346.
- [16] H. Schlichting and K. Gersten. *Grenzschicht-Theorie*. 10th ed. Springer, 2006.
- [17] M. Herty, J. Mohring, and V. Sachers. “A new model for gas flow in pipe networks”. In: *Mathematical Models in the Applied Sciences* **30** (2010), pp. 845–855.
- [18] F. M. Hante et al. “Challenges in Optimal Control Problems for Gas and Fluid Flow in Networks of Pipes and Canals: From Modeling to Industrial Applications”. In: *Industrial Mathematics and Complex Systems*. Ed. by P. Manchanda, R. Lozi, and A. H. Siddiqi. Singapore: Springer Singapore, 2017, pp. 77–122.
- [19] D. Rim, S. Moe, and R. J. LeVeque. “Transport Reversal for Model Reduction of Hyperbolic Partial Differential Equations”. In: *SIAM/ASA Journal on Uncertainty Quantification* **6.1** (2018), pp. 118–150.
- [20] M. Wang et al. “Deep Learning-Based Model Reduction for Distributed Parameter Systems”. In: *IEEE Transactions on Systems, Man, and Cybernetics - Part A: Systems and Humans* **46.12** (2016), pp. 1664–1674.
- [21] M. Ohlberger and S. Rave. “Nonlinear reduced basis approximation of parameterized evolution equations via the method of freezing”. In: *Comptes Rendus Mathématique* **351.23** (2013), pp. 901–906.
- [22] A. C. Antoulas. *Approximation of Large-Scale Dynamical Systems*. Society for Industrial and Applied Mathematics, 2005.
- [23] M. K. Banda, M. Herty, and A. Klar. “Gas flow in pipeline networks”. In: *Networks & Heterogeneous Media* **1.1** (2006), pp. 41–56.
- [24] M. K. Banda, M. Herty, and A. Klar. “Coupling conditions for gas networks governed by the isothermal Euler equations”. In: *Networks & Heterogeneous Media* **1.2** (2006), pp. 295–314.
- [25] M. Gugat et al. “Well-posedness of networked hyperbolic systems of balance laws”. In: *Constrained optimization and optimal control for partial differential equations*. Springer, 2012, pp. 123–146.
- [26] H. Egger et al. “On Structure-Preserving Model Reduction for Damped Wave Propagation in Transport Networks”. In: *SIAM Journal on Scientific Computing* **40.1** (2018), A331–A365.
- [27] B. van der Heijde et al. “Dynamic equation-based thermo-hydraulic pipe model for district heating and cooling systems”. In: *Energy Conversion and Management* **151** (2017), pp. 158–169.
- [28] I. del Hoyo Arce et al. “Models for fast modelling of district heating and cooling networks”. In: *Renewable and Sustainable Energy Reviews* **82** (2018), pp. 1863–1873.

- [29] L. Giraud et al. “Optimal Control of District Heating Systems using Dynamic Simulation and Mixed Integer Linear Programming”. In: The 12th International Modelica Conference, Prague, Czech Republic, May 15-17, 2017. 2017, pp. 141–150.
- [30] National Institute of Standards and Technology. *Thermophysical Properties of Fluid Systems*. 2016.
- [31] J. P. Holman. *Heat transfer*. 10. ed. McGraw-Hill series in mechanical engineering. OCLC: 837082143. Boston, Mass.: McGraw-Hill Higher Education, 2010.
- [32] J. Welty, G. L. Rorrer, and D. G. Foster. “Fundamentals of momentum, heat, and mass transfer”. In: ed. by J. R. Welty. 5th ed. Hoboken, NJ: Wiley, 2008.
- [33] M. Schmidt, M. C. Steinbach, and B. M. Willert. “High detail stationary optimization models for gas networks”. In: *Optimization and Engineering* **16.1** (2015), pp. 131–164.
- [34] F. M. Hante and M. Schmidt. “Complementarity-based nonlinear programming techniques for optimal mixing in gas networks”. In: *EURO J Comput Optim* **7.3** (2019), pp. 299–323.
- [35] Technische Werke Ludwigshafen am Rhein AG. *Technische Anschlussbedingungen für die Versorgung mit Fernwärme aus den Versorgungsnetzen der Technischen Werke Ludwigshafen am Rhein AG*. 2019.
- [36] R. Köcher. “Beitrag zur Berechnung und Auslegung von Fernwärmenetzen”. Technische Universität Berlin, 2000.
- [37] J. A. Bondy, U. S. R. Murty, et al. *Graph theory with applications*. Vol. 290. Macmillan London, 1976.
- [38] R. J. LeVeque. *Numerical methods for conservation laws*. 2nd ed. Lectures in mathematics. OCLC: 552210683. Basel: Birkhäuser, 2008.
- [39] E. F. Toro. *Riemann solvers and numerical methods for fluid dynamics: a practical introduction*. 3. ed. OCLC: 391057413. Berlin: Springer, 2009.
- [40] B. Cockburn and C.-W. Shu. “The Runge-Kutta local projection P1-discontinuous-Galerkin finite element method for scalar conservation laws”. In: *ESAIM: Mathematical Modelling and Numerical Analysis* **25.3** (1991), pp. 337–361.
- [41] B. Cockburn, S.-Y. Lin, and C.-W. Shu. “TVB Runge-Kutta local projection discontinuous Galerkin finite element method for conservation laws III: One-dimensional systems”. In: *Journal of Computational Physics* **84.1** (1989), pp. 90–113.
- [42] B. Cockburn and C.-W. Shu. “Runge–Kutta Discontinuous Galerkin Methods for Convection-Dominated Problems”. In: *Journal of Scientific Computing* **16.3** (2001), pp. 173–261.
- [43] A. Ilchmann and T. Reis, eds. *Surveys in Differential-Algebraic Equations I*. Berlin, Heidelberg: Springer Berlin Heidelberg, 2013.

- [44] P. Benner, S. Gugercin, and K. Willcox. “A Survey of Projection-Based Model Reduction Methods for Parametric Dynamical Systems”. In: *SIAM Review* **57.4** (2015), pp. 483–531.
- [45] E. A. Coddington and N. Levinson. *Theory of ordinary differential equations*. Tata McGraw-Hill Education, 1955.
- [46] J. Pade. “Modeling and Numerical Analysis of Water Pipe Networks”. MA thesis. University of Cologne, 2013.
- [47] L. Jansen and J. Pade. *Global unique solvability for a quasi-stationary water network model*. Tech. rep. 2013.
- [48] V. Mehrmann. “Index concepts for differential-algebraic equations”. In: *Encyclopedia of Applied and Computational Mathematics* (2015), pp. 676–681.
- [49] K. Tsakalis and P. Ioannou. *Linear time-varying systems: control and adaptation*. Prentice Hall, 1993.
- [50] D. Hinrichsen and A. J. Pritchard. *Mathematical systems theory I: modelling, state space analysis, stability and robustness*. Vol. 48. Springer Science & Business Media, 2011.
- [51] R. A. Horn and C. R. Johnson. *Matrix analysis*. Second edition. New York, NY: Cambridge University Press, 2017.
- [52] P. Azimzadeh and P. Forsyth. “Weakly Chained Matrices, Policy Iteration, and Impulse Control”. In: *SIAM Journal on Numerical Analysis* **54.3** (2016), pp. 1341–1364.
- [53] C. Mehl, V. Mehrmann, and M. Wojtylak. “Linear Algebra Properties of Dissipative Hamiltonian Descriptor Systems”. In: *SIAM Journal on Matrix Analysis and Applications* **39.3** (2018), pp. 1489–1519.
- [54] A. van der Schaft and B. Maschke. “Generalized port-Hamiltonian DAE systems”. In: *Systems & Control Letters* **121** (2018), pp. 31–37.
- [55] A. J. van der Schaft and B. M. Maschke. “Port-Hamiltonian Systems on Graphs”. In: *SIAM Journal on Control and Optimization* **51.2** (2013), pp. 906–937.
- [56] A. Van Der Schaft. “Port-Hamiltonian systems: an introductory survey”. In: *Proceedings of the international congress of mathematicians*. Vol. 3. Citeseer. 2006, pp. 1339–1365.
- [57] R. V. Polyuga. *Model reduction of port-Hamiltonian systems*. PhD thesis, University of Groningen, 2010.
- [58] C. Beattie et al. “Linear port-Hamiltonian descriptor systems”. In: *Mathematics of Control, Signals, and Systems* **30.4** (2018), pp. 1–27.
- [59] S.-A. Hauschild et al. “Port-Hamiltonian modeling of district heating networks”. In: *arXiv:1908.11226 [math]* (2019).
- [60] A. Moses Badlyan et al. “Open physical systems: From GENERIC to port-Hamiltonian systems”. In: *Proceedings of the 23rd International Symposium on Mathematical Theory of Systems and Networks*. 2018, pp. 204–211.

- [61] A. Moses Badlyan and C. Zimmer. *Operator-GENERIC Formulation of Thermodynamics of Irreversible Processes*. arXiv:1807.09822. 2018.
- [62] P. Benner, M. Hinze, and E. J. W. ter Maten. *Model Reduction for Circuit Simulation*. Ed. by P. Benner, M. Hinze, and E. J. W. ter Maten. Vol. 74. Lecture Notes in Electrical Engineering. Dordrecht: Springer Netherlands, 2011.
- [63] P. Benner, ed. *System Reduction for Nanoscale IC Design*. 1st ed. Vol. 20. Mathematics in Industry. Springer, 2017.
- [64] S. Chaturantabut and D. C. Sorensen. “Nonlinear Model Reduction via Discrete Empirical Interpolation”. In: *SIAM Journal on Scientific Computing* **32.5** (2010), pp. 2737–2764.
- [65] N. Monshizadeh, H. L. Trentelman, and M. Kanat Camlibel. “Stability and synchronization preserving model reduction of multi-agent systems”. In: *Systems & Control Letters* **62.1** (2013), pp. 1–10.
- [66] N. Monshizadeh and A. van der Schaft. “Structure-preserving model reduction of physical network systems by clustering”. In: *Decision and Control (CDC), 2014 IEEE 53rd Annual Conference on*. IEEE, 2014, pp. 4434–4440.
- [67] R. V. Polyuga and A. van der Schaft. “Structure preserving model reduction of port-Hamiltonian systems by moment matching at infinity”. In: *Automatica* **46.4** (2010), pp. 665–672.
- [68] S. Gugercin et al. “Structure-preserving tangential interpolation for model reduction of port-Hamiltonian systems”. In: *Automatica* **48.9** (2012), pp. 1963–1974.
- [69] S. Gugercin et al. “Interpolation-based \mathcal{H}_2 model reduction for port-Hamiltonian systems”. In: IEEE, 2009, pp. 5362–5369.
- [70] C. Beattie and S. Gugercin. “Interpolatory projection methods for structure-preserving model reduction”. In: *Systems & Control Letters* **58.3** (2009), pp. 225–232.
- [71] S. Chaturantabut, C. Beattie, and S. Gugercin. “Structure-Preserving Model Reduction for Nonlinear Port-Hamiltonian Systems”. In: *SIAM Journal on Scientific Computing* **38.5** (2016), B837–B865.
- [72] G. Berkooz, P. Holmes, and J. L. Lumley. “The proper orthogonal decomposition in the analysis of turbulent flows”. In: *Annual review of fluid mechanics* **25.1** (1993), pp. 539–575.
- [73] K. Willcox and J. Peraire. “Balanced Model Reduction via the Proper Orthogonal Decomposition”. In: *AIAA Journal* **40.11** (2002), pp. 2323–2330.
- [74] A. Chatterjee. “An introduction to the proper orthogonal decomposition”. In: *Current Science* **78.7** (2000), pp. 808–817.
- [75] B. Haasdonk and M. Ohlberger. “Reduced basis method for finite volume approximations of parametrized linear evolution equations”. In: *ESAIM: Mathematical Modelling and Numerical Analysis* **42.2** (2008), pp. 277–302.

- [76] S. Hovland, J. T. Gravdahl, and K. E. Willcox. “Explicit Model Predictive Control for Large-Scale Systems via Model Reduction”. In: *Journal of Guidance, Control, and Dynamics* **31.4** (2008), pp. 918–926.
- [77] J. Reiss et al. “The Shifted Proper Orthogonal Decomposition: A Mode Decomposition for Multiple Transport Phenomena”. In: *SIAM Journal on Scientific Computing* **40.3** (2018), A1322–A1344.
- [78] P. Schulze, J. Reiss, and V. Mehrmann. “Model Reduction for a Pulsed Detonation Combuster via Shifted Proper Orthogonal Decomposition”. In: *Active Flow and Combustion Control 2018*. Springer, 2019, pp. 271–286.
- [79] R. Abgrall, D. Amsallem, and R. Crisovan. “Robust model reduction by L^1 - norm minimization and approximation via dictionaries: application to nonlinear hyperbolic problems”. In: *Advanced Modeling and Simulation in Engineering Sciences* **3.1** (2016).
- [80] S. Gugercin, T. Stykel, and S. Wyatt. “Model Reduction of Descriptor Systems by Interpolatory Projection Methods”. In: *SIAM Journal on Scientific Computing* **35.5** (2013), B1010–B1033.
- [81] S. Gugercin, A. C. Antoulas, and C. Beattie. “ \mathcal{H}_2 Model Reduction for Large-Scale Linear Dynamical Systems”. In: *SIAM Journal on Matrix Analysis and Applications* **30.2** (2008), pp. 609–638.
- [82] M. Gifftthaler et al. “Parametric Model Order Reduction of Port-Hamiltonian Systems by Matrix Interpolation”. In: *at - Automatisierungstechnik* **62.9** (2014), pp. 619–628.
- [83] U. Baur et al. “Interpolatory Projection Methods for Parameterized Model Reduction”. In: *SIAM Journal on Scientific Computing* **33.5** (2011), pp. 2489–2518.
- [84] U. Baur, P. Benner, and L. Feng. “Model Order Reduction for Linear and Nonlinear Systems: A System-Theoretic Perspective”. In: *Archives of Computational Methods in Engineering* **21.4** (2014), pp. 331–358.
- [85] P. Schulze et al. “Data-driven structured realization”. In: *Linear Algebra and its Applications* **537** (2018), pp. 250–286.
- [86] A. C. Ionita and A. C. Antoulas. “Data-Driven Parametrized Model Reduction in the Loewner Framework”. In: *SIAM Journal on Scientific Computing* **36.3** (2014), A984–A1007.
- [87] D. Hartman and L. K. Mestha. “A deep learning framework for model reduction of dynamical systems”. In: *2017 IEEE Conference on Control Technology and Applications (CCTA)*. 2017 IEEE Conference on Control Technology and Applications (CCTA). Mauna Lani Resort, HI, USA: IEEE, 2017, pp. 1917–1922.
- [88] J. Ling, A. Kurzwski, and J. Templeton. “Reynolds averaged turbulence modelling using deep neural networks with embedded invariance”. In: *Journal of Fluid Mechanics* **807** (2016), pp. 155–166.

- [89] J. N. Kutz et al. “On dynamic mode decomposition: Theory and applications”. In: *Journal of Computational Dynamics* **1.2** (2014), pp. 391–421.
- [90] J. L. Proctor, S. L. Brunton, and J. N. Kutz. “Dynamic Mode Decomposition with Control”. In: *SIAM Journal on Applied Dynamical Systems* **15.1** (2016), pp. 142–161.
- [91] M. I. Ahmad et al. “Moment-matching based model reduction for Navier-Stokes type quadratic-bilinear descriptor systems: Moment-matching based MOR for NS type QBDAEs”. In: *ZAMM - Journal of Applied Mathematics and Mechanics / Zeitschrift für Angewandte Mathematik und Mechanik* **97.10** (2017), pp. 1252–1267.
- [92] P. Benner, P. Goyal, and S. Gugercin. “ \mathcal{H}_2 -Quasi-Optimal Model Order Reduction for Quadratic-Bilinear Control Systems”. In: *SIAM Journal on Matrix Analysis and Applications* **39.2** (2018), pp. 983–1032.
- [93] C. Gu. “QLMOR: A Projection-Based Nonlinear Model Order Reduction Approach Using Quadratic-Linear Representation of Nonlinear Systems”. In: *IEEE Transactions on Computer-Aided Design of Integrated Circuits and Systems* **30.9** (2011), pp. 1307–1320.
- [94] P. Benner, T. Breiten, and T. Damm. “Generalised tangential interpolation for model reduction of discrete-time MIMO bilinear systems”. In: *International Journal of Control* **84.8** (2011), pp. 1398–1407.
- [95] M. Rewieński and J. White. “Model order reduction for nonlinear dynamical systems based on trajectory piecewise-linear approximations”. In: *Linear Algebra and its Applications* **415.2** (2006), pp. 426–454.
- [96] M. J. Rewienski. “A trajectory piecewise-linear approach to model order reduction of nonlinear dynamical systems”. PhD thesis. Massachusetts Institute of Technology, 2003.
- [97] T. Breiten, C. Beattie, and S. Gugercin. “Near-optimal Frequency-weighted Interpolatory Model Reduction”. In: *Systems & Control Letters* **78** (2015), pp. 8–18.
- [98] B. Anić et al. “Interpolatory weighted- model reduction”. In: *Automatica* **49.5** (2013), pp. 1275–1280.
- [99] C. Beattie and S. Gugercin. “Realization-independent \mathcal{H}_2 -approximation”. In: *51st IEEE Conference on Decision and Control*. IEEE, 2012, pp. 4953–4958.
- [100] R. Borsche, M. Eimer, and N. Siedow. “A local time stepping method for thermal energy transport in district heating networks”. In: *Applied Mathematics and Computation* **353** (2019), pp. 215–229.
- [101] X. Cheng, Y. Kawano, and J. M. A. Scherpen. “Reduction of Second-Order Network Systems With Structure Preservation”. In: *IEEE Transactions on Automatic Control* **62.10** (2017), pp. 5026–5038.
- [102] B. Besselink, H. Sandberg, and K. H. Johansson. “Clustering-Based Model Reduction of Networked Passive Systems”. In: *IEEE Transactions on Automatic Control* **61.10** (2016), pp. 2958–2973.

- [103] H.-J. Jongsma et al. “Model reduction of linear multi-agent systems by clustering with \mathcal{H}_2 and \mathcal{H}_∞ error bounds”. In: *Mathematics of Control, Signals, and Systems* **30.1** (2018), p. 6.
- [104] R. Borsche and J. Kall. “High order numerical methods for networks of hyperbolic conservation laws coupled with ODEs and lumped parameter models”. In: *Journal of Computational Physics* **327** (2016), pp. 678–699.
- [105] P. Benner, E. Sachs, and S. Volkwein. “Model order reduction for PDE constrained optimization”. In: *Trends in PDE constrained optimization*. Springer, 2014, pp. 303–326.
- [106] O. Lass and S. Ulbrich. “Model Order Reduction Techniques with a Posteriori Error Control for Nonlinear Robust Optimization Governed by Partial Differential Equations”. In: *SIAM Journal on Scientific Computing* **39.5** (2017), S112–S139.
- [107] R. M. Colombo et al. “Optimal Control in Networks of Pipes and Canals”. In: *SIAM Journal on Control and Optimization* **48.3** (2009), pp. 2032–2050.
- [108] S. Grundel et al. “Model Order Reduction of Differential Algebraic Equations Arising from the Simulation of Gas Transport Networks”. In: *Progress in Differential-Algebraic Equations*. Ed. by S. Schöps et al. Berlin, Heidelberg: Springer Berlin Heidelberg, 2014, pp. 183–205.
- [109] J. T. Borggaard and S. Gugercin. “Model reduction for DAEs with an application to flow control”. In: *Active Flow and Combustion Control 2014*. Springer, 2015, pp. 381–396.
- [110] M. Rein et al. “Model order reduction of hyperbolic systems at the example of district heating networks”. In: *arXiv:1903.03342 [math]* (2019).
- [111] Bundesverband der deutschen Gas- und Wasserwirtschaft (BGW). Bundesverband der deutschen Gas- und Wasserwirtschaft (BGW), 2006.

Curriculum vitae

Markus Rein

Personal information

Place of birth	Mannheim, Germany
Nationality	German

Education

10/2016 - present	Doctoral candidate Fraunhofer Institute for Industrial Mathematics ITWM Kaiserslautern
10/2016 - present	Doctoral candidate Technomathematics group Technische Universität Kaiserslautern
04/2016 - 10/2016	Qualification studies for a PhD in mathematics University of Kaiserslautern
12/2015 - 03/2016	Research assistant: Condensed matter theory Johannes Gutenberg-University Mainz
10/2013 - 12/2015	Master of Science Physics Johannes Gutenberg-University Mainz
04/2010 - 09/2013	Bachelor of Science Physics Johannes Gutenberg-University Mainz
03/2010	A-levels, Leininger-Gymnasium, Grünstadt

Lebenslauf

Markus Rein

Persönliche Daten

Geburtsort	Mannheim
Nationalität	deutsch

Akademischer Werdegang

Seit 10/2016	Doktorand Fraunhofer-Institut für Techno- und Wirtschaftsmathematik ITWM Kaiserslautern
Seit 10/2016	Doktorand Arbeitsgruppe Technomathematik Technische Universität Kaiserslautern
04/2016 - 10/2016	Promotionsqualifikationsstudium Mathematik Technische Universität Kaiserslautern
12/2015 - 03/2016	Wissenschaftlicher Mitarbeiter: Theorie kondensierter Materie Johannes Gutenberg-Universität Mainz
10/2013 - 12/2015	Master of Science Physik Johannes Gutenberg-Universität Mainz
04/2010 - 09/2013	Bachelor of Science Physik Johannes Gutenberg-Universität Mainz
03/2010	Abitur, Leininger-Gymnasium, Grünstadt

This thesis focuses on the formulation of reduced order models for a numerically efficient simulation of district heating networks. Their dynamics base upon incompressible Euler equations, forming a system of quasi-linear hyperbolic partial differential equations. The algebraic constraints introduced by the network structure cause dynamical changes of flow direction as a central difficulty. A control system is derived allowing to analyze essential properties of the reduced order model such as Lyapunov stability. By splitting the problem into a differential part describing the transport of thermal energy and an algebraic part defining the flow field, tools from parametric model order reduction can be applied. A strategy is suggested which produces a global Galerkin projection based on moment-matching of local transfer functions. The benefits of the resulting surrogate model are demonstrated at different, existing large-scale networks. In addition, the performance of the suggested model is studied in the numerical computation of an optimal control of the feed-in power employing a discretize-first strategy.

ISBN 978-3-8396-1581-2



FRAUNHOFER VERLAG